Achieving novel functionalities in semiconductor-crystalline oxide heterostructures through electrical and structural coupling

by

Kamyar Ahmadi-Majlan

Presented to the Faculty of the Graduate School of

The University of Texas at Arlington in Partial Fulfillment

for the Degree of

DOCTOR OF PHILOSOPHY

Supervisor

Dr. Joseph H. Ngai

Committee Members

Dr. Efstathios Meletis

Dr. Alex Weiss

Dr. Choong-Un Kim

Dr. Seong Jin Koh

THE UNIVERSITY OF TEXAS AT ARLINGTON

August 2018

Acknowledgements

I am sincerely thankful to my advisor, Dr. Joseph H. Ngai, for his continued support and contribution in the development of my research. His clear vision and expert guidance has helped me stay on track and made successful completion of my work possible. I would also like to express my gratitude to my thesis committee members Dr. Weiss, Dr. Meletis, Dr. Kim and Dr. Koh. I would like to thank my parents Giti and Esi, my wife Farinaz and my sister Kamelia for their constant encouragement and support without which this work would have not been possible. I would like to thank all my UT Arlington and Texas friends for friendship and emotional support. Since this documents consist of three separate projects with different collaborators, here I have shown acknowledgements section of each published articles to thank their scientific inputs in my thesis.

The band-gap engineering project (chapter 2)

This work was supported by the University of Texas at Arlington. The STEM characterization performed at the Center for Functional Nanomaterials at BNL was supported by U.S. Department of Energy, Office of Basic Energy Sciences, under contract no. DEAC02-98CH10886. The band offset measurements and the reciprocal space mapping were performed at PNNL and supported by the U.S. Department of Energy, Office of Science, Division of Materials Sciences and Engineering under Award 10122. The PNNL work was performed in the Environmental Molecular Sciences Laboratory, a national science user facility sponsored by the Department of Energy's Office of Biological and Environmental Research.

Superconductivity $YBa_2Cu_3O_{7-\delta}$ on silicon (chapter3)

This work was supported by the University of Texas Arlington, NSERC, and by the National Science Foundation (NSF) under award No. DMR-1508530.

Tuning metal insulator transition in $LaTiO_3/SrTiO_3$ on silicon (chapter4)

This work was supported by the National Science Foundation (NSF) under award No. DMR-1508530 and the University of Texas-Arlington under the Research Enhancement Program. We also thank the Alan G. MacDiarmid Nano Tech Institute at the University of Texas-Dallas for use of the Quantum Design PPMS. STEM work is supported by the Center for Functional Nanomaterials, BNL, which is supported by the U.S. Department of Energy (DOE), Office of Basic Energy Science, under Contract No. DE- SC0012704. We express our gratitude to S. Ismail-Beigi for providing the code for the Poisson-Schrödinger solver.

.

Department of Materials Science and Engineering

The University of Texas at Arlington

Abstract

Creating new materials that exhibit enhanced or novel behaviors is essential to meet the technological challenges we face today. Complex oxides are perfect candidates to overcome these challenges due to the range of electronic, optical, and ionic properties they exhibit. The research presented here, mainly focuses on overcoming two important challenges in oxide electronics. First, the ability of epitaxially growing multifunctional oxides on conventional semiconductor substrates and second, the successful integration of multifunctional oxide properties on semiconductors

Oxide molecular beam epitaxy was utilized to grow transition metal oxides with unprecedented control, layer-by-layer, at the atomic scale. Such control of growth enables oxides differing in chemical composition and functionality to be epitaxially combined in artificial heterostructures. By manipulating the composition and functionality, artificial heterostructures can potentially be designed to exhibit enhanced or new behaviors not found in bulk compounds. In this regard, the work presented here consists of three individual research projects in which each project has tried to integrate some of the functionalities of transition metal oxides into semiconductors for possible future device applications.

1. Project one: Band gap engineering at a crystalline oxide-semiconductor interface.
    - M.J. Moghadam et. al. Advanced Materials Interfaces, 2, 140049, (2015).

Project two: Superconducting $YBa_2Cu_3O_{7-\delta}$ grown epitaxially on $SrTiO_3$ buffered Si (001).

- K Ahmadi-Majlan et. al. Journal Bulletin of Materials Science, 41, 23, (2018).

Project three: Tuning the metal-insulator transition in $LaTiO_3/SrTiO_3$ heterostructures integrated on Si (001).

- Kamyar Ahmadi-Majlan et. al. Applied Physics Letters, 112, 193104, (2018).

Band-gap engineering at a semiconductors-crystalline oxide interface.

Complex oxide materials exhibit a wide range of properties such as magnetism, superconductivity, ferroelectricity and multiferroicity that are needed to create new functionalities and to address various challenges in energy harvesting and microelectronics. One way of creating new materials is to combine materials that exhibit dissimilar behaviors and try to electrically couple them. Oxides and semiconductors are two classes of materials with different properties. Combining them electrically may make it possible to create functionalities that cannot be realized in either material alone. In this regard, the main objective of the first part of this thesis is to achieve novel material functionalities by electrically coupling multifunctional oxides on to conventional semiconductors. Principles of band gap engineering were applied to change the band offset from Type-II to Type-I to create an electrical platform in which the conduction (valence) band of semiconductors is below (above) the conduction (valence) band of oxide. The system that we have explored is a solid solution of $SrZr_xTi_{1-x}O_3$ on a Ge substrate.

Various structural characterization techniques such as: X-ray diffraction measurements and scanning transmission electron microscopy confirm an atomically abrupt and structurally coherent interface between $SrZr_xTi_{1-x}O_3$ and Ge. Moreover, electrical characterizations like, current-voltage and capacitance-voltage measurements indicate that Type-I band offset has been achieved. Finally, X-ray photoemission spectroscopy was used to measure the band offset between the epitaxial oxides grown on Ge substrate.

Superconducting epitaxial $YBa_2Cu_3O_{7-\delta}$ on $SrTiO_3$ buffered Si (001)

The changes in technology along with the increased demand for effective electronic devices has prompted researchers to search for novel materials having new properties with the intention of creating faster and more reliable technologies. It has been indicated that the complex transition metal oxides exhibit exotic properties and are thus regarded as a likely choice for future electronic applications. Properties such as ferroelectricity, magnetism and superconductivity can be integrated into oxide-semiconductor heterostructures for device applications like microelectronic, sensing and energy harvesting technologies.

One of the most interesting and technologically relevant properties of complex transition metal oxides is superconductivity in which transition metal oxides exhibit zero resistance below a transition temperature. In the second part of the thesis, the effect of a single crystalline $SrTiO_3$ buffer layer on the transport properties of $YBa_2Cu_3O_{7-\delta}$ grown epitaxially on silicon was investigated. Single crystalline $SrTiO_3$ grown epitaxially on silicon using oxide molecular beam epitaxy is proven to be a reliable platform to integrate superconducting $YBa_2Cu_3O_{7-\delta}$ films. The stability of $SrTiO_3$ on silicon under ambient conditions without any protective layer makes it an ideal candidate to be used as platform for other deposition techniques like sputtering, which enables growth of $YBa_2Cu_3O_{7-\delta}$ on a larger size wafer. The single crystalline $YBa_2Cu_3O_{7-\delta}$ grown on $SrTiO_3$ buffered silicon exhibits higher T_c (93 K) as confirmed by transport measurement.

Tuning metal-insulator behavior in $LaTiO_3/SrTiO_3$ heterostructures integrated directly on Si (100) through control of atomic layer thickness.

Transition metal oxides that exhibit strongly correlated phenomena are of great interest due to their unique properties such as strong electron-electron correlation, high carrier density, superconductivity and magnetism which can be utilized in new electronic devices. The ability of

growing oxide heterostructures with atomic level precision utilizing oxide molecular beam epitaxy enables us to introduce strong electron-electron correlation phenomena at the interface through varying the thickness of oxide layers and manipulating the electronic stability of heterostructures. In the fourth chapter of this thesis, electrical and structural characterization of metal-insulator behavior in oxide heterostructures integrated directly on silicon were demonstrated.

The heterostructures that we have explored consist of a wide band gap insulating $SrTiO_3$ and Mott insulator $LaTiO_3$ epitaxially grown on un-doped Si (001). Scanning transmission electron microscopy images confirm atomically abrupt and coherent interface in the heterostructures in which reducing the thicknesses of the $SrTiO_3$ layer sandwiched between $LaTiO_3$ and silicon results in a metal insulator transition through enhancement of carrier-carrier scattering. The metallic side of the transition can be explained by Fermi-Liquid behavior and the insulating behavior can be described by activated transport. According to the data presented in this document, the metal-insulator transition observed in $LaTiO_3/SrTiO_3$ heterostructure is consistent with the transition through filling control mechanism.

Table of Contents

List of Figures

List of abbreviations

MBE	Molecular beam epitaxy
PLD	Pulse laser deposition
RHEED	Reflected high energy electron diffraction
RGA	Residual gas analyzer
QCM	Quartz crystal microbalance
STEM	Scanning transmission electron microcopy
HRTEM	High resolution transmission electron microscopy
HAADF	High angle annular dark field
XRD	X-ray diffraction
XPS	X-ray photoemission spectroscopy
RSM	Reciprocal/Real space mapping
AFM	Atomic force microcopy
EELS	Electron energy loss spectroscopy
PPMS	Physical property measurements system
TMO	Transition metal oxide
MIT	Metal -insulator transition
C-V	Capacitance-voltage
I-V	Current-voltage
CMOS	Complementary metal oxide semiconductor

Chapter1

Introduction

Multifunctional oxides on semiconductors

1.1 Introduction

Multi-functional oxides exhibit exotic properties such as ferroelectricity, superconductivity, metal-insulator transition, higher dielectric constant (*high-k materials*) and magnetism which can be utilized in electronic device applications [1,2], hence growing these oxides on conventional semiconductors are of great importance. To date, there have been extensive and active research on studying the properties of multifunctional oxides and the possibility of integrating their properties for electronic and microelectronic technologies.

Many of these oxides have already been synthesized and utilized at industrial levels. For instance, one of the interesting phenomena that observed in some multifunctional oxides is ferroelectricity in which electric polarization in these compounds can be reversed by changing the external electric field. $PbTiO_3$, $BaTiO_3$ and $PbZrTiO_3$ are among the known ferroelectric oxides with various applications in micromechanical systems and none volatile memory devices [1,2]. Thin film ferroelectric devices exhibit the lowest power consumption that make them ideal candidates for future dynamic random memory devices (DRAMs) or electrically erasable programmable read only memory flash drives (EEPROM) [1,2].

Superconductivity is another puzzling phenomenon that happens in some transition metal oxides like $YBa_2Cu_3O_7$ whereby a material loses all its resistivity below a certain critical temperature known as the transition temperature (T_c). This high temperature superconductivity can be utilized in many devices applications such as infrared sensors or superconducting quantum interface devices (SQUIDS) [3,4].

Another interesting property of multifunctional oxides like lanthanum titanate or vanadium oxide is the metal-insulator transition due to the strong correlation effect [5]. Their resistivity can be changed with the help of internal or external parameters like magnetic/electric field, pressure or strain. These types of oxides known as "Mott insulators" are ideal candidates for ultra-fast ON/OFF switch devices like MottFETs [6].

It is important to note that, changing chemical compositions and structural modulations even at the atomic levels have a profound effect on many properties of multifunctional oxides. For many practical applications, integrating these properties on technologically relevant platforms only possible through epitaxial growth of these oxides on semiconductor substrates. Therefore, one of the key factors in integrating some of the properties of oxides onto semiconductors for enhancements in device functionality is achieving a high-quality interface between multifunctional oxide layer and the substrate [7-13].

Advances in deposition techniques enabled us to achieve atomic-level control of heteroepitaxial growth of oxides on semiconductors, despite challenges involved in heteroepitaxial growth, such as the lattice or thermal mismatch, and the dissimilar nature of chemical bonding between semiconductors and oxides across the interface, [15-18]. The monolithic integration of

oxides on semiconductors with atomically sharp and coherent interface was made possible after the successful growth of epitaxial $SrTiO_3$ on Si (001) substrate by McKee et. al. [14].

The successful growth of epitaxial oxides on semiconductors and the ability of integrating their properties create an opportunity for many device applications such as logic technology, memory applications, energy harvesting [19-28]. Additionally, since many of these oxides are sensitive to temperature or pressure variations, strain gradient and magnetic field, they are very useful for sensor technologies [29-33].

1.2 Research Objectives and Motivations

The main goals of this work can be summarized in answering two fundamental questions:

1) Can multifunctional oxides be successfully grown on conventional semiconductors such as silicon or germanium?

2) Will these oxides retain their properties when epitaxially grown on semiconductors?

Here in this thesis, we have intentionally studied the integration of three different classes of multifunctional oxides that exhibit various properties such as high dielectric, superconductivity and strongly correlated phenomena on traditional semiconductor substrates in form of three individual projects:

1. Electrically coupling multifunctional oxide on conventional semiconductor platform using band gap engineering.
2. Utilizing oxide molecular beam epitaxy to integrate superconductivity of single crystalline $YBa_2Cu_3O_7$ on the most technologically relevant platform (silicon).
3. Structurally couple transition metal oxides that exhibit strongly correlated phenomena with the silicon substrate through controlling the atomic thickness.

Over the next four chapters, some of the advanced deposition and characterization methods such as molecular beam epitaxy, pulsed laser deposition, X-ray diffraction, X-ray photoemission spectroscopy, transmission electron microscopy, scanning transmission electron microscopy, atomic force microscopy, physical property measurement system, reflected high energy electron diffraction, X-ray synchrotron have been utilized to demonstrate the ability of epitaxially growing these three oxides on semiconductors while maintaining their properties.

1.3 Dissertation Overview

This document consists of five chapters. The following is an outline and summary of each chapter presented in this document:

Chapter 1, "Introduction": This chapter introduces the main motivations and challenges in growing multifunctional oxides on semiconductors in general, as well as providing a brief introduction to the basic physics of transition metal oxides and some specification of oxide molecular beam epitaxy system.

Chapter 2, "Electrically coupling multifunctional oxides on semiconductors": This chapter gives detailed information about principles of band gap engineering to tune the band offset between oxide and semiconductors as well as the ability of integrating electrical properties of multifunctional oxides (*SZTO*) on Ge substrate utilizing oxide molecular beam epitaxy system. Later in this chapter, various structural as well as electrical characterization techniques will be discussed in detail to better understand the process behind creating an electrical platform to integrate electrical properties of oxides on semiconductors.

Chapter 3, "Superconducting $YBa_2Cu_3O_7$ integrated on $SrTiO_3$ buffered silicon": In this chapter, the growth process and the ability of growing single crystalline $YBa_2Cu_3O_7$ on the silicon will be discussed. Previous studies have shown that growing $YBa_2Cu_3O_7$ on silicon was very challenging mainly because of inter-diffusion and formation of polycrystalline phase. Here MBE and pulsed laser deposition were used to grow single crystalline $SrTiO_3$ as a buffer layer to integrate superconductive $YBa_2Cu_3O_7$ on silicon. Later, transport measurements confirm that our approach resulted in achieving the highest reported transition temperature among $YBa_2Cu_3O_7$ films grown directly on silicon so far.

Chapter 4, "Tuning metal-insulator transition in strongly correlated oxide directly grown on silicon": Here, we have used several experimental and theoretical approaches to investigate the ability of tuning the metal-insulator transition through changing the thickness of heterostructures in which the metallic side of the transition can be explained by Fermi-liquid behavior and the insulating side can be perfectly fitted to the activation transport.

Chapter 5, "Conclusion and Outlook": Findings throughout the thesis regarding integrating multifunctional oxide properties on semiconductors are summarized in this chapter and some of the possible routes to continue studying these systems are proposed.

1.4 Literature Review

1.4.1 Integration of Multifunctional Oxides on Semiconductors

Semiconductors are a group of materials that are insulators in their nature but adding small amounts of impurities known as dopants make them electrically conductive. The dopant can be added into the semiconductor crystal unit-cell; the number of outer electrons determine the dopant type in which in case of Si or Ge, elements with 3-valence electrons are p-type dopants and 5-valence elements are n-dopants. In general, semiconductors can be classified into six main categories: elemental semiconductors such as Si or Ge, binary semiconductors like GaAs or GaN, oxides semiconductors such as $BaTiO_3$ and $SrTiO_3$, layered semiconductors, organic and magnetic semiconductors [34].

Silicon and germanium are the most studied semiconductors due to their role in electronic devices like transistors (only silicon) and sensors. Both belong to a group IV of the periodic table and have diamond crystal structure in which each atom forms covalent bonds with its four surrounding neighbors as shown in Figure 1.1.

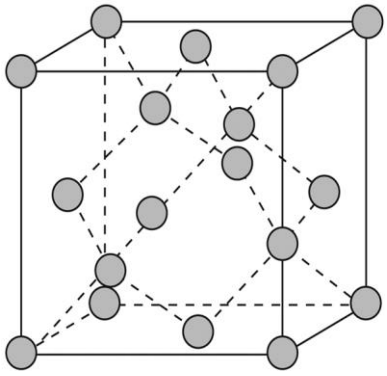

Figure 1.1: Diamond cubic crystal structure [S. Kittel. Introduction to solid state physics. Wiley 1968].

Aside from the abundance of silicon in nature, silicon has an energy band gap of 1.12eV at 0 K which makes it a stable element particularly in semiconductor technologies. In addition, doping ability of silicon (or germanium) [~ $2x10^{21}$ atom.cm^{-3}] due to its face center cubic crystal structure with 34% APF (atomic packing factor) makes it an ideal element for substitution of impurity atoms [34].

Even though many studies have been carried out on silicon or germanium as substrates, but as briefly mentioned above, interesting behavior that can be used for device applications usually occur in the thin films deposited on top of the substrate or at the interface. One of the most interesting compounds that can be grown as thin films on semiconducting substrates with interesting interface physics is transition metal oxides that will be discussed in detail over the following sections and chapters.

1.4.2 Transition Metal Oxides

Transition metal oxides, exhibiting variety of interesting electronic properties such as ferromagnetism, higher carrier densities, superconductivity, metal-insulator transition and many other exotic behaviors due to presence of strong electron-electron correlation [33]. However, understanding the physics behind the correlated phenomena still remains one of the greatest challenges of solid state physics and oxide electronics.

1.4.3 Perovskites

Perovskite oxides are among the most important classes of transition metal oxides due to their unique properties and crystal structures [35]. The perovskites have ABO_3 chemical composition and cubic crystal structure where corner atoms are the A-sites and transition metals are in the center of the cube surrounded by oxygen atoms as shown in Figure 1.2 (a). According to the Goldschmidt calculations, perovskite can almost accommodate all the element of the periodic table due to its high tolerance factor (t) [36]. In an ideal case where the tolerance factor is one (t =1) the perovskite has the cubic structure whereas by increasing the size of the A-site cations or generally decreasing the tolerance factor, the perovskite will be distorted which result in a formation of orthorhombic crystal structure. Other crystal structures of perovskite are also existed in nature depending on the size of the ions forming the crystal like $BaTiO_3$ that has tetragonal perovskite structures [37].

Prior to study the properties of these oxides, it is important to briefly discuss some of the fundamental physics behind the transition metal oxides (*d-orbital systems*). There are four key parameters involve in determining the electrical properties of transition metal oxides in general and perovskites in particular. 1)Band width and orbital hybridizations, 2) Crystal field splitting, 3) Hund's coupling and 4) electron-electron interactions which will be discussed in the following sections.

1.4.4 Orbital Hybridizations and Bandwidth in Perovskites

Crystal distortion has a profound effect on orbital overlapping and electronic behaviors of perovskites. As shown in Figure 1.2(a) in a cubic perovskite crystal structure, oxygen atoms (occupying *p-orbitals*) are located in an octahedral cage surrounding the transition metal (occupying *d-orbitals*) situated in a center of the cube [38]. Hence, hopping electrons from one metal site to the neighboring one will be resulted in a *p-d orbital* over lapping. This *p-d orbital* overlap is called "hybridizations" which is the origin of many interesting phenomena that seen in transition metal oxides [13]. Generally, the size and shape of the *d-orbitals* are smaller than s and p ones which give raise to relativity narrower bandwidth. In principle, the size of the bandwidth can be determined from the overlap of two adjacent neighboring transition metals in the crystal [39]. In an ideal perovskite with tolerance factor equal to one like $SrTiO_3$, the oxygen-titanium-oxygen bonds are in a straight line with maximum orbital overlapping whereas in a distorted perovskite the bond angles between the oxygen and transition metals are smaller which reduce the *p-d orbital* overlapping and alter the electronic properties as shown in Figure 1.2 (b).

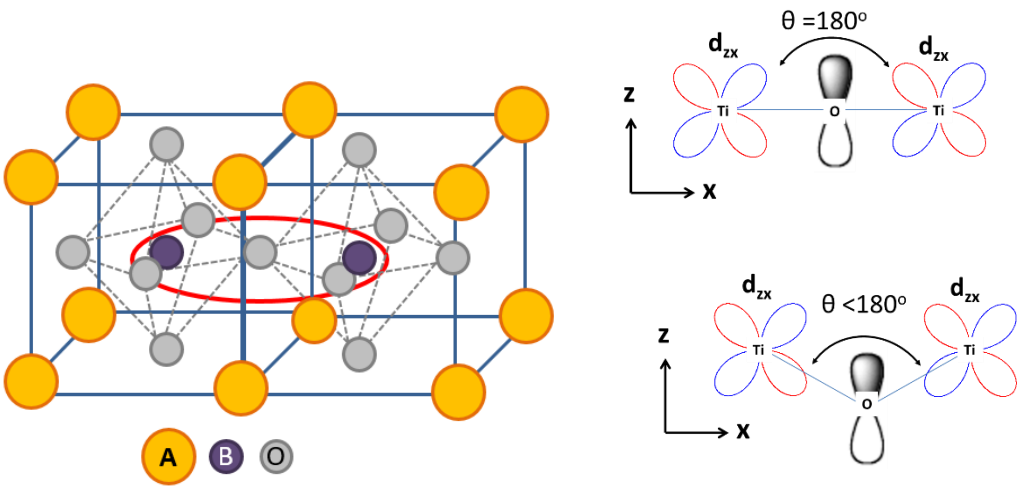

Figure 1.2: (a)Two perovskite crystals showing O-Ti-O bonds (b) Ideal perovskite p-d orbitals, (c) distorted p-d orbitals.

1.4.5 Crystal field splitting in perovskites

Another important parameter in determining the electronic behavior of transition metal oxides is the crystal splitting due to strong electron correlation. In order to understand some of the very important properties of transition metal oxides, one must consider the effect of neighboring atoms (negative point charge) on the behavior of *d-orbital* of transition metals. One of the most successful theories that explain the effect of negative charge (ligands) on the energy of *d-orbital* electrons of a transition metal ion is the crystal field theory [40]. According to crystal field theory, *d-orbitals* in transition metal oxides split into higher energy orbitals known as e_g and lower energy ones called t_{2g}. Following the symmetry rules in *d-orbitals*, e_g orbitals consist of d_z^2 and $d_{x^2-y^2}$ where as t_{2g} orbitals consist of d_{xy} , d_{yz} and d_{xz} orbitals as shown in Figure 1.3(a).

For the transition metals in the absence of any crystal fields, all the *d-orbitals* are degenerated which means they all have the same energy levels. However, in the presence of any other atoms such as oxygen in a cubic perovskite, some of the orbital lobes pointing directly toward the oxygen orbitals which resulted in a higher energy state (d_z^2 and $d_{x^2-y^2}$) due to the stronger Coulomb repulsion force, whereas other orbitals pointing in different directions having lower energy state (t_{2g}) [41]. The energy difference between the higher energy e_g orbitals and the lower t_{2g} is called the crystal field splitting (Δ). The crystal field splitting energy depends on the position as well as symmetry of surrounding negative charges [42].

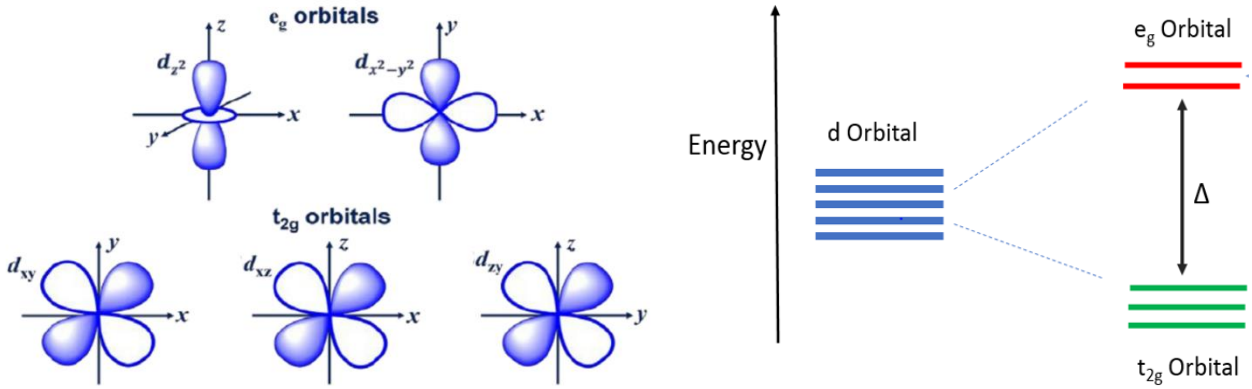

Figure 1.3: (Left)The d-orbital with different orientation of e_g and t_{2g} sets. (Right) Crystal field splitting [Adapted from A. Biswas et al. cond-mat arXiv:1508.04929 2015].

1.4.6 Hund's Coupling in perovskites

In addition to the crystal filed splitting, according to the Hund's coupling rule the most favorable electronic configurations happen when electrons are further apart (minimizing the energy of the occupying states). In other words, electrons filling the energy states based on the orbital energy levels, meaning the lowest energy orbitals fill first and then remaining electrons filling higher energy orbitals.

Hund's rule states that: in order to maximize the total spins of electrons, every orbital in a sublevel is first singly occupied having the same spin. Generally, Atoms at ground states prefer to have as many unpaired electrons as possible because electrons want to reduce repulsion force by filling their own orbitals, instead of sharing an orbital with another electron, therefore, electrons tend to occupy degenerate orbitals first, prior to start pairing half-filled orbitals. with the same energy [40].

1.4.7 Strong electron correlation in perovskites

Strong correlation is another important parameter that determines the electrical properties of perovskites. Prior to explain the strong correlation effect in oxides, it is important to briefly mention the history of theoretical attempts to explain electrical behavior of many transition metal oxides. The first successful approach to explain metallicity and insulating behavior in materials was based on non-interacting electrons known as band theory of solids, in which insulators are classified as materials with completely filled energy bands whereas metals are the ones with partially filled orbitals. Insulators with smaller energy gaps in which electrons can easily excite between conduction band and valence band were recognized as semiconductors as shown in Figure 1.4 [43].

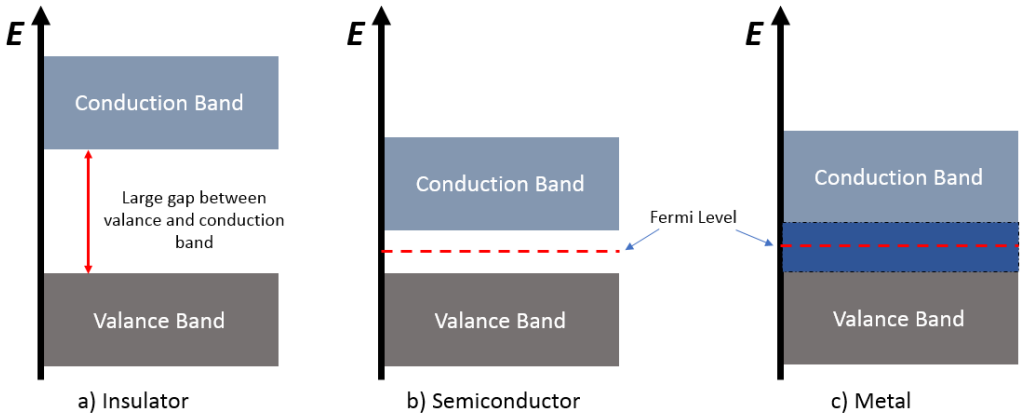

Figure 1.4 : The band theory of solids.

However, despite its success in explaining many properties of solids, the band theory was unable to explain insulating (or metallic) behavior of many partially filled *d-orbital* systems. A perfect example was NiO with partially filled orbitals [43]. According to the band theory, NiO must show metallic behavior (partially filled electrons in conduction band) but instead exhibiting insulating behaviors.

In order to unravel the strange behavior observed in transition metal oxides, Peierls and Mott pointed out the importance of electron-electron interactions in transport properties of solids which could explain insulating behavior seen in NiO. They have suggested: "it is quite possible that the electrostatic interaction between the electrons prevents them from moving at all. At low temperatures the majority of the electrons are in their proper places in the ions. The minority which have happened to cross the potential barrier find therefore all the other atoms occupied, and in order to get through the lattice have to spend a long time in ions already occupied by other electrons. This needs a considerable addition of energy and so is extremely improbable at low temperatures" [44]. Over the last decade scientist tried to understand how an insulator can become a metal and more importantly under what conditions metal to insulator transition occur in solids (partially filled *d-orbitals*).

According to the Pauli exclusion principle, two electrons with the same quantum numbers cannot occupy the same energy state, but electrons with different quantum number (opposite spins) can still occupy the same energy state [43-45]. A few years later, Mott argued that: two electrons occupying the same energy state would experience Coulomb repulsion force. According to the laws of thermodynamics, system would minimize the repulsion force by splitting the bands into lower occupied state and higher empty state. Therefore, the lower band would be full and the system exhibiting insulating behavior. This type of insulators that the insulating behaviors arise from the band splitting due to Coulomb repulsion is known as Mott insulators [45].

Strong Coulomb repulsions in transition metal oxides result in the emergence of phenomena such as metal-insulator transitions, high-temperature superconductivity, colossal magnetoresistance etc. [13].

This thesis, mainly focused on three different transition metal oxides with different electronic configurations; band insulator $SrTiO_3$ with d^0 electron configuration, Mott insulator $LaTiO_3$ with d^1 electron configuration and superconducting $YBa_2Cu_3O_7$ with d^9 configuration.

1.4.8 Band Insulator $SrTiO_3$

One of the most famous perovskites is $SrTiO_3$ with a lattice constant of a = 3.905 Å. In the cubic ABO_3 crystal structure, Sr^{2+} ions occupying the corner of the cube while transition metal Ti^{4+} is located in the center of the cube surrounded by oxygen cage in a middle of the cube as shown in Figure 1.5[46,47].

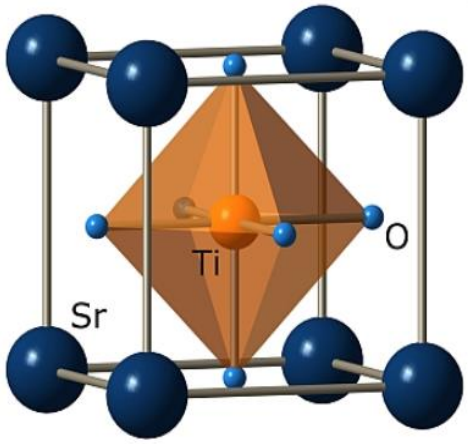

Figure 1.5: Crystal structure of perovskite $SrTiO_3$.

Many d^0 insulators are very sensitive to oxygen vacancies which can give rise to semiconducting behavior. According the band theory, the valence band of $SrTiO_3$ completely filled and *d-orbital* is completely empty which give rise to insulating behavior as shown in Figure 1.6(a) [46,47].

Many of the interesting properties of $SrTiO_3$ can be attributed to the nature of ionic-covalent bonding in its crystal structure in which Ti^{+4} ion in a center of the cubic perovskite forms an equal titanium to oxygen bond. The $SrTiO_3$ in stoichiometric form (Sr/Ti is 1:1) is an insulator with a wide band gap of 3.2 eV (at 0K) [48]. The electrical conductivity of $SrTiO_3$ can be modified with the presence of oxygen vacancies dopants or extrinsic defects. Variation in the amount of Sr and oxygen atoms in the crystal have proven to be more effective in changing the $SrTiO_3$ conductivity than the Ti vacancies. [49].

Recently, many studies have been performed on $SrTiO_3$ due to its properties such as high charge capacity, high dielectric constant, optical transparency, excellent insulator and more importantly its ability to be epitaxially grown on many substrates. Moreover, many studies have also been carried out on the interface between $SrTiO_3$ and $RTiO_3$ oxides due to the formation of 2-dimensional electron gas. The $SrTiO_3$ has many applications in device technologies such as phase shifters, filters, tunable oscillators, wave guides etc. $SrTiO_3$ can be epitaxially grown using various deposition techniques such as pulsed laser deposition and molecular beam epitaxy [50-54].

The ability of tuning the conductivity of $SrTiO_3$ as well as having a high-dielectric constant makes $SrTiO_3$as a possible gate dielectric for future transistors such as MOSFETs and varistors [55,56]. Some of the physical properties of $SrTiO_3$ is shown in Figure 1.6 (b).

(a)

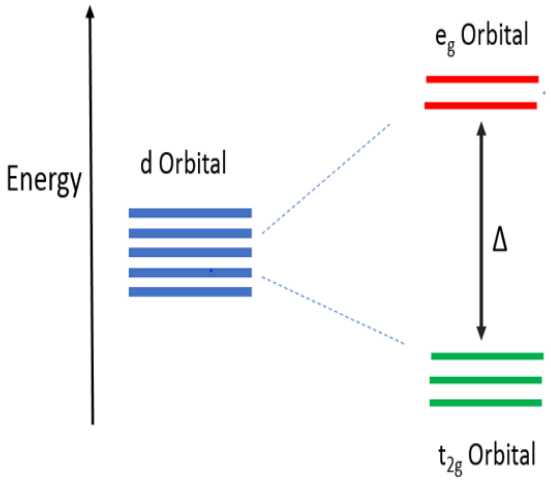

(b)

Property	Value
Lattice parameter at RT (nm)	0.3905
Atomic density (g/cm^3)	5.12
Melting point (°C)	2080
Mohs hardness	6
Dielectric constant (ε_0)	300
Thermal conductivity (W/m.K)	12
Coefficient of thermal expansion (Å/°C)	9.4×10^{-6}
Refractive index	2.31-2.38

Figure 1.6: (a)Insulating behavior of $SrTiO_3$ due to empty d-orbital. (b) Physical properties of STO.

1.4.9 Mott Insulator $LaTiO_3$

Another example of a transition metal oxide that exhibits strong Coulomb interactions is $LaTiO_3$. The $LaTiO_3$is a known Mott insulator with d^1 electron configuration. According to the band theory, $LaTiO_3$ is a metal with one unpaired electron in the *d-orbital*. However, due to strong electron correlation, a gap opens up between fully occupied oxygen *p-orbitals* and singly occupied *d-orbitals* as shown in Figure 1.7. This energy splitting between the upper and lower bands is the origin of insulating behavior observed the $LaTiO_3$ [58]. There are three main parameters controlling the charge gap and metal-insulator behavior in Mott driven materials like $LaTiO_3$: "U", the hopping energy of electron moving from one site to another site, "μ", the chemical potential or electron concentration and "t", the band width.

$LaTiO_3$ crystallize in a form of distorted cubic perovskite with chemical formula of ABO_3 like $SrTiO_3$. The La^{+3} ions occupy the corner of the cube whereas transition metals Ti^{+3} are located in a center surrounded by oxygen atoms. The $LaTiO_3$ is polarized in which $La^{+3}O^{-2}$ planes have +1. Recently, $LaTiO_3$has attracted increasing attentions due to its unique properties such as metal-insulator transition that can be attributed mainly to the strong electron-electron interaction [59].

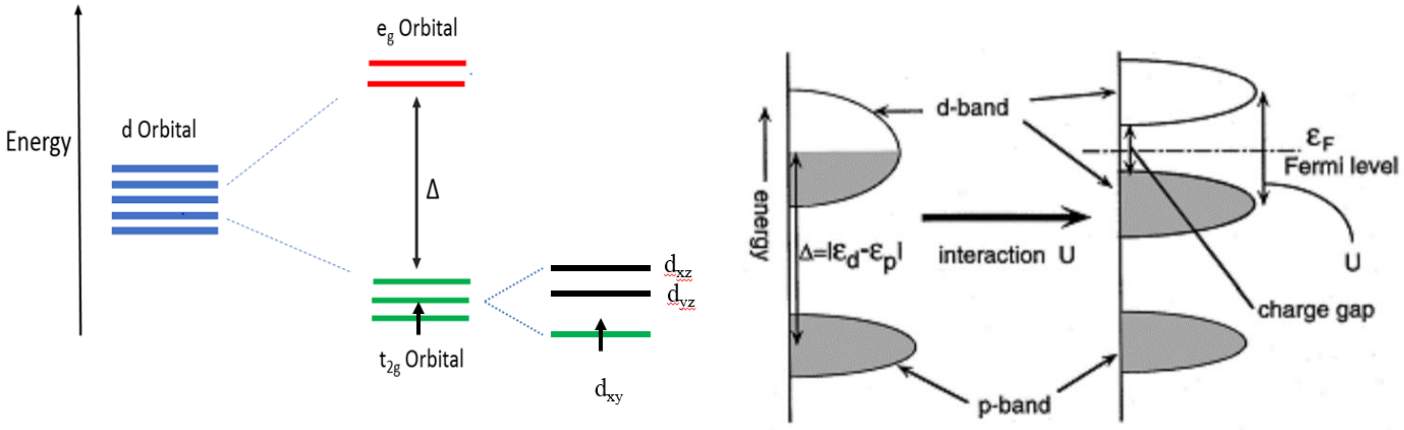

Figure 1.7: Crystal field splitting for d-orbitals and unchanged p orbitals [Adopted from Q. Meng "Metal Insulator Transition" (2010)].

1.4.10 Superconducting $YBa_2Cu_3O_7$

The cuprate superconductor compounds consist of multi-layers of CuO_2, alkaline oxide (AO) and transition metal oxides (MO_2) that stack in different sequences. $YBa_2Cu_3O_7$ is among the cuprate superconductors having perovskite crystal structure with a stacking sequence of $CuO–BaO–CuO_2–Y–CuO_2–BaO$ along the c-axis as shown in Figure 1.8. Oxygen content plays an important role in superconducting behavior of $YBa_2Cu_3O_7$. Oxygen chains in $YBa_2Cu_3O_7$ crystal structure can act as charge reservoirs in which electrons are transferred to the copper-oxygen

planes, hence, varying the amount of oxygen in the unit-cell can have a profound effect on physical properties, crystal structure (distortion) and even critical temperature [60].

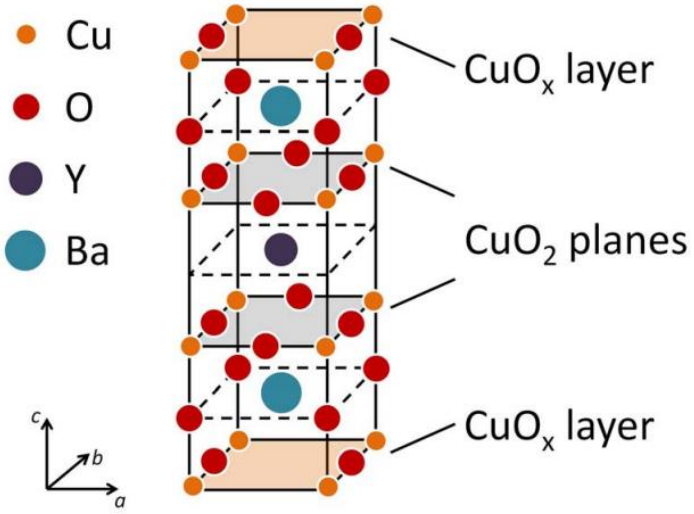

Figure 1.8: Crystal Structure of Superconducting $YBa_2Cu_3O_{7-\delta}$ [B. Howe. Crystal structure of YBCO. Minnesota State University]

Following the discussion above, cuprate superconductors with CuO_2 planes like the $YBa_2Cu_3O_7$ system are a perfect example of *d-orbital* splitting due to strong electron correlation. The Cu^{2+} atoms have a d^9 electron configuration which classifies $YBa_2Cu_3O_7$ as a heavy transition-metal oxide with a strong hybridization between the *d*-orbitals and the oxygen *p*-orbitals [60]. In the cuprate systems, the unpaired electrons in Cu ions occupy the $d_{x^2-y^2}$ state near the filled oxygen *2p-orbitals*.

According to the band theory of solids, this electron configuration would give rise to a metallic behavior while strong electron-electron Coulomb repulsion causes a band splitting in order to lower the total energy state. This band splitting, due to strong electron interactions, result in an emergence of insulating behavior where energy bands are separated into higher and lower energy sub-bands known as upper Hubbard band (UHB) and lower Hubbard band (LHB) [61]. In the $YBa_2Cu_3O_7$ system, the e_g *orbitals* are strongly hybridized with the *p-orbitals* which means the *p-orbitals* located between the upper and lower Hubbard bands as illustrated in Figure 1.9 [62]. Many studies have performed over the years on the origin of superconductivity in cuprate system which is beyond the context of this thesis. All of the transition metal oxides that have been studied in this document are classified under perovskite crystal structure. Therefore, a brief introduction about perovskite is important for further discussions in the following chapters.

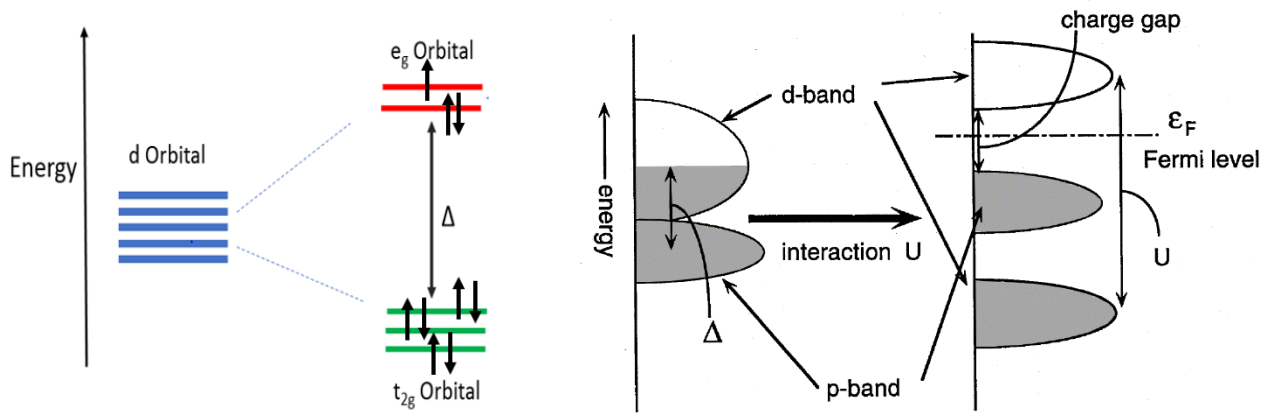

Figure 1.9: The band splitting in CuO_2 planes due to strong electron [Imada, et al. Rev. Mod. Phys., (1998)]

1.4.11 Challenges in Oxide-Semiconductor Heteroepitaxy

One of the main challenges of integrating multi-functional oxides on to semiconductors is the crystal structure difference between perovskite (ABO_3) like $SrTiO_3$ and diamond cubic semiconductors like silicon or germanium. The lattice constant of Si along [110] direction is slightly smaller than the lattice constant of perovskite $SrTiO_3$ which results in less than 2% compressive strain at the interface [66]. In order to accommodate the lattice mismatch between diamond cubic Si and perovskite $SrTiO_3$, the surface unit cell of silicon is rotated 45° as shown in Figure 1.10. This type of rotation is common in epitaxial growth of perovskites on diamond structure semiconductors [14,66].

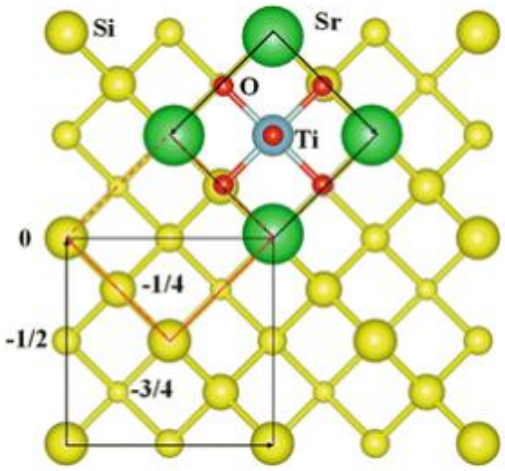

Figure 1.10: Epitaxial matching of $SrTiO_3$ and Si (001). [A. Demkov, Integration of multifunctional oxides with semiconductors, springer 2014]

One of the other difficulties of successfully growing epitaxial films on semiconductors is the wetting parameter. According to thermodynamics, the sum of surface energies of the growing films (new surface) and the cost of creating new interface must be lower than the surface energy of the substrate [67].

Depending on the chemical bonding between the new surface and the underlying layers, epitaxial growth of a thin film on the substrate can create one of two types of new interfaces: homo-epitaxy and hetero-epitaxy [68]. In homo-epitaxy, both the substrate and the film share the same crystal structure as well as the same chemical bonding, like growing semiconductor on semiconductor, therefore the interface energy is small and the lattice mismatch is minimal, consequently achieving the desirable wetting surface is relatively easy [69].

However, in hetero-epitaxy, the substrate and the film are from different crystal structures and chemical bonding, like growing perovskite (ABO_3) on top of a diamond cubic silicon [70-72]. Perovskites have ionic chemical bonding while silicon has covalent bonding which results in a higher surface energy costs. In order to reduce the raised surface energy, templates must be created at the perovskite/semiconductor interface to act as a wetting layer for subsequent layers. Many technological applications in device technologies such as superconductivity, ferromagnetism, ferroelectricity, energy harvesting, transistor technologies, etc. are the result of the hetero-epitaxial growth. In general, there are three modes of epitaxial growth [73]:

1. Layer by layer growth or Frank-Vander Merwe growth.
2. 3-D nucleation or Volmer-Weber growth.
3. Mixed mode or Stranski-Krastanov growth.

In Volmer-Weber mode, an initial monolayer form on a surface template and subsequent layers grow on top. When a thickness reaches a certain number of layers known as “critical thickness”, the lattice mismatch energy raises to the point that dislocations begin to form in order to lower the surface energy [74]. A perfect example of 2-dimensional growth is epitaxial growth of $SrTiO_3$ on silicon [14]. In three-dimensional mode, as the name suggests, the initial nucleation forms on surface features such as atomic steps, impurities or crystal defects.

Surface nucleation on these active sites known as "islands" reduces the surface energy. In cases where the lattice mismatch is more than 2% the crystal growth mode tends to follow the Stranski-Krastanov mode in which the surface energy is lower than the strain energy. The mixed mode growth is very common in growing superconducting $YBa_2Cu_3O_7$ films [74-76]. All different modes of growth are shown in Figure 1.11.

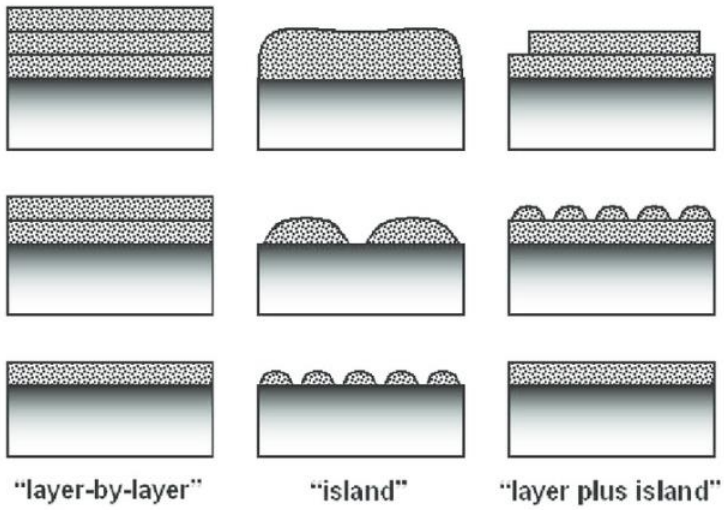

Figure 1.11: Three main growth modes [M. Ohring, The Materials Science of thin Films, Academic Press (1992)].

In 1998, R. A. McKee, F. J. Walker, and M. F. Chisholm were able to successfully grow heteroepitaxial $SrTiO_3$ on a silicon (001) substrate by molecular beam epitaxy chamber for the first time. In their approach, ½ monolayer of Sr metal was deposited on a clean silicon surface to form a 2x1 (reconstruction) template for subsequent layers. In fact, half a monolayer of Sr occupying positions among silicon dimer rows prevents the formation of a silicon oxide layer during the $SrTiO_3$ growth. It is important to note that although $SrTiO_3$ can be epitaxially grown on Si with different deposition techniques and process, but all rely on the initial ½ monolayer Sr template layer that is essential for depositing subsequent SrO and TiO_2 layers [13].

1.4.12 Oxide Molecular Beam Epitaxy (MBE)

Professor H. Kroemer started his Nobel lecture by "Often, it may be said that the interface is the device". Many of the discoveries in semiconductor technologies are originated from physical phenomena happens in semiconductor interfaces. The introduction of interfaces into semiconductor and oxides materials produced variety of microelectronic devices exhibiting interesting physics.

After the invention of transistors and later the ability of integrating materials with exotic properties on to semiconductors, electronic devices and microelectronic technologies were critically dependent on the ability of growing additional materials on top of semiconductors in order to integrate their properties into the substrate for device applications. Intensive experimental research have started over the last years to grow oxide/semiconductor heterostructures using various deposition techniques such as atomic layer deposition (ALD), pulse laser deposition (PLD), chemical vapor deposition (CVD) and molecular beam epitaxy (MBE) [77-81].

However, integrating many of the properties of oxides into semiconductors proven to be very challenging, since the interface required to be abrupt, smooth and coherent. Oxide MBE chambers have been developed to grow high quality superconducting films and metal oxide semiconducting materials with a highly controlled oxygen background pressure. The ultra-high vacuum environment creates collision-free path for the evaporated beams of atoms. The key advantage of MBE in general, and oxide MBE in particular, is the ability of controlling the growth at the atomic level by turning the beams of atoms on and off instantly by opening or closing the shutters located between the evaporating cells and the substrate [82, 86]. Here, in this thesis, we have utilized custom built oxide molecular beam epitaxy to grow three different heterostructures on silicon, germanium and other single crystal oxide substrates with sharp and abrupt interface.

The work presented here was done using a custom-built oxide molecular beam epitaxy system located at the University of Texas at Arlington. Our MBE system is equipped with reflection high energy electron diffraction (RHEED) system and residual gas analyzer as in-situ monitoring equipment. The RHEED system is a very useful characterization technique to monitor the surface roughness and film quality. Shining a high energy beam of electrons in the range of 10-35 keV with an incident angle of few degrees with respect to the substrate surface provides the diffraction pattern on the phosphorous plate as shown in Figure 1.12 [83]. Monitoring the RHEED during the growth can immediately show the changes in the growth conditions such as surface reconstructions, film quality, off stoichiometry, etc. [83]. Since the incident angle of electrons are very small and the penetration depth is only few monolayers makes RHEED a very useful technique for studying the surface morphology.

In the growth mechanism, atoms gradually fill the vacant sites and form layers which are associated with RHEED intensity oscillations [85]. Scattered electrons coming off the substrate surface have different intensities depending on the surface roughness which can be used to determine the growth rate [84]. The schematic of the MBE system equipped with the RHEED is shown in Figure 1.13 below.

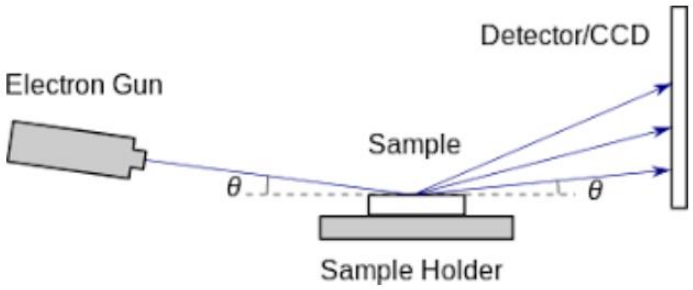

Figure 1.12: Reflected High Energy Electron Diffraction (RHEED) set up. [Braun, W. Reflection high energy electron diffraction during crystal growth. Springer, Berlin (1999)].

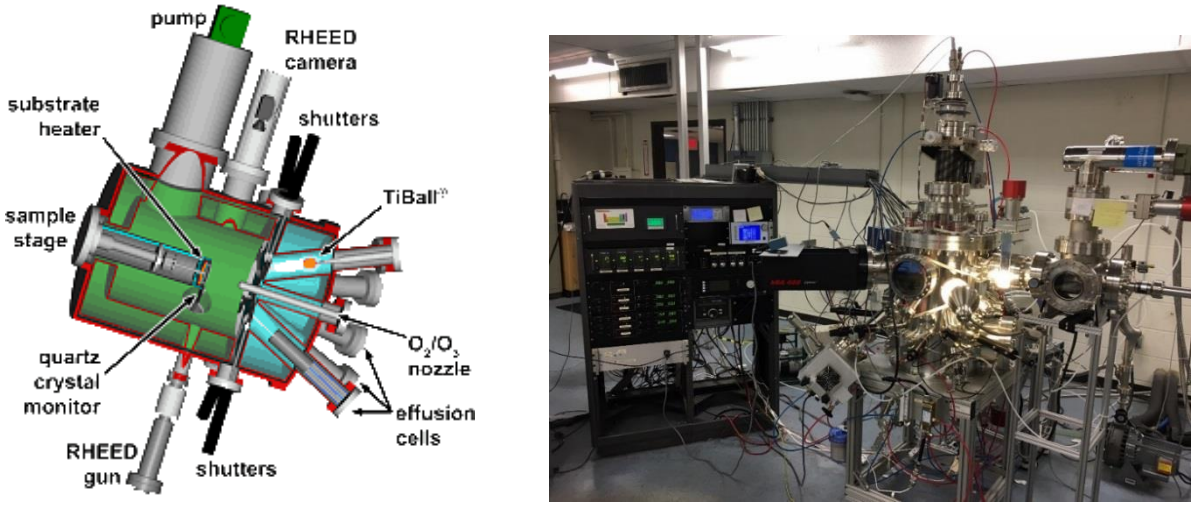

Figure 1.13: (a) Schematic of the Veeco GEN10 MBE chamber. (b) Custom built oxide-MBE at UTA.

1.5 Statement of originality

The three main research described in this thesis were collaborative in nature, hence I will summaries my role and contribution of others in research shown in chapter 2, 3 and 4. The STEM images shown in chapter 2 (Band gap engineering at crystalline oxide-semiconductor interface) were taken by X. Shen and D. Su from Center for Functional Nanomaterials Brookhaven National Laboratory. The band offset measurements and the reciprocal space mapping were performed by T. Droubay, S. A. Chamber and M. Bowden at Pacific Northwest National Laboratory. The XRD, CV and IV measurements were carried out with the help of M.J Moghadaam from UTA. In chapter 3 (Superconducting $SrTiO_3$ grown on $SrTiO_3$ buffered silicon) $SrTiO_3$ films were deposited (PLD) by our collaborators H. Zhang and T. We from University of Toronto. STEM images were done by X. Shen and D. Su from Brookhaven National Laboratory. In chapter 4 (Tuning MIT in $LaTiO_3$/

$SrTiO_3$ heterostructure on Si(001), I have used lab-view program written by Patrick Conlin and Ricky Hensley from UTA.

Some of the transport measurements were carried out with the help of Zheng Hui Lim and Mathew Chrysler from UTA. STEM images were taken by D. Su and H. Chen from Brookhaven National Laboratory and New York University Shanghai. Synchrotron X-ray diffraction and RSM were performed by D. P. Kumah and T. Chen at North Carolina State University. Dr. Ngai developed a code for Poisson-Schrodinger solver. Original code was provided by S. Ismail-Beigi.

Chapter 2

Band-gap engineering at a semiconductor-crystalline oxide interface

2.1 Introduction

Over the last decade, many studies have been carried out in order to improve microelectronic technologies with the help of utilizing new materials that exhibit novel functionalities [86-93]. One of the most promising approaches in realizing new material functionalities is coupling the properties of heterostructures with dissimilar yet complementary electrical properties [13,14]. In this regard, transition metal oxides are a perfect candidate due to their unique properties such as ferromagnetism, ferroelectricity, metal-insulator transitions, and other strongly correlated phenomena that are not achievable in traditional semiconductors. Integrating complementary properties is very important because traditional semiconductors also exhibiting properties such as higher mobilities and direct band line ups that are difficult to be realized in oxide materials. Consequently, integrating electrical properties of complex oxides and semiconductors enable us to achieve functionalities that cannot be realized independently in either material alone [13,93-98].

Among the complex oxides, transition metal oxides with perovskite crystal structures are believe to be the promising candidate for monolithically integrate on to conventional semiconductors. These perovskite oxides have smaller lattice mismatch with diamond and zinc blende semiconductor substrates such as Si, Ge and GaAs and therefore, can be directly grown on

these platforms. Epitaxial growth and characterization of these oxide materials as well as integrating their properties on to semiconductors are still a challenge [99]. Regardless of the ability to integrate crystalline oxides on semiconductors and create an epitaxial platform, electrically coupling these oxides have proven to be challenging due to the band offset between oxide and semiconductor. One approach to electrically couple oxide on semiconductors is band gap engineering in which the band gap of materials can be altered and tuned using composition modulation [100-104]. Band-gap engineering is a powerful technique for the design of new semiconductor materials and devices.

Artificial heterostructures along with advanced deposition techniques enable band diagrams with continuous band-gap variations to be created [104]. The band alignment of two semiconductors in contact can be categorized in three different lineups based on the position of their valence and conduction bands as portrayed in the Figure 2.1. The most common type of alignment is the "straddle alignment" or type-I in which the conduction band (valence band) of one semiconductor is above (below) the conduction (valence) band of the other one. The second type of band alignment is the "staggered lineup" or type-II in which the steps in the valence and conduction band go in the same direction and the third one is the most extreme band alignment, called "broken gap" or type-III [105,106,107].

For gate dielectrics, maximizing the conduction and valence band (VB) offsets in a type-I arrangement between the oxide and semiconductor is essential. Furthermore, minimizing the physical thickness of the oxide is also necessary

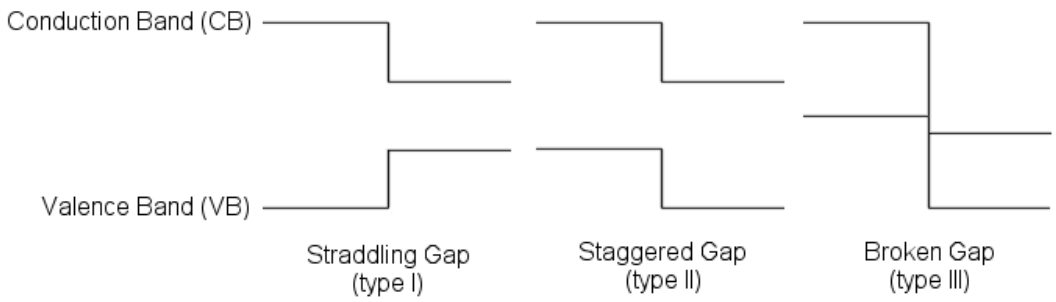

Figure 2.1: Types of energy band alignments: (left) Straddling gap or type-I, (middle) Staggered gap or type-II, (right) Broken gap or type-III.

2.2 Research objectives and motivations

Multifunctional oxides such as $BaTiO_3$ and $SrTiO_3$ are among the most studied transition metal oxides for possible replacement of SiO_2 gate dielectrics because of their low interface trap densities and high dielectric constants that could be realized via epitaxial growth. However, in real applications, integration of $SrTiO_3$ or $BaTiO_3$ on Si or Ge is not quite effective for device applications like insulating layer in field-effect devices, due to their band alignments with respect to Si or Ge or GaAs. [110,111]. Hence, tuning the band offset between oxide and semiconductor as well as their interface are two of the most critical challenges for oxide/semiconductors [108]. For instance, the band alignment between $SrTiO_3$ and conventional semiconductors is staggered, or type-II, where the conduction and valence bands of oxides are below the conduction band of semiconductors. This kind of energy gap line up is not appropriate for electrically coupling oxides onto semiconductors due to the high leakage current.

Comparable to $SrTiO_3$, the $BaTiO_3$ is equally unsuitable for electrically coupling onto the semiconductors. The $BaTiO_3$ conduction bands along with Si or Ge are almost aligned to the extent that prevents polarization of the multifunctional oxides to maintain accumulation or depletion in the semiconductors [103]. To couple ferroelectric features of oxides with semiconductors, the band alignment must be type-I [109-111]. This implies that the oxide's conduction band must be above the conduction band of semiconductor and the oxide valence band beneath the valence band of semiconductors, as presented in the Figure 2.2. Therefore, the main objective of this part of our research is to investigate the tune ability of band offset between transition metal oxide and semiconductor.

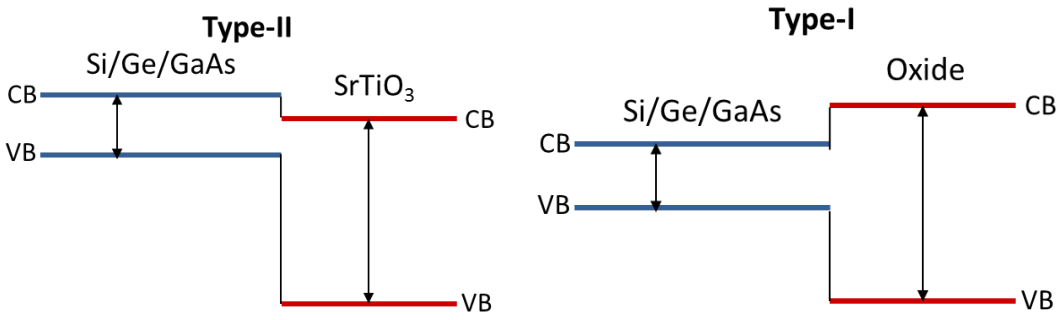

Figure 2.2: (Left) type-II band offset between oxide and semiconductor. (Right) type-I band alignment between the oxide and semiconductors.

Band gap engineering principles can be utilized to manipulate the band offset between single crystalline perovskite oxides and the Ge semiconductor platform [112]. Oxide molecular beam epitaxy chamber was used to form an atomically abrupt and coherent interface between crystalline perovskite oxide and *p-type* Ge substrate.

The solid solution of single crystalline $SrZr_xTi_{1-x}O_3$ *(SZTO)* was epitaxially grown and integrated directly on to Ge. The band-gap of the oxide is enhanced through increasing the Zr content *"x"* in the solid solution which resulted in formation of the inversion layer in the Ge as well as exhibiting reduced leakage current [113].

After successfully growing a series of *SZTO/Ge* heterostructures with *Zr* content ranging from $x = 0.2$ *to* 0.7, various structural and electrical characterization techniques were used to confirm the abrupt interface as well as enhanced band offset. The formation of atomically abrupt as well as coherent interface between crystalline oxide *SZTO* and the semiconductor Ge was confirmed by X-ray diffraction measurements. The RHEED was used in-situ for monitoring the 2-dimensional growth quality. A type-I band offset is confirmed via current-voltage (I-V) and capacitance-voltage measurements (C-V). High-resolution photoemission spectroscopy measurements verify that type-I offset has been achieved for heterostructures with higher Zr content. These findings prove that band-gap engineering can be manipulated to create multifunctional crystalline oxide/semiconductor heterojunctions in which a type-I band offset is achieved. In the following sections, details of the growth procedure and characterization methods will be discussed.

2.3 Epitaxial Growth of $SrZr_xTi_{1-x}O_3$ on *Ge* substrate

Several carefully designed steps were involved in epitaxially growing *SZTO* on Ge : first, chemical cleaning the Ge wafer (out-side the chamber). Next, achieving clean dimerized Ge surface (after introducing the wafer into UHV chamber). Then, calibrating the fluxes of *Sr, Ti and Zr* sources with high accuracy and monitoring the oxygen pressure during the growth to avoid formation of any unwanted secondary phases at the interface.

With the use of custom-built oxide MBE chamber functioning at a base pressure of $< 2 \times 10^{-10}$ Torr, the crystalline *SZTO* films were grown on *p-type Ge (100)* wafers (AXT Inc., $\rho \approx 0.02$ Ω.cm).

The chemical etching and surface cleaning were performed prior to the introducing Ge wafers into the growth chamber. Cleaning the Ge wafer is a two-step process including chemical etching out-side the chamber and the UHV annealing. Chemical etching encompasses the multiple dipping process into the acid to remove native oxide layer as well as organic and metallic contaminations. Later hydrogen peroxide was used to create a protective oxide layer on clean Ge surface [114-116]. The chemical process consists of dipping the Ge wafer into *HCl* 15% for 20 seconds as step one followed by dipping the wafer into H_2O_2 for 30 seconds as the second step. The steps are then repeated three times and for the third time, dipping is done in *HCl* 15% for 20 seconds followed by keeping Ge in the H_2O_2 for duration of 60 seconds. Ge is then rinsed using ultra clean DI water and subsequently dried with Argon gas to prohibit any additional chemical reactions [117]. After carefully chemical etched the substrate, Ge wafer was introduced in the MBE chamber. A clean dimerized Ge surface was acquired by thermally desorbing the resulting GeO_2 from the surface by annealing the wafer in UHV at 130 ^{o}C for half an hour and then substrate was heated up to ≈600 ^{o}C then cooled to room temperature.

All source materials were evaporated using the effusion cells and fluxes were calibrated using a quartz crystal microbalance (QCM). The retractable QCM arm was located near the substrate to measure the same flux arriving at the wafer. The QCM is a widely known technique for measuring and monitoring the film growth in which varying the mass of evaporated materials due the oxidation or thermal decay per unit area causing a change in the frequency of a quartz crystal resonator [118].

The Ge was then heated to around 450 °C, and half a monolayer of Sr was deposited. After cooling the Ge to room temperature. 1.5 monolayer of *SrO* and 2 monolayers of $Zr_xTi_{1-x}O_2$ were co-deposited in an oxygen background pressure of 3×10^{-7} Torr. The initial *1.5 ML SrO* was necessary to form a template for subsequent layers [14]. Then the substrate was heated to 550 °C to crystallize *2.5 unit-cells of SZTO*. Subsequently *3 unit-cells of SZTO* was deposited at the substrate temperature of ≈ 250 °C at oxygen background pressure of 3×10^{-7} Torr to reach total thickness of 38 unit-cells (~15nm). After each 3 unit cells samples were briefly annealed in vacuum to enhance the crystallinity. Finally, when the total desired thickness achieved the substrate was heated to ≈ 580 °C in UHV for several minutes to improve crystallinity. The growth was monitored in-situ using RHEED which each growth step shown Figure 2.3.

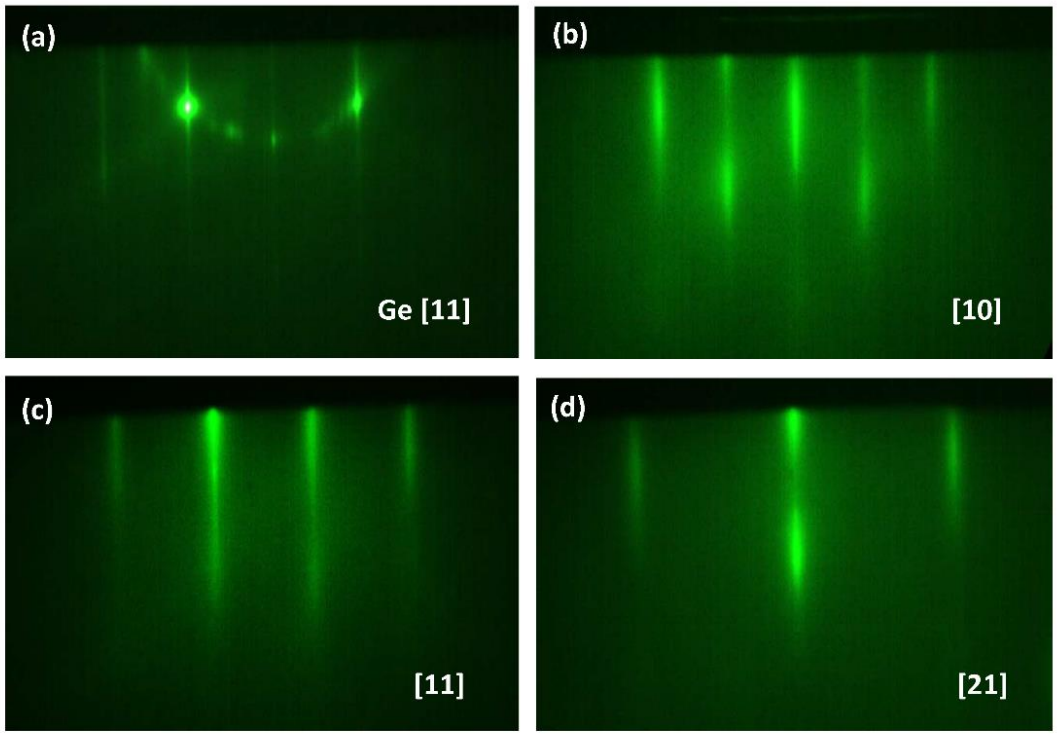

Figure 2.3. RHEED images taken (a) After 0.5 monolayers of Sr (b) The 38 unit-cell thick SZTO on Ge taken along [10] plus (c) [11] and (d) [21] directions.

2.4 Heterostructure Analysis

2.4.1 Structural characterizations

The X-Ray diffraction (XRD) method is used extensively in the characterization of thin film heterostructures given that it can reveal information regarding the lattice parameters of single crystals, crystalline phase, texture or even stress of polycrystalline materials [119]. The XRD measurements were done in a Bruker D8 thin-film diffractometer by using Cu Kα radiation. The XRD survey scan of various *SZTO* heterostructures with different *Zr* contents confirmed the single crystalline nature of our film grown on Ge, as shown in Figure 2.4 (a).

There are few remarks on the XRD results that must be explained in details. According to the Bragg's diffraction law, lower diffraction angles represent higher lattice spacing [119].

$$n\lambda = 2d\sin\theta$$

Where "λ" is the wave length of incident beam (Cu Kα), "d" is the lattice spacing and "θ" is the diffracted angle. A closer examination of the (002) peaks reveals that increasing the amount of *Zr* content resulted in peaks shifting to the left. In case of our heterostructure where *Ti* atoms replaced with *Zr* atoms, the shifted peaks indicating out of plane lattice constant expansion as can be seen in Figure 2.4 (b).

Zr ions have a larger atomic radius than the *Ti* ions resulting in an increase in c-axis lattice parameter. Theoretically, increasing the *Zr* will enhance the lattice match with *Ge* which improve the quality of the film. The crystal structure of *SZTO* is tetragonal considering the fact that on one side, $SrTiO_3$ has a perovskite cubic structure with a lattice constant of $3.905\ Å$ and the other end is a orthorhombic $SrZrO_3$ with larger lattice constant of $4.08\ Å$.

A summary of the effect of *Zr* content on out of plane lattice constant enhancement is provided in Figure 2.5. The lattice mismatch will increase the interface energy, as a result, system ultimately reduces the raised interface energy through formation of interfacial defects or by transforming the growth condition from 2-dimensional to more heterogeneous, or 3-dimensional mode.

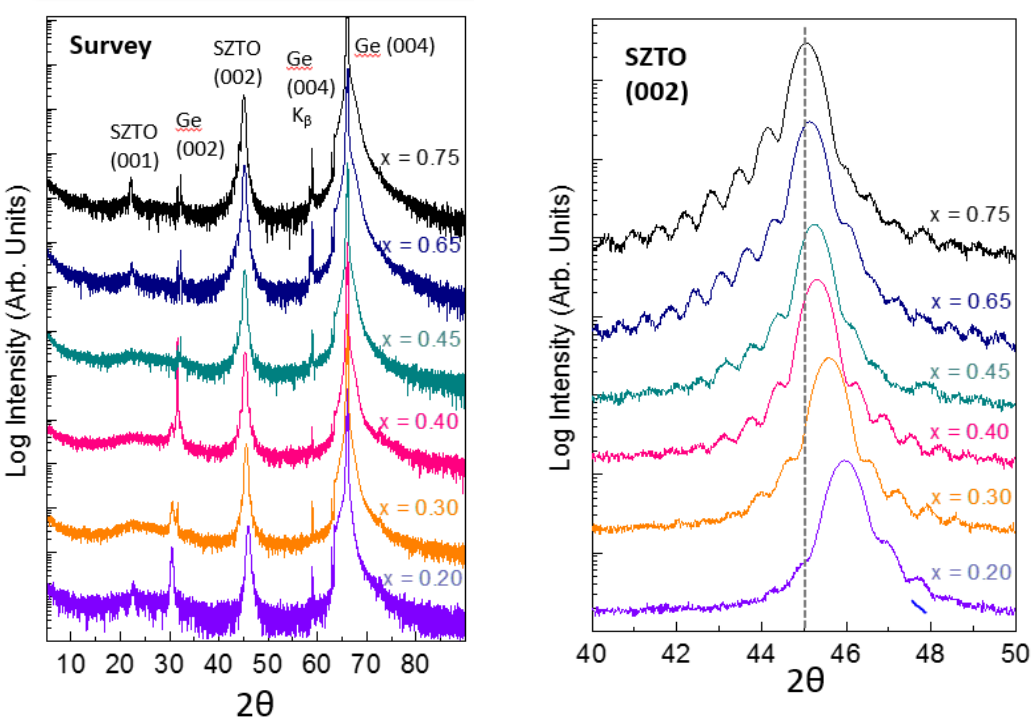

Figure 2.4. (Left) SZTO-Ge heterojunctions survey scan for various x confirms the single crystalline nature of the heterostructure. (Right) A shift in the (002) peak observed with increasing Zr content showing expansion of the out-of-plane lattice constant

As discussed earlier, the monotonic expansion of lattice constant with increasing Zr content results in a smaller lattice mismatch between *Ge*/*SZTO* heterostructure and higher interface quality along with abrupt and coherent interface.

The FWHM profiles extracted from the XRD data can demonstrate valuable information about the microstructure modulations and stress–strain buildup in the heterostructure [120]. As it was previously predicated, higher Zr content showing narrower FWHM angle compared to the lower Zr content "x" with wider FWHM values. The measured FWHM ranging from $\Delta\omega \approx 0.39^0$ to $\Delta\omega \approx 0.65^0$.

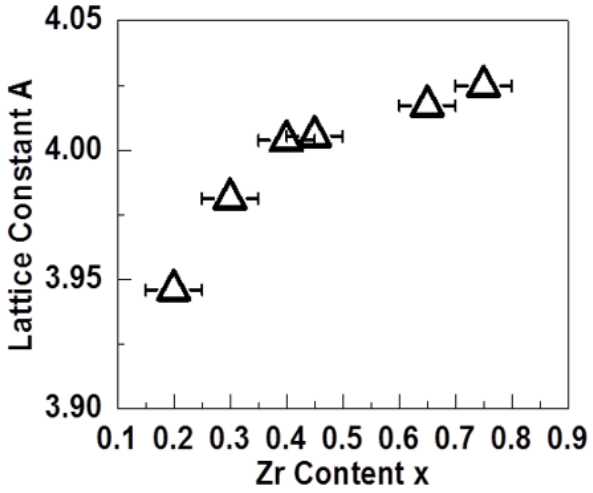

Figure 2.5: An increase in the Zr content will bring about an increase in lattice constant

Atomic force microscopy (AFM) is a commonly used technique for measuring the surface roughness in which the voltage variations in the tip of the cantilever were translated into the image and presented as a topographical map of the surface. AFM results also confirm the lattice match enhancement through increasing the *Zr* in the heterostructures which exhibit a smoother surface with roughness of less than < 1nm as shown in the Figure 2.6 below.

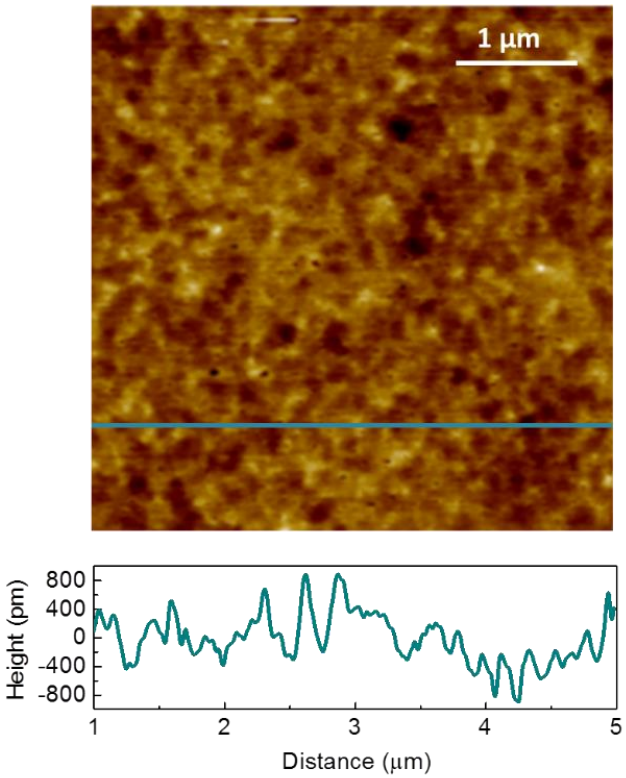

Figure 2.6: Atomic force microscopy image of a typical SZTO-Ge sample (x = 0.70) displaying surface roughness of less than 1 nm

It is important to note that the heterostructures remained largely strained with respect to the *Ge* substrate confirmed by the reciprocal space mapping with $Zr = 0.65$ as shown in the Figure 2.7. Since the data translated into the real space phase, the round shape of *Ge* peaks in real space mapping data represent the cubic structure of Ge whereas a slight upward shift of *SZTO* can be attributed to the larger lattice constant of *SZTO* and elongation along the *c-axis*. The Ge lattice parameters were multiplied by $\sqrt{2}$ to allows for direct comparison of the Ge diamond cubic unit-cell with perovskite SZTO as well as accommodation for the 45^0 rotations of heterostructure epitaxially grown Ge.

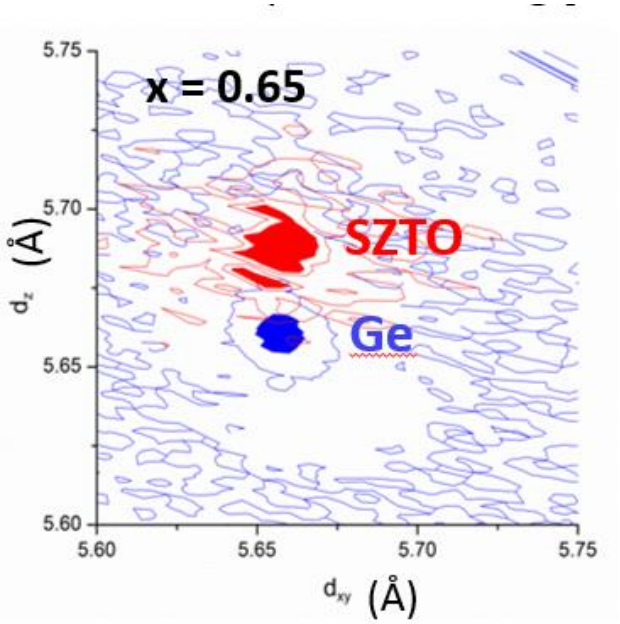

Figure 2.7: Direct-space map of a x = 0.65 SZTO-Ge heterojunction).

Two additional characterization measurements were done on the heterostructure with Zr content x = 0.7 for the purpose of confirming the quality of the interface along with the abruptness of the heterojunctions. Scanning transmission electron microscopy (STEM) and electron energy loss spectroscopy. Scattered electrons from the sample can be used to form a *Z-contrast* image showing atomic locations as well as elemental compositions. The ability to provide two-dimensional maps using STEM image is complementary to measurements based on X-rays, revealing any surface termination or inter-diffusion at the oxide/semiconductor interfaces as well as any local deviation at defects such as dislocation, stacking faults and antiphase boundaries [121]. The scanning transmission electron microscopy (STEM) measurements offer atomic scale images of single crystalline *SZTO* and Ge interface. The STEM cross-sectional specimens along [110] direction of Ge was prepared by our collaborators at Brookhaven National Laboratory. Figure 2.8 revealed atomically abrupt and structurally coherent interface.

It is important to point out that there exist no amorphous GeO_x interfacial layers or any secondary phases at the interface confirming the growth quality and sharp interface. The result of *Z*-contrast in in high-angle annular dark field image (HAADF) is especially clear due the close atomic mass of *Zr and Sr* [122].

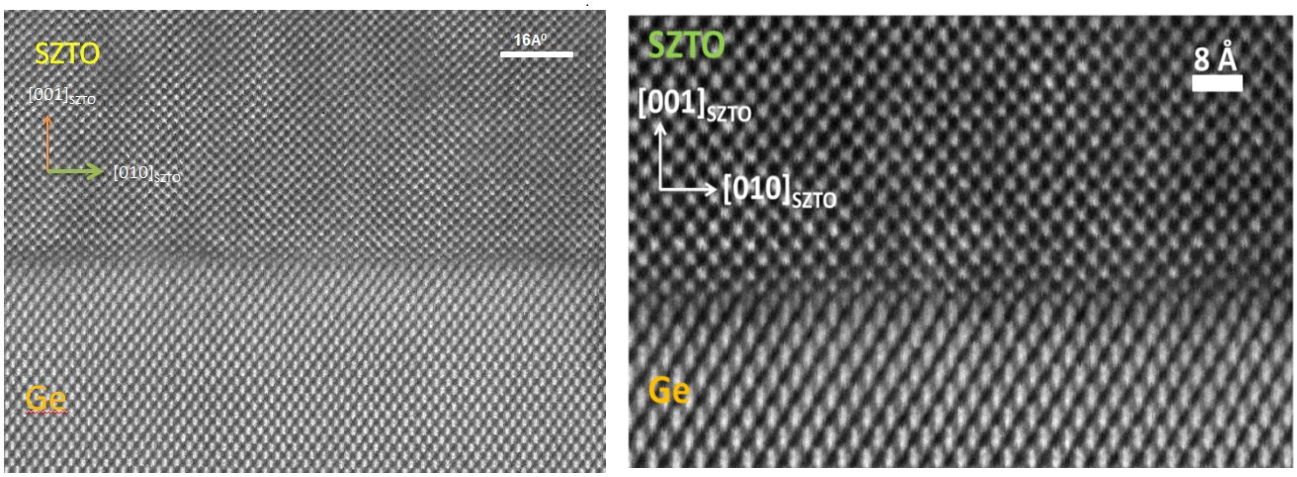

Figure 2.8. STEM characterization of single crystalline SZTO x = 0.70 Ge (100) interface. The interface of SZTO and Ge is atomically abrupt as well as structurally coherent.

Electron energy loss spectroscopy line scans also confirms the abruptness of the *SZTO/Ge* interface. The main advantage of using the electron energy loss spectroscopy is the ability of studying the atomic scale migrations at the interface [123]. Our *SZTO/Ge* heterostructure have an abrupt interface in which *Ti, O and Ge* inter-diffusion at the interface were below 1 nm as indicated from the electron energy loss spectroscopy spectrum (Figure 2.9).

The electron energy loss spectroscopy data showing a very narrow diffusion area that can be interpreted as an abrupt interface between *SZTO* and *Ge* substrate. As discussed earlier in this chapter and chapter one, two key parameters in integrating oxide on semiconductors were coherent interface and the band offset. So far with the help of various structural characterization techniques, it has been confirmed that the interface between *SZTO and Ge* is atomically abrupt and coherent. Now it is time to turn to electrical characterization to investigate the band alignment enhancement in our heterostructure.

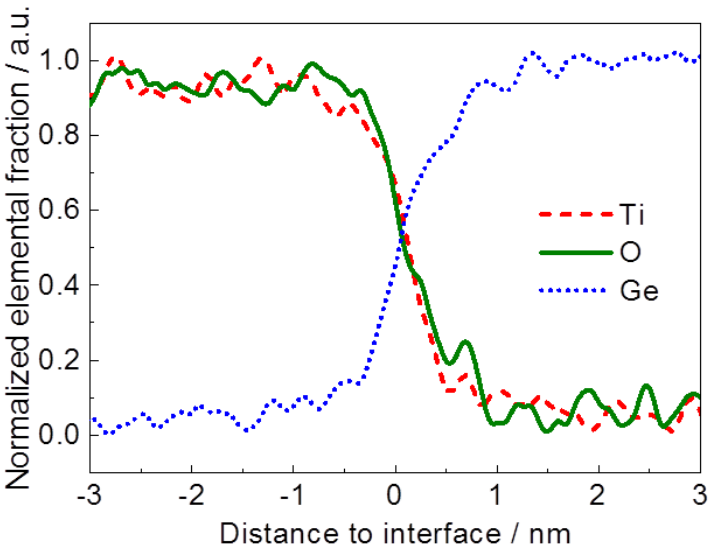

Figure 2.9: EELS line-scan of the interface along [001] direction, displaying elemental fraction of Ti, O along with Ge.

2.4.2 Electrical characterizations

Prior to discussing the electrical measurements, a brief background of *MOS* capacitors and phrases commonly used in I-V and C-V measurements are explained here: The *MOS* capacitor comprises of a Metal-Oxide-Semiconductor structure as depicted by Figure 2.10.

The semiconductor substrate with a thin oxide layer as well as a top metal electrode known as the gate is shown. An Ohmic contact to the rear of the semiconductor is formed by using counter electrode [124].

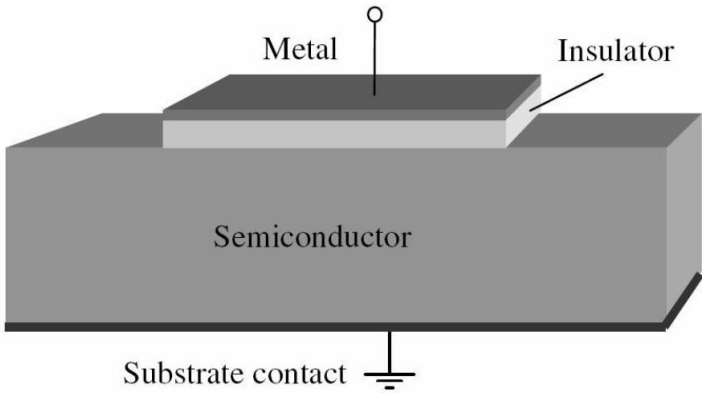

Figure 2.10: MOS capacitance structure.

There are four main bias modes that can be applied to a *MOS* capacitors. Depending on the voltage applied on the metal contact there are (a) accumulation (b) flat band (c) depletion and (d) inversion, as shown in Figure 2.11. Flat band condition occurs when the energy band of oxide and semiconductor is flat and the surface electric field is zero as shown in Figure 2.11 (b). The applied bias in the flat-band condition is called V_{fb} which is the difference between the Fermi levels. If the negative bias keeps increasing, the energy bands of the *p-type substrate* bending upward which results in an accumulation of holes at the interface, this condition is known as surface accumulation (shown in Figure 2.11 (a). Another scenario happens when applying the positive voltage to the gate. In this case the energy bands of the oxide bend downward and majority carriers (holes) pushed away from the surface known as the depletion region as shown in Figure 2.12(c). Interesting phenomena occur when increasing the positive bias at the gate, since all the majority carriers (holes in case of p-type substrate) pushed away from the surface, the carrier types will be change at a critical voltage known as threshold voltage (V_T).

The band bending continues to the point that the surface inverted from p-type to n-type. This condition is called inversion as shown in Figure 2.12 (d) [125].

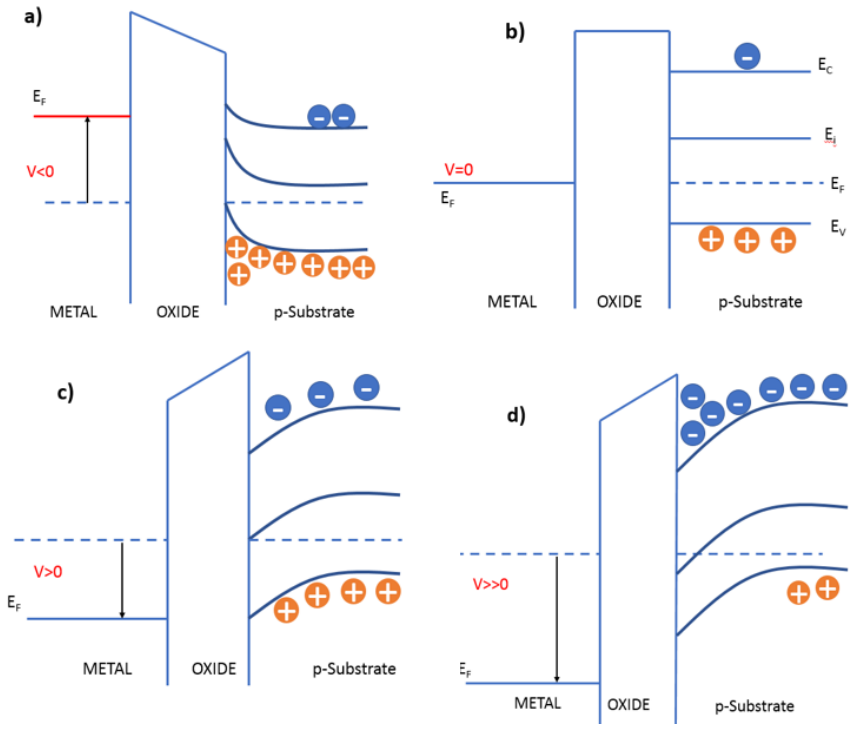

Figure 2.11: The energy band diagrams in (a) accumulation, (b) flat band, (c) depletion, and (d) inversion for a MOS capacitor

2.4.2.1 Current-Voltage analysis

Our *SZTO* film epitaxially grown on *p-type Ge* substrate can be consider as a *MOS* capacitor where *30 nm Ni* electrode pads were deposited by electron beam evaporation technique to create metal gate and the back side of the wafers were mechanically scratched using a diamond scribe. InGa eutectic applied to create a counter electrode as shown in Figure 2.12.

In order to compare the effect of *Zr* content (*B-site substitution*) on the band alignment of *SZTO* films grown on Ge (001), identically thick *(15nm)* $Ba_{0.4}Sr_{0.6}TiO_3$ *(BST)* films *(A-site substitution)* were also grown under the same chamber conditions on *p-type Ge*. Prior to electrical characterization, all the heterostructures were annealed in wet oxygen at 350 ^{o}C for half an hour to improve the interface quality and remove the oxygen vacancies and [126,127].

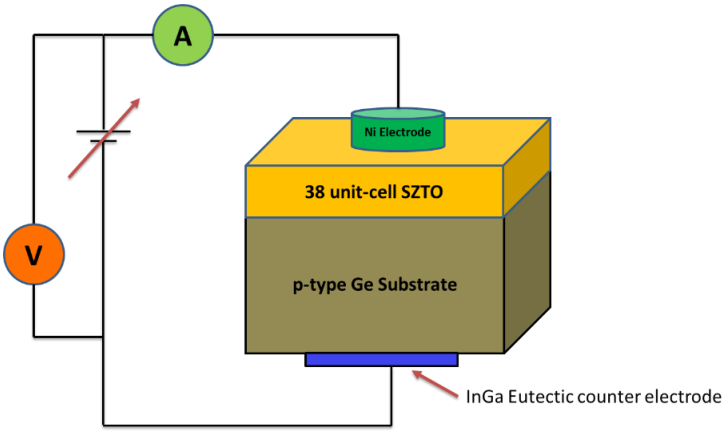

Figure 2.12: Schematic of the I-V set up.

It is important to note that low temperature annealing did not cause formation of any secondary phases like GeO_x at the interface as confirmed by the post-annealing STEM image shown in Figure 2.13 which indicates an atomically abrupt and coherent interface [127].

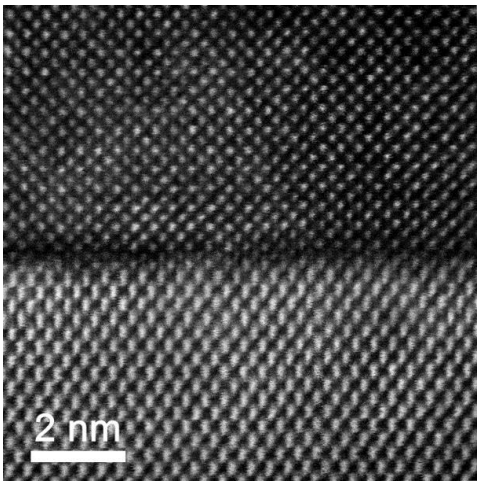

Figure 2.13. STEM image of a SZTO x = 0.70 sample after annealing in wet oxygen.

The current-voltage measurements were carried out on both *BST* and *SZTO* heterostructures (x = 0.25-0.7). The current-voltage measurements can reveal the improvement in leakage current as well as band offset enhancement in *SZTO* heterostructure. The I-V was done on a Micromanipulator 8060 probe station using flexible, 10-micron radii tungsten probe whiskers and the current-voltage measurements were performed via ramping the current applied to the Ni electrode from 0 to +3 V and 0 to -3V by means of Agilent 4155 C. Figure 2.14 shows the I-V characteristics of both *BST* and *SZTO* heterostructures in which the current density plotted versus applied voltage. *BST* has a type-II band offset with respect to *Ge* that brings about higher leakage current compared to *SZTO/Ge* heterojunction as shown in Figure 2.14. The continuous reduction of leakage current in *SZTO/Ge* heterojunctions arise as a result of the formation of type-I band offset.

There are a few remarks appeared on the *I-V* curves that must be explained. The asymmetry in the *I-V* plots in positive and negative bias around the zero voltage can be attributed to the barrier height difference between *Ni electrode* and the *p-type Ge* substrate [128]. It is important to mention that substituting the *Sr* metal with *Ba* did not have a profound effect on the leakage current whereas increasing the *Zr* content as *a B-site* substitution improved a leakage current more than an order of magnitude. The remaining leakage currents that can be seen in Figure 2.14 mostly originated from the residual oxygen vacancies that did not annihilated during the wet annealing. These point defects can act as n-type dopant which increase the overall leakage of carriers in *SZTO* heterojunctions [128].

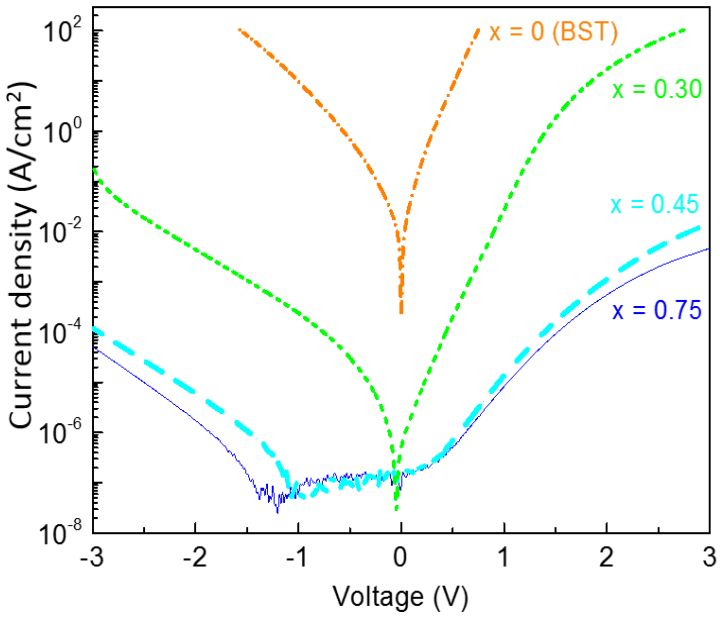

Figure 2.14: I-V curves of SZTO/Ge and BST/Ge heterojunctions.

2.4.2.2. Capacitance -Voltage analysis

Following the confirmation of the creation of type-I band offset in *SZTO*/*Ge* heterostructure utilizing the I-V measurements, capacitance-voltage (C-V) measurements were performed to additionally confirm the type-I band offset as well as compute the dielectric constant of *SZTO*. Capacitance-voltage measurements offer important information regarding the band alignment. Prior to discussing the CV measurements, a brief background of MOS capacitors C-V response are explained here: The capacitance–voltage measurement is a powerful and accurate method to estimate the oxide thickness as well as calculating the flat band and threshold voltages. In most common C-V set up, a DC bias applied through the gate along with an AC signal and the response recorded by AC meter [125]. As discussed earlier, a MOS capacitor showing three different responses depending on the voltage polarity and the magnitude of the applied voltage (accumulation, depletion and inversion).

The *MOS* capacitor responds differently with frequency. At low frequencies known as quasi-static conditions, the generation rate of carriers in the depleted surface layer is fast, therefore, carriers have enough time to swept to the interface to create a sheet of charge whereas in a high frequency situation, the generation rate is not fast enough, thus carrier do not have time to respond to the high frequency [125]. The *MOS* capacitor consist of a series combination of fixed oxide capacitance and voltage dependent semiconductor capacitance. Hence, the most important parameter in determining the overall *MOS* capacitor is the amount of bias applied on the *MOS* capacitor. The ideal *MOS C-V* characteristics in various bias is shown in Figure 2.15 for a p-type substrate. The maximum *MOS* capacitance can be calculated in accumulation using the equation below:

$$C_{accumulation} = C_{MOS} = C_{Max} = \varepsilon_{OX} / t_{OX}$$

Where ε_{OX} is the permittivity of the oxide and t_{OX} is the oxide thickness.

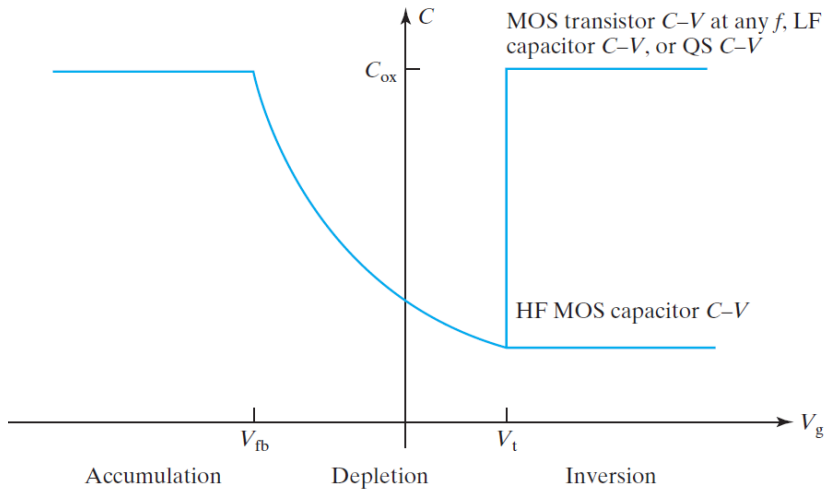

Figure 2.15: MOS capacitor C-V characteristics with high and low frequencies [125].

The C-V measurements were carried out on our heterostructures at different frequencies using Agilent 4284A LCR meter and Micromanipulator 8060 probe station with flexible tungsten probe whiskers. Figure 2.16 shows a C-V response of our heterostructure at various applied frequencies ranging from 5KHz to 1MHz. As it can be clearly seen from the plot, the inversion layer was created in *SZTO-Ge* heterostructure (x = 0.7). *Zr* substitution modifies the band offset from type-II to type-I in *SZTO/Ge* heterostructures. Without the formation of type-II band offset, the carriers would leak into the substrate in which the inversion layer never formed.

There are few remarks on the C-V curves that need to be explained. The calculated flat band voltage showing the shift to the left. This flat band shift is consistent with presence of positive charge at the interface which originated form the oxygen vacancies at the interface [129-131]. Knowing the oxide film thickness (~15nm) and measured capacitance in accumulation (1.7×10^{-6} Fcm $^{-2}$), enabled us to estimate the dielectric constant of our heterostructure using the MOS capacitor equation. The dielectric constant of the *SZTO* was approximated to be $\kappa_{SZTO} = 29$ (in accumulation at 1 MHz) which is very close to the dielectric constant of bulk $SrZrO_3$ (≈ 30) and is comparable to some of the highest dielectric constants among gate materials reported [132,133].

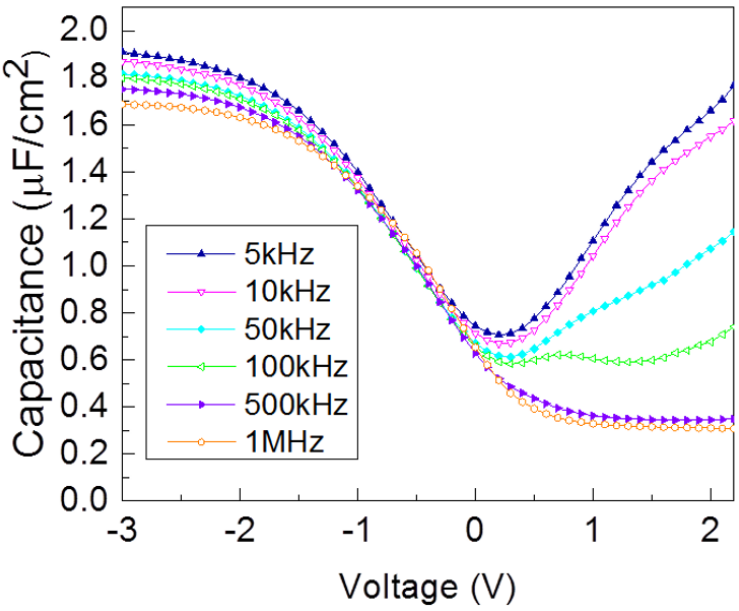

Figure 2.16: C-V characteristics of SZTO/Ge heterostructure (x = 0.70).

2.4.3 Quantifying the Band Offset

Additional measurements involved quantifying the band offset between the *SZTO* and *Ge* using high-resolution core-level(C_L) and the valence band (V_B) X-ray photoemission spectroscopy (*XPS*) measurements on a x = 0.65 heterostructure. XPS is a characterization method that can study a sample to nanoscale depth as well as revealing chemical elements and their bonds at the surface. XPS is very sensitive characterization technique to revealing the electron behavior in the valence band and oxidation state of the compound. X-ray photoemission spectroscopy measurements were carried out at Pacific Northwest National Laboratory (PNNL). To determine the valence band offset (V_{BO}) of our heterostructure, core level and valence band spectra were used for clean Ge and both thin (6 u.c) and thick (38 u.c) *SZTO/Ge* films with Zr content of x = 0.65 [135,136].

The energy from the top of the V_B to the Sr $3_{d5/2}$ core peak of thick *SZTO* (38 u.c.) was measured to be 130.59eV. Similarly, the energy from the top of the V_B to $E_{Ge3d5/2}$ core peak of clean *Ge* was measured to be 29.52 eV. The core level binding energy of Ge and Sr was measured to be 104.27 eV. Finally, the valence band offset was measured to be $\Delta E_{V=}$ 3.2eV.

(1) $(E_{Sr3d5/2} - E_V)_{SZTO:}$ *130.59eV*

(2) $(E_{Ge3d5/2} - E_V)$ *Ge = 29.52eV*

(3) $(E_{Sr3d5/2} - E_{Ge3d5/2})_{HJ}$ *= 104.27(2) eV.*

(4) $\Delta E_V = (E_{Sr3d5/2} - E_{Ge3d5/2})_{HJ} + (E_{Ge3d5/2} - E_V)$ *Ge* $- (E_{Sr3d5/2} - E_V)$ *SZTO = 3.20(8) eV.*

Following the Vegard's law, the conduction band offset in our heterostructure with *Zr = 0.65* is calculated to be 0.91 eV which is an agreement with achieving type-I band offset. Figure 2.17 summarized all the calculations above.

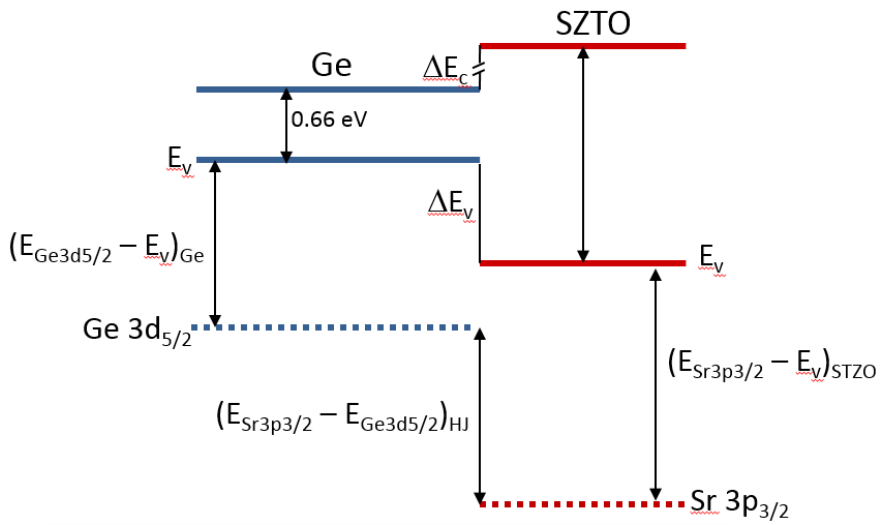

Figure 2.17: Band diagram showing conduction and valence band offsets for a x = 0.65 SZTO-Ge heterojunction.

2.5 Potential Applications & Conclusion

Previously, intermediate buffer layers like rocksalt structured materials AeO were used to engineer a type-I band offset with respect to semiconductor platform [131]. The unpredictability of the rocksalt/perovskite stacks in which AeO layer can react with $AeTiO_3$ make epitaxially growth and integration of AeO layers very challenging [138]. Moreover, rocksalt structured materials have low dielectric constants which make them an unfavorable candidate for gate dielectrics. Additionally, AeO materials are known to be unstable in ambient conditions. Therefore, our method of enhancing the band gap between crystalline oxides and semiconductors through creating a *SZTO* solid solution proved to be a more reliable method in integrating oxide on semiconductors since the band offset can be tuned through changing *Zr* content and avoid the mixing of rocksalt as intermediate buffer layer with perovskite. In the *SZTO* solid solution, increasing the *Zr* content (B-site substitution) modified both the band gap and crystallinity (less lattice mismatch with Ge), while A-site substitution mainly impacts only the lattice constant.

It has been confirmed that *SZTO* thin films can be a possible replacement for a gate dielectric in the field-effect devices due to its high dielectric constant and its stability. Other than functioning as a candidate gate dielectric, *SZTO* can also function as an electrical as well as epitaxial platform for integrating multifunctional crystalline oxides on semiconductors. Single crystalline *SZTO* films have a potential to be utilized as a tunnel barrier in spintronic applications in which spin-polarized carriers from a half-metallic oxide can be injected into a semiconductor [137]. The solid solution *SZTO* can also function as an intermediate layer to mitigate the leakage of carrier from ferroelectric to semiconductor by maintaining the accumulation or inversion. Figure 2.18 schematically summarize some of the potential applications of *SZTO* solid solution.

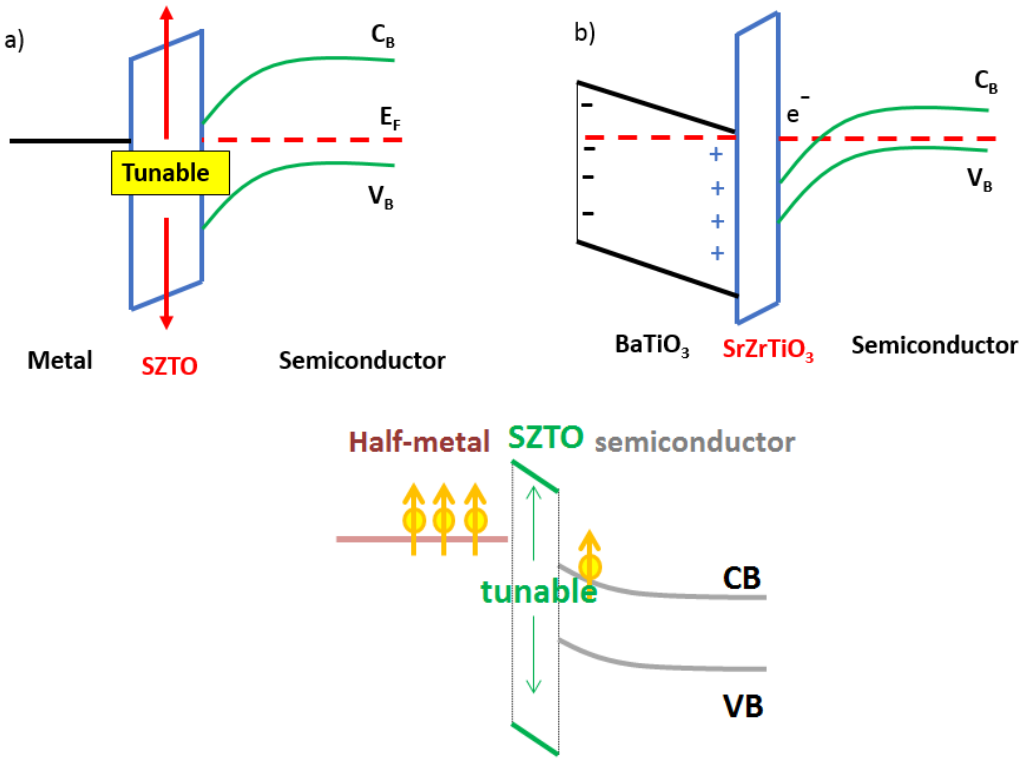

Figure 2.18: (a) SZTO as a gate dielectric for field effect devices. (b) SZTO as Ferroelectric for ultra-low power, and non-volatile logic, (c) Ferromagnetic: Spin-injection (Spintronics/Opto-spintronics)

Summary

Here we applied principals of band gap engineering to change the band offset between single crystalline $SrZr_xTi_{1-x}O_3$ integrated directly on Ge from type-II to type-I through varying Zr content x. X-ray diffraction measurements confirmed the single crystalline nature of the heterostructure. STEM images confirmed the abrupt and coherent interface with no secondary phases existing at the interface. Electrical characterizations such as C-V and I-V measurements confirmed the formation of type-I band offset in our heterojunctions. The band offset calculated to

be around 0.91eV using XPS. A dielectric constant, estimated to be around 29 extracted from C-V data which is among the highest reported so far for gate materials. Finally, single crystalline SZTO directly integrated on Ge can be utilized as an electrical platform for device applications such as a gate dielectric, ferroelectric and ferromagnetic devices.

Chapter 3

Superconducting epitaxial $YBa_2Cu_3O_{7-\delta}$ on $SrTiO_3$ buffered *Si (001)*

3.1 Introduction

The changes in technology along with the increasing demand for electronic devices have prompted the researchers to search for novel materials having new properties with the intention of creating new functionalities. It has been indicated that the complex transition metal oxides exhibit exotic materials properties and thus regarded as a likely choice for future electronic applications [14]. These properties such as ferroelectricity, magnetism and superconductivity can be integrated into oxide-semiconductor heterostructures for device applications like microelectronic, sensing and energy harvesting technologies [139].

One of the most interesting and technologically relevant properties of complex transition metal oxides is superconductivity in which material exhibit zero resistance below a transition temperature [140-145]. In 1911, superconductivity was first observed in Hg in which resistivity dropped when cooling down to 4 Kelvin. Superconductivity was under extensive research for finding new materials or compounds to exhibit superconductivity at higher temperature. Eventually M. K. Wu et al. found the first compound (a copper oxide $YBa_2Cu_3O_7$) which exhibits superconductivity above the boiling point of liquid nitrogen. Since then, many research have been carried out to utilize $YBa_2Cu_3O_7$ for possible device applications.

3.2 Literature Review & Motivation

Cuprate systems are one of the most exciting class of transition metal oxides due to their interesting properties such as superconductivity. There are more than 40 different types of cuprate systems with various copper-oxygen planes. Among all copper-oxide compounds, superconducting $YBa_2Cu_3O_{7-\delta}$ is the most studied system due to its higher transition temperature as well as the ability of fabricating in the form of thin films [146]. The ability of growing single crystalline $YBa_2Cu_3O_7$ on dissimilar compounds open a new pathway to investigate for integrating its properties on to different materials [147].

Superconducting $YBa_2Cu_3O_7$ have many important applications such as infrared detectors, filters and superconducting quantum interface devices (SQUID) [140-148]. For many technological applications single crystalline films exhibit higher transition temperature and narrower transition widths are preferred [149,150]. However, growing single crystalline $YBa_2Cu_3O_7$ is challenging since $YBa_2Cu_3O_7$ is mostly grown on single crystalline substrates like $SrTiO_3$ and $La_{0.18}Sr_{0.82}Al_{0.59}Ta_{0.41}O_3$ *(LSAT)*, which are very costly and cannot be fabricated in large sizes. Additionally, growing single crystalline $YBa_2Cu_3O_7$ on technologically relevant platforms like silicon is proven to be very difficult since growing single crystal $YBa_2Cu_3O_7$ requires high temperature which cause inter-diffusion and formation of polycrystalline phases.

In this regard, different deposition method like magnetron sputtering [151-154], pulsed laser deposition (PLD), laser ablation, molecular beam epitaxy, chemical vapor deposition (CVD), metalorganic deposition (MOD), and metalorganic chemical vapor deposition (MOCVD) [155–161], were utilized to grow $YBa_2Cu_3O_7$ on silicon which resulted in low transition temperature and wide transition widths. To mitigate inter-diffusion in growing $YBa_2Cu_3O_7$, buffer layers were

introduced at the interface to minimize the lattice mismatch and chemical reaction between superconducting $YBa_2Cu_3O_7$ and the substrate.

Some of the most common compounds that are used as intermediary buffer layers were : ZrO_2, MgO, SiO_2, Y_2O_3/YSZ, $MgAl_2O_4$, CeO_2, RuO_2, $CoSi_2$, and $BaTiO_3/MgAl_2O_4$ [161-170]. The film quality, interface coherency and intermediate layer thickness are key parameters that have proven to be successful in reducing the inter-diffusion and increasing the transition temperatures from 55 K to 88 K. Therefore, the main objective of this chapter is to create an epitaxial platform to act as a buffer layer to integrate superconducting $YBa_2Cu_3O_7$ on to silicon to exhibit higher transition temperature as well as narrower transition width with no inter-diffusion in $YBa_2Cu_3O_7/Si$ films. This achievement is important for future device technology since epitaxial $YBa_2Cu_3O_7$ can be integrated on silicon instead of single crystalline expensive substrates. Hence, oxide molecular beam epitaxy chamber was utilized to grow single crystalline $SrTiO_3$ as a buffer layer on a silicon (001) substrate, then single crystalline $YBa_2Cu_3O_7$ was deposited using pulse laser deposition method as shown schematically in Figure 3.1. After successfully growing $YBa_2Cu_3O_7$ *on* $SrTiO_3/Si$, various characterization methods were used to determine the interface quality and the transport properties of the heterostructure.

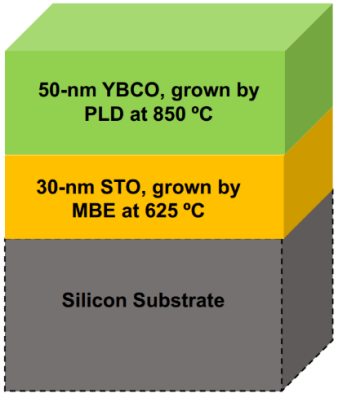

Figure 3.1: 30 nm STO grown on Si (001) using MBE, and 50 nm YBCO grown using PLD.

3.3 Step 1, Growing Epitaxial $SrTiO_3$ on Silicon

The 30 nm $SrTiO_3$ buffer is grown on undoped, 0.5 mm thick, 2" diameter (001)-oriented Si wafers (resistivity of 14–22 Ω.cm MTI) using reactive MBE in a custom-built chamber operating at a base pressure of < 2 x 10^{-10} Torr. In order to remove residual organic materials from the substrate surface, the Si wafer was exposed at ambient temperature to activated oxygen for ten minutes in UHV. The activated oxygen was produced by breaking the O_2 molecules to oxygen ions using radio frequency plasma source operating at 220 W in an O_2 background pressure of 5 x 10^{-6} Torr which result in a formation of a native layer of SiO_x on the surface. In order to remove the native oxide layer formed from the previous step, 2 monolayers (ML) of *Sr* metal was deposited at a substrate temperature of 560 ^{0}C.

All source materials were evaporated using thermal effusion cells (VEECO, SVT Associates) and fluxes were calibrated using a quartz crystal microbalance (QCM Inficon). Shutters were located near the evaporating cells to achieve atomic level control of the arriving materials towards the substrate. The silicon substrate was rotating at a constant speed throughout the growth to achieve a uniform deposition rate. A clean *Si* surface was obtained by heating the substrate to 860 ^{0}C in which *SrO* was desorbed from the Si surface evidenced by a 2 x 1 surface reconstruction monitored by RHEED [170]. In the next step, sufficient amount of *Sr* was deposited to achieve half monolayer *Sr* coverage at a substrate temperature of 660 ^{0}C to create necessary templates for subsequent layers [14]. Next, 1.5 *ML* of *SrO* and *2 ML* of TiO_2 were co-deposited at ambient temperature and then heated up to 500 ^{0}C to crystallize and form 2 unit-cells of crystalline $SrTiO_3$.

Fluxes were then re-calibrated to be 1:1 ratio and additional $SrTiO_3$ layers were deposited at a substrate temperature of 625 ^{0}C in a background O_2 pressure of 3 x 10^{-7} Torr. Reflected high

energy electron diffraction was used during the growth to monitor the film quality. Strong RHEED intensity along the [10], [21] and [11] directions and streaky nature of the diffracted patterns confirm the high crystal quality and 2-dimesnional epitaxial growth of 30 nm $SrTiO_3$ on silicon as shown in Figure 3.2(a-d). Atomic force microscopy also confirms the smooth surface resulting from a 2-dimensional growth mode of the $SrTiO_3$. The surface roughness was measured from a line profile of AFM to be less than 1nm as shown in Figure 3.2 (e) and (f).

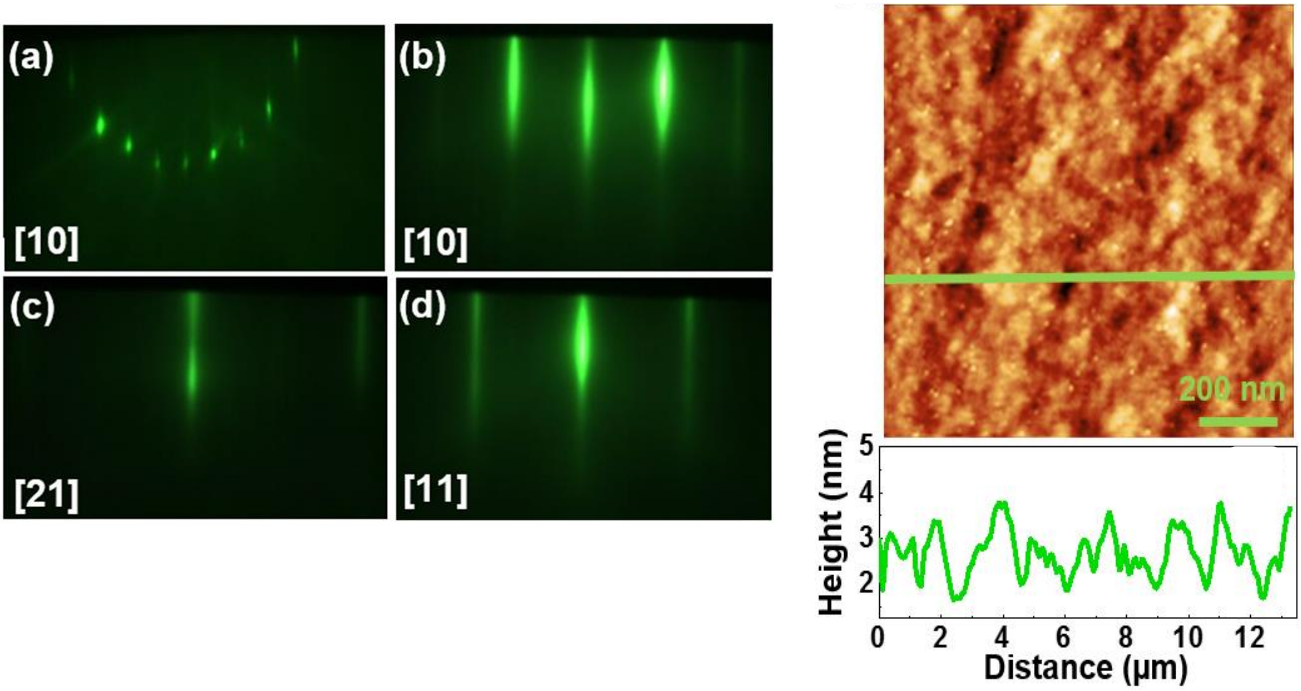

Figure 3.2: (a) RHEED patterns of clean Si along [10] direction; (b) After 30 nm STO grown epitaxially on Si (001) taken along [10] and (c) [21] and (d) [11] directions. (e) AFM image of 30 nm STO on Si (001). (f) The surface morphology confirms 2-dimenssional growth.

3.4 Step 2, Growing $YBa_2Cu_3O_7$ using Pulse Laser Deposition

After growing 30 nm epitaxial $SrTiO_3$ *on Si*, wafers were taken out of the chamber and broken into smaller 5 × 5 mm pieces and transported in ambient condition to a PLD chamber. Pulse laser deposition is a known technique for growing complex oxides such as $YBa_2Cu_3O_7$. The PLD is a simple technique in principle where high power laser used for evaporating materials from a target to deposit them on the substrate as schematically depicted in Figure 3.3 [171]. Some of the advantages of using pulse lase deposition method are:

1. Stoichiometric and complex compounds can be deposited in PLD.
2. Relatively precise thickness control and fast growth rate.

The $YBa_2Cu_3O_7$ growth using PLD was done at University of Toronto. Prior to PLD deposition of $YBa_2Cu_3O_7$, samples were glued on to a contact heater using Ag paste. The substrate is then heated to 850 ^{0}C in a background O_2 pressure of 200 mTorr, at which the $YBa_2Cu_3O_7$ is deposited by striking a stoichiometric polycrystalline target with a laser. The stoichiometric *YBCO* target is situated ~ 6 cm from the substrate and is continuously rotated during deposition. After growth, the PLD chamber is back-filled with 1 atm of O_2 and the $YBa_2Cu_3O_7$ film is slowly cooled to 300 ^{0}C at a rate of 12 ^{0}C/min, and then cooled to room temperature.

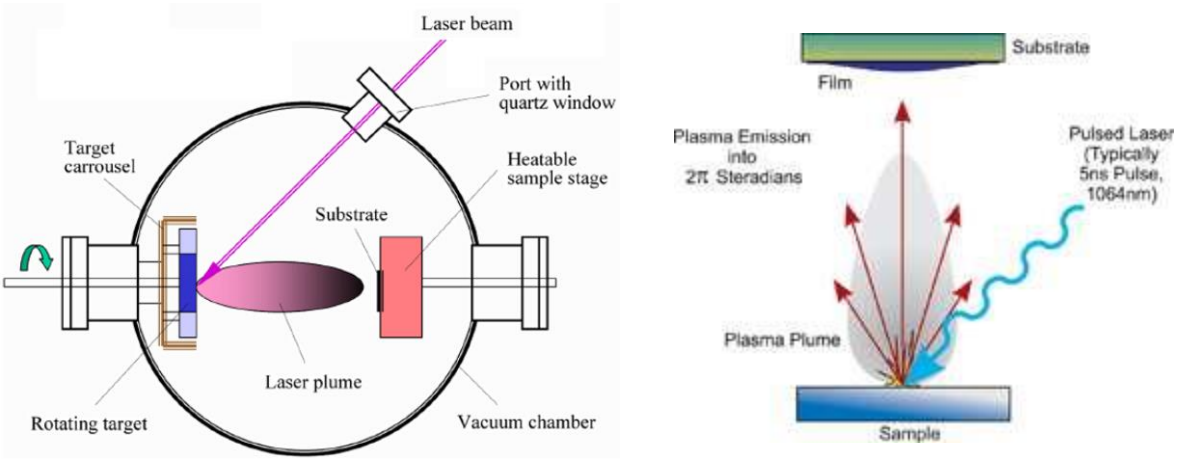

Figure 3.3 Schematic view of PLD-system [Oxford Instrument].

After successfully growing $YBa_2Cu_3O_7$ *on* $SrTiO_3/Si$, the next step is to study the quality of the interface using some of the advanced characterization techniques such as high resolution transmission electron microscopy (HRTEM) and scanning transmission electron microscopy (STEM) imaging which provide real-space structural characterization of the $YBa_2Cu_3O_7/SrTiO_3/Si$ heterostructures.

Figure 3.4(a) shows a HRTEM image of the combined stack comprised of 50 nm of $YBa_2Cu_3O_7$ grown on 30 nm of $SrTiO_3$ *on Si*. As it can be seen from the image ~ 5 nm thick layer of SiO_x situated between the *Si* substrate and $SrTiO_3$ buffer. The formation of the oxide layer at the interface can be attributed to the high temperature required to grow $YBa_2Cu_3O_7$ which results in oxygen diffusion through the $SrTiO_3$ to the $SrTiO_3/Si$ interface. Scanning transmission electron microcopy images confirmed the atomically abrupt and coherent interface between 30 nm $SrTiO_3$ and silicon even after growing 50 nm $YBa_2Cu_3O_7$ and formation of the oxide layer.

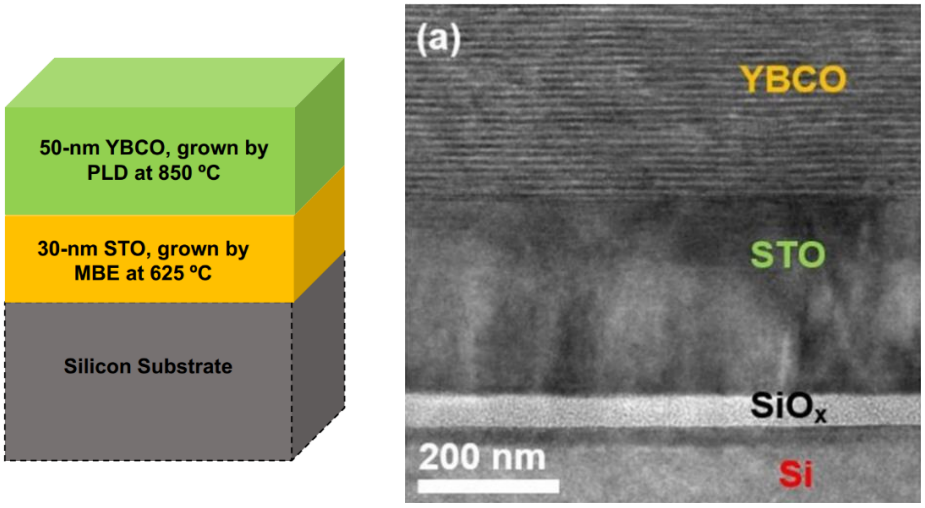

Figure 3.4: (a) HRTEM image of the YBCO/STO/Si heterostructure with SiO_x layer.

3.5 Interface Analysis and Structural Characterizations

High resolution transmission electron microscopy was utilized to investigate the growth quality and the interface between $SrTiO_3/Si$ and $YBa_2Cu_3O_7/ SrTiO_3$. The HRTEM imaging indicate the thickness of the $SrTiO_3$ still remained 30 nm despite formation of SiO_x layer. $YBa_2Cu_3O_7$ film exhibiting c-axis oriented growth and the interface between superconducting $YBa_2Cu_3O_7$ and buffer layer $SrTiO_3$ remained abrupt, revealed by the high angle annular dark-field image shown in Figure 3.7(b) and (c).

Higher growth temperature and excess oxygen in $YBa_2Cu_3O_7$ during the PLD growth resulted in the formation of some distortion and modulation in the spacing between adjacent $YBa_2Cu_3O_7$ layers as indicated by arrows in Figure 3.4 (b). Line profile analysis of the 50nm $YBa_2Cu_3O_7$ grown on $SrTiO_3$ buffered Si using contact mode atomic force microscopy confirmed 3-dimensional growth as shown in Figure 3.5 [172].

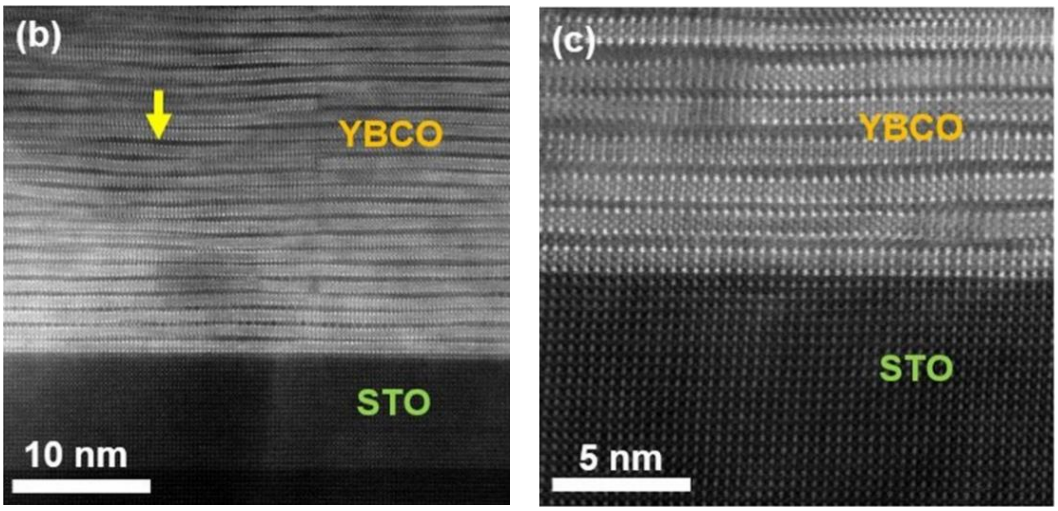

Figure 3.4: (b) STEM image of YBCO on STO buffer (c) STEM image of the atomically abrupt interface between the YBCO and STO buffer

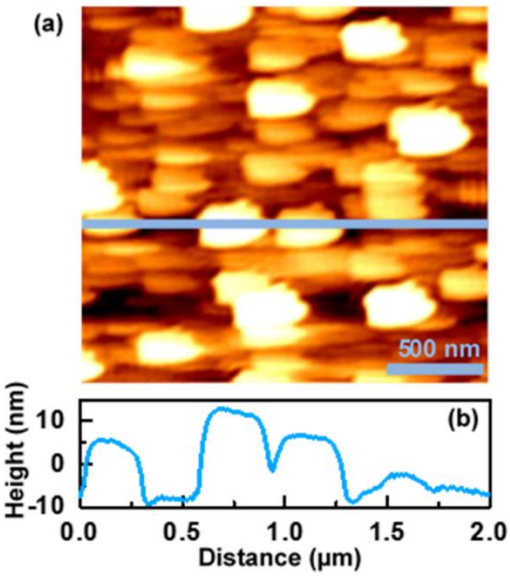

Figure 3.5: (a) AFM image of a YBCO on STO buffered Silicon. (b) Line-profile analysis of the surface roughness

X-ray diffraction analysis on the 50 nm thick $YBa_2Cu_3O_7$ film revealed the single crystallinity of the heterostructure. The XRD results confirm a c-axis oriented epitaxial growth of $YBa_2Cu_3O_7$ crystal; samples were characterized at room temperature, using the Bruker D8 X-ray Diffractometer. Thin film Nickel filter monochromator was used to filter Cu-K_β and retain Cu-$K_{\alpha 1}$ (λ=1.54056 nm) and Cu-$K_{\alpha 2}$ (λ=1.544 nm) radiation. Data were recorded in the wide range ($5^\circ < 2\theta < 95^\circ$) with the step size of 0.01 and time per step of 1.0 second in order to observe low angle *YBCO* peaks. The divergence and anti-scatter slits were both 1.0 mm. Figure 3.6 shows the XRD pattern with wide angle peaks from [001] to [0011] and a peak located at $2\theta \sim 44^0$ indicated by the asterisk which can be originated from the presence of silver compound. The extracted out of plane lattice constant of 50 nm $YBa_2Cu_3O_7$ is estimated to be around c = 11.66 Å which is comparable to the c lattice constant of bulk $YBa_2Cu_3O_7$.

In order to determine the effect of 30 nm single crystalline $SrTiO_3$ as a buffer layer, identically thick 50 nm $YBa_2Cu_3O_7$ was grown directly on a single crystal $SrTiO_3$ substrate using PLD under the same conditions. One of the extremely useful techniques to study the film quality, strain, layer thickness and lattice mismatch is the rocking curve method. The $YBa_2Cu_3O_7$ grown on $SrTiO_3$ buffered silicon shows a slightly larger full-width half maximum ($\Delta\omega = 0.85^0$) compared to $YBa_2Cu_3O_7$ grown directly on a single crystal $SrTiO_3$ substrate ($\Delta\omega = 0.65^0$) as shown in the inset of Figure 3.6.

The difference in full width at half maximum (FWHM) values can be attributed to the lattice mismatch between $YBa_2Cu_3O_7/SrTiO_3$ and $YBa_2Cu_3O_7/SrTiO_3/Si$. Growing $YBa_2Cu_3O_7$ *on* $SrTiO_3$ buffered *Si or* $YBa_2Cu_3O_7$ grown directly on $SrTiO_3$ enhanced the FWHM values which is largely attributed to the difference in c lattice constants between the $SrTiO_3$ and the $YBa_2Cu_3O_7$ [14,173].

Generally, heterostructures that we have grown, experiencing compressive strain which result in formation of dislocations to minimize the surface energy known as "mosaicity". For instance, the $SrTiO_3$ film growing on silicon exhibit much smaller FHWM values ($\Delta\omega = 0.40^0$) due to the smaller lattice match and smaller interfacial strain.

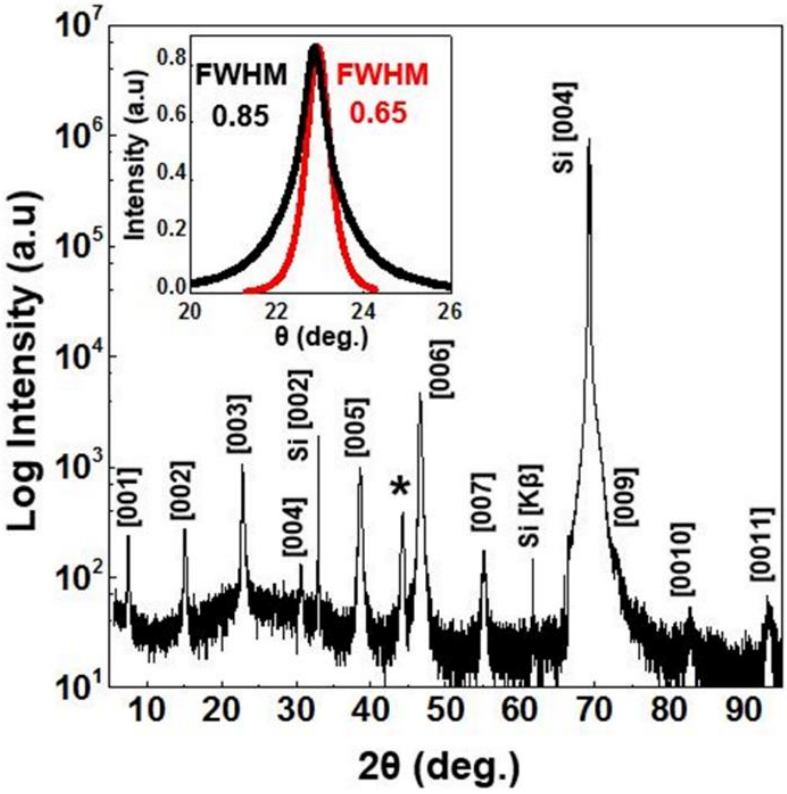

Figure 3.6: XRD of a YBCO/STO/Si heterostructure. Rocking curve of the YBCO grown on STO buffered Si (001) is shown in the inset (black). For comparison, the rocking curve of a 50 nm thick YBCO film grown on STO single crystal substrate is also shown (red).

So far structural characterization confirmed the abrupt interface between $SrTiO_3$ and silicon substrate as well as 3-dimenssional growth mode in $YBa_2Cu_3O_7$. After confirming the crystallinity of the heterostructure using XRD, RHEED and STEM imaging, electrical characterization of $YBa_2Cu_3O_7$/ $SrTiO_3$/*Si* films were investigated by our collaborators at the University of Toronto

using transport measurement technique to determine the transition temperature of the thin film epitaxially grown on silicon.

3.6 Transport Measurements and Electrical Characterizations

One of the most common transport measurement techniques to determine the low temperature electrical properties of materials is a four-point measurement. The four-point probe is a widely used technique to measure the sheet resistance of thin layers. The electrical transport measurements were performed using a standard AC lock-in technique on 1 × 5 mm samples in a 4-point geometry. Prior to the transport measurements, 15 nm thick Au contacts were deposited on the sample surface using DC magnetron sputtering (shadow mask) then conducting leads (lines) were connected in-line using silver wires.

Transport analysis revealed high T_c's and narrow transition widths for our *50 nm* $YBa_2Cu_3O_7$ grown on *30 nm* $SrTiO_3$ buffer layer on Si (001). Figure 3.7 shows the resistivity plotted versus temperature for both $YBa_2Cu_3O_7$ on $SrTiO_3$ buffered silicon and $YBa_2Cu_3O_7$ directly on a single crystal $SrTiO_3$ substrate. In transport data, the critical temperature (T_c) was defined as the temperature at which zero resistivity was recorded.

As can be clearly seen from the inset of the Figure 3.6, the T_c value of the $YBa_2Cu_3O_7$ film deposited directly on single crystal $SrTiO_3$ substrate (~ 90 ± 0.5 K), is lower than the $YBa_2Cu_3O_7$ grown on $SrTiO_3$ buffered silicon (93 ± 0.5 K). The extrapolated zero temperature residual resistivity of the *YBCO* film grown on $SrTiO_3$ buffered *Si* is about 110 Ω.cm which is higher than $YBa_2Cu_3O_7$ on $SrTiO_3$ single crystal (~ 75 Ω.cm). The *RRR* is defined as the resistivity of the material at room temperature over the estimated resistivity at zero Kelvin. The *RRR* is directly

dependent on crystal quality, defects and inelastic scattering. Commonly, higher *RRR* value can be attributed to a higher impurity in the crystal structure or the interface. The $YBa_2Cu_3O_7$ film grown on $SrTiO_3$ buffered silicon the extrapolated *RRR* value is around ~16 whereas the *RRR* value for the $YBa_2Cu_3O_7$ grown directly on $SrTiO_3$ substrate is ~9. The enhanced *RRR* can be originated from couple of reasons: as discussed earlier, $YBa_2Cu_3O_7$ film grown on silicon was experienced more compressive strain compared to $YBa_2Cu_3O_7$ grown on $SrTiO_3$. The excessive compressive strain resulted in a formation of mosaicity due to higher lattice mismatch.

In addition to the mosaicity, the SiO_x layer in the $YBa_2Cu_3O_7$ film grown on $SrTiO_3$ buffered silicon is another source of scattering. Consequently, higher *RRR* value calculated for $YBa_2Cu_3O_7$ film on silicon can be attributed to higher density of defects and scattering.

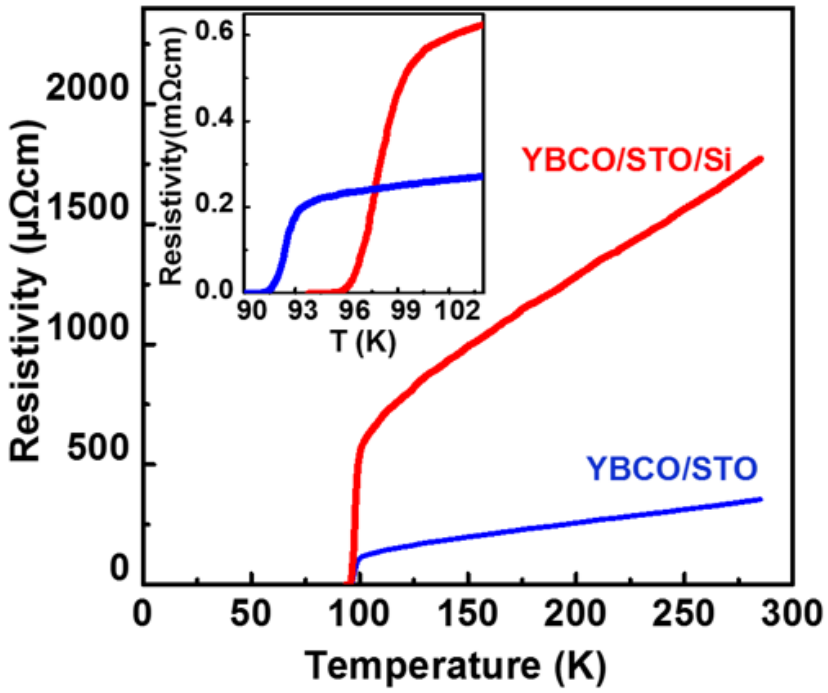

Figure 3.7: Transport characterization of YBCO/STO/Si (red) and YBCO/STO (blue) heterostructures

3.7 The Origin of Higher "T_c"

Growing a single crystalline $SrTiO_3$ buffer layers using MBE, followed by growing $YBa_2Cu_3O_7$ using PLD are the main reasons to achieve a higher T_c as compared to previously reported values for $YBa_2Cu_3O_7$ grown on Si. Hereof, it is important to understand why $YBa_2Cu_3O_7$ grown on *STO* buffered *Si* exhibits higher T_c than same thickness $YBa_2Cu_3O_7$ film grown directly on $SrTiO_3$ substrate. The enhanced T_c could be attributed to several separate mechanisms involved in growing $YBa_2Cu_3O_7$ *on* $SrTiO_3$ buffered *Si*.

According to structural analysis, superconducting $YBa_2Cu_3O_7$ grown on 30 nm buffered silicon exhibits more mosaicity which can be explained by generating more dislocations. These dislocations can facilitate the oxygen flow through the heterostructure. Additionally, previous studies have shown silver inclusion (seen in the XRD data) can increase the amount of oxygen reaching the $YBa_2Cu_3O_7$ [37-40]. Consequently, higher T_c reported for $YBa_2Cu_3O_7$ grown on $SrTiO_3$ buffered silicon could originate from the improved oxygenation happening during the growth. Single crystalline $SrTiO_3$ grown epitaxially on Silicon with MBE is proven to be a reliable platform to integrate superconducting $YBa_2Cu_3O_7$ films. The stability of 30 nm $SrTiO_3$ on silicon under ambient conditions without any protective layer makes it an ideal candidate to be used as platform for other deposition techniques like sputtering which can enable growth of $YBa_2Cu_3O_7$ on larger sized wafers.

Chapter 4

Tuning metal-insulator behavior in $LaTiO_3/SrTiO_3$ heterostructure integrated directly on *Si (100)* through control of atomic layer thickness

4-1 Introduction & Motivation

Since the invention of transistors and entering the computer era, science and technology have mainly focused to develop cheaper, faster, smaller and energy-efficient products. In this regard, understanding the materials behavior at a smaller scale is of great fundamental and technological importance for electronic devices. Multifunctional oxides are among the most exciting candidates for future device applications due to their exotic properties that were explained in details in previous chapters.

Among multifunctional oxides, transition metal oxides that exhibit strongly correlated phenomena are of great interest due to their unique properties such as strong electron-electron correlation, high carrier density, superconductivity, magnetism and metal insulator transition [175,185]. The ability of growing oxide heterostructures with atomic level precision utilizing molecular beam epitaxy enables us to introduce strong electron-electron correlation phenomena at the interface through varying the thickness of oxide layers and manipulating the electronic stability of heterostructures [176-184].

Transition metal oxides such as rare-earth titanates are a perfect example of filling control metal-insulator (FC-MI) Mott systems in which transitions are driven by carrier density. Depending on the thickness of the heterostructure, carrier density can be modulated in different ways. Oxide heterostructures such as bulk rare-earth titanates allow for external control of properties through the manipulation of carrier concentration through changing composition while carrier density in thin film can be modified using field effect [180,185,190]. In this regard, achieving Mott-driven MI behavior in oxide heterostructures and integrating this phenomenon on the most technologically relevant platform (silicon) through highly controlled growth processes are of great interest for future applications in device technologies such as information processing and sensing.

In this chapter, electrical and structural characterization of metal-insulator behavior in oxide heterostructures integrated directly on silicon were investigated. The system that we explore consist of a wide band gap insulating $SrTiO_3$ and a Mott insulator $LaTiO_3$ epitaxially grown on un-doped Si (001) using oxide-MBE system. Both $SrTiO_3$ *and* $LaTiO_3$ share the same perovskite crystal structure. $SrTiO_3$ is a band insulator with an empty *d-band and* Ti^{4+} valence, whereas $LaTiO_3$ is a Mott–Hubbard insulator with one *d-electron* per-site and titanium valence of Ti^{3+} [191-195].

Over the last decade perovskite oxides such as $SrTiO_3$ have gained a lot of attention due to its ability to form a two dimensional electron liquid (*2DEL)* with high carrier densities at the interface. The mechanism of formation of a *2DEL* in these type of oxide interfaces is different from the mechanism observed in other semiconductor systems like $Al_xGa_{1-x}As$ */ Ga As* in which a *2DEL or 2DEG* is formed due to the band bending at the quantum well interface.

Interfaces between $RTiO_3$ (R is a trivalent rare earth ion) and $SrTiO_3$ such as $LaAlO_3/SrTiO_3$, $LaTiO_3/SrTiO_3$, $GdTiO_3/SrTiO_3$, $LaTiO_3/KTaO_3$ etc. exhibit a polar discontinuity at the interface in which high-density mobile carriers mitigate the raised electrostatic potential energy created by polar/none polar interface [193-200]. The band insulator $SrTiO_3$ is composed of neutrally charged SrO (A-site) and TiO_2 (B-site) planes whereas polar $RTiO_3$ oxides are composed of $R^{+3}O^{-2}$ planes with (+1 charge) that transfer charge to $SrTiO_3$ (0.5 electron per unit cell) as shown in Figure 4.1. This mechanism of charge transfers due to polar discontinuity (polar catastrophe) is known as electronic reconstruction [196-200].

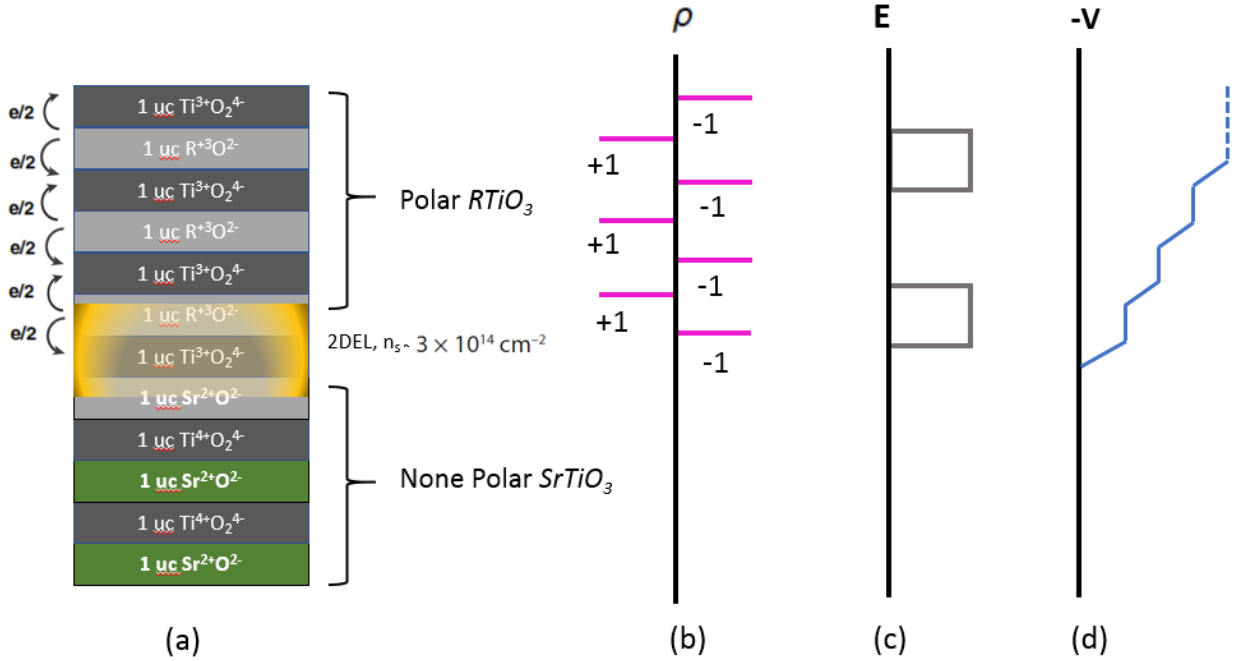

Figure 4.1: (a) Schematic showing the formation of a 2DEL at a polar/ none polar oxide interface formed between $SrTiO_3$ and $RTiO_3$ oxides. (b) Charge distribution in LTO/STO, (c) electric field in the heterostructure and (d) Potential build up.

A perfect example of forming a *2DEL* due to charge transfer is the system that we have explored in this chapter namely $LaTiO_3$ *and* $SrTiO_3$, in which variation in titanium valence at the $LaTiO_3$/ $SrTiO_3$ interface will result in a formation of electron liquid at the $SrTiO_3$ layer as shown in Figure 4.2.

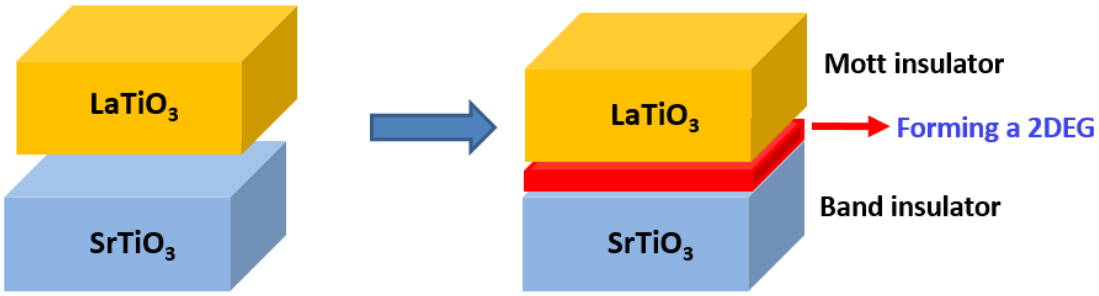

Figure 4.2: The formation of 2-dimenssional quasi electron liquid at the $LaTiO_3$/ $SrTiO_3$ *interface.*

In this research, various characterization techniques and theoretical approaches were carried out to explain the metal-insulator transition in $LaTiO_3$/ $SrTiO_3$ heterostructures in which increasing the thickness of $SrTiO_3$ layers will result in an emergence of metal-insulator transition. The metallic behavior in the heterostructure can be explained by Fermi-Liquid behavior, while reducing the thickness of the $SrTiO_3$ channel between silicon and $LaTiO_3$ will result in carrier-carrier enhancement and therefore give rise to insulating behavior that can be described by activated transport. The manipulation of Mott metal-insulator behavior in oxides grown directly on Si opens the pathway to harnessing strongly correlated phenomena in device technologies.

4.2 Methodology

4.2.1 Growth Mechanism & Structural Characterizations

The $LaTiO_3/SrTiO_3$ heterostructures consist of 3 layers: a bottom layer of $SrTiO_3$ that is *n* unit-cells (u.c.) thick, an intermediary layer comprised of 3 u.c. of $LaTiO_3$ and a top layer comprised of *1.5 u.c.* $SrTiO_3$, as illustrated in the schematic of Figure 4.1.

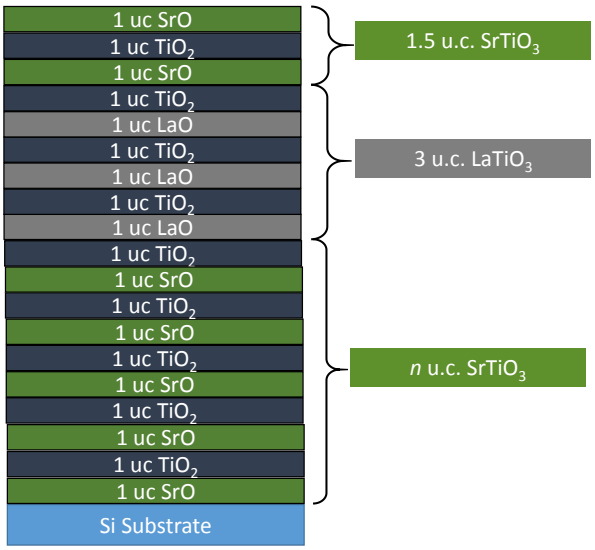

Figure 4.2: Schematic representation of the $LaTiO_3/SrTiO_3/Si$ *heterostructures.*

The $LaTiO_3/SrTiO_3/Si$ heterostructures were grown in a custom built oxide molecular beam epitaxy chamber operating at a base pressure of $< 2 \times 10^{-10}$ Torr. Prior to film deposition, undoped 2" diameter Si (100)-oriented wafers (Virginia Semiconductor) were cleaned by exposing to activated oxygen generated by a radio frequency source (VEECO) to remove residual organics from the surface. Then, two monolayers of *Sr* metal (fluxes calibrated by QCM) deposited at a substrate temperature of 550 °C, which was subsequently heated to 870 °C to remove the SiO_x layer. Surface reconstructions *(2 x 1)* captured by in-situ RHEED confirmed a clean, dimerized

silicon surface. Then enough *Sr* was deposited at 660 °C to achieve a total of half monolayer *Sr* coverage which is a very crucial step to form a template for subsequent layers [14].The substrate was then cooled to room temperature, at which *3 ML of SrO* and *2 ML* of TiO_2 were co-deposited at room temperature. In the next step, the substrate was heated up to 500 °C to crystallize *2.5 unit-cells of* $SrTiO_3$. Then *Sr and Ti* fluxes were re-calibrated to 1:1 ratio and following layers of $SrTiO_3$ of various thicknesses were co-deposited at a substrate temperature of 500 °C. All the fluxes were calibrated using quartz crystal microbalance mounted on the retractable arm and located near the substrate surface to capture and measure the same flux reaching the wafer.

The single crystalline $SrTiO_3$ film was A-site terminated due to the initial *SrO* monolayer, therefore, prior to depositing $LaTiO_3$ layers, a single monolayer of TiO_2 was deposited to form a B-site terminated growth, which minimizes intermixing of *Sr and La* during the $LaTiO_3$ growth. Later, single crystalline $SrTiO_3$ was briefly annealed at 580 °C to improve crystallinity just before depositing $LaTiO_3$ layers. The oxygen background pressure (3×10^{-7} Torr) was kept constant for all grown films, as measured by an ion gauge situated away from the substrate. This oxygen level prevents the formation of insulating phases such as $La_2Ti_2O_7$.

Finally, 7 nm of amorphous silicon was deposited as a capping layer on all heterostructures at room temperature to protect underneath oxide layers. Since the amorphous Si was deposited at room temperature, no structural changes occurred in our heterostructures due to the capping layer. Figure 4.3 (a) and (b) show typical post-growth RHEED images taken along the [10] and [11] crystal directions.

In order to determine the interface quality, Scanning transmission electron microscopy imaging was used. The HAADF image of the heterostructures confirmed the atomically sharp and coherent interface, as shown in Figure 4.3(c) and (d). The $LaTiO_3$ is heavier than $SrTiO_3$ *and*

silicon, hence it is brighter in STEM image due to the fact that, heavier elements scatter more electrons and the HAADF detector capture more signal whereas lighter elements like oxygen can be detected by low angle or medium angle detectors (less intense scattering)

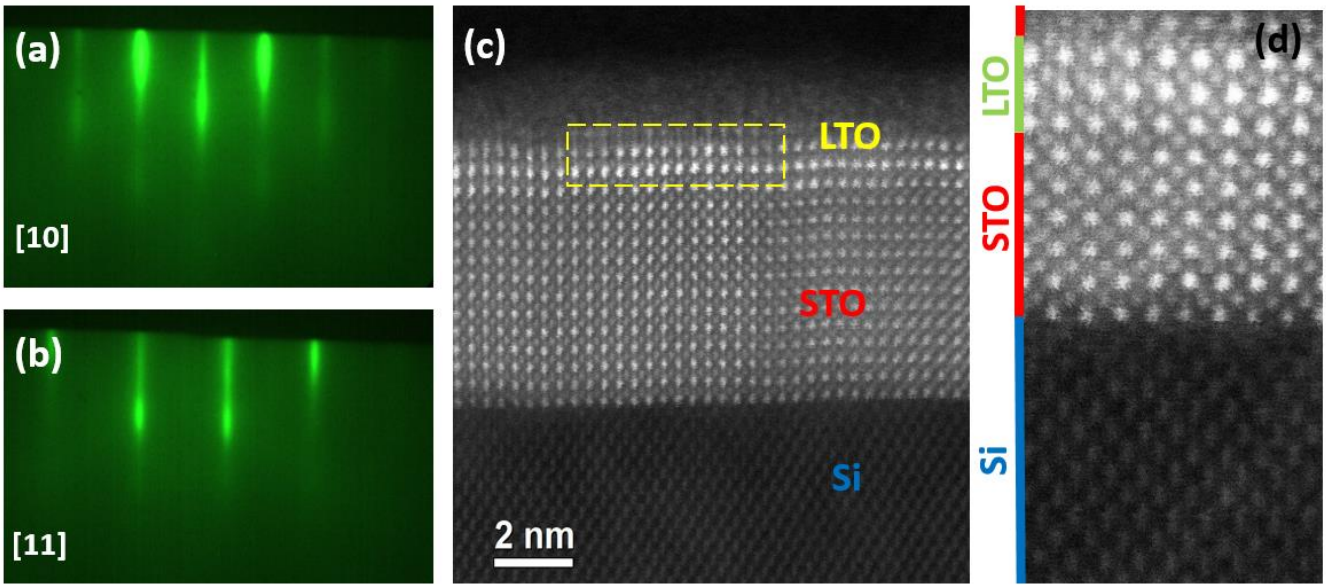

Figure 4.3: (a) and (b) RHEED images taken along [10] and [11] directions. (c) and (d) STEM image of the heterostructure confirms the atomically abrupt interface between LTO/STO and STO/Si interfaces

4.2.2 Transport Measurement Set up

In the previous section, the growth quality and the abruptness of the interfaces were confirmed using different characterization and imaging techniques, now in this section the main focus is on the electrical transport measurements of $LaTiO_3/SrTiO_3/Si$ heterostructure.

Electrical transport of the heterostructures were measured in the Van der Pauw geometry. Measuring the resistivity using Van der Pauw is a more reliable technique in which electrical contacts are made at the corner of the sample as show in Figure 4.4. Ohmic contacts were established on the four corners of 4 mm × 4 mm samples using Al wedge bonding.

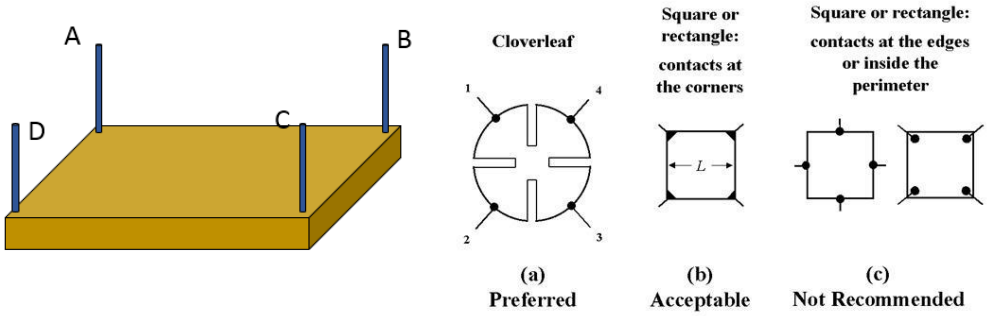

Figure 4.4: Examples of possible Van der Pauw configurations and their preference [226].

Resistivity and Hall measurements were carried out using a Keithley 2400 source-meter and a Keithley 2700 multiplexer in a Quantum Design Physical Property Measurements System (PPMS) located at University of Texas at Dallas. The PPMS configurations were kept constant throughout the measurements for all different heterostructures, meaning samples were cooled down at the constant rate ($5K^0$/min), the maximum magnetic field applied in these measurements were ~5 Tesla and the excitation current was set to ~20 μA throughout the measurements.

4.3 The Origin of Metal-Insulator Transition in $LaTiO_3/SrTiO_3/Si$ Heterostructure

According the calculated sheet carrier densities from the Hall measurement, the "n_s" values were relatively independent of the heterostructure thickness, which confirms the formation of 2DEL near the $LaTiO_3/SrTiO_3$ interface as shown in the schematic of Figure 4.1 and 4.2. The sheet carrier densities measured in our heterostructures are near ~ 2×10^{15} cm^{-2}, which is much higher than the ~ 3.5×10^{14} cm^{-2} expected strictly from charge transfer from $LaTiO_3$ to $SrTiO_3$ [192, 202, 203]. Figure 4.5 Shows the calculated sheet carrier densities plotted versus the number of unit-cells (thickness) for $LaTiO_3/SrTiO_3/Si$ heterostructures.

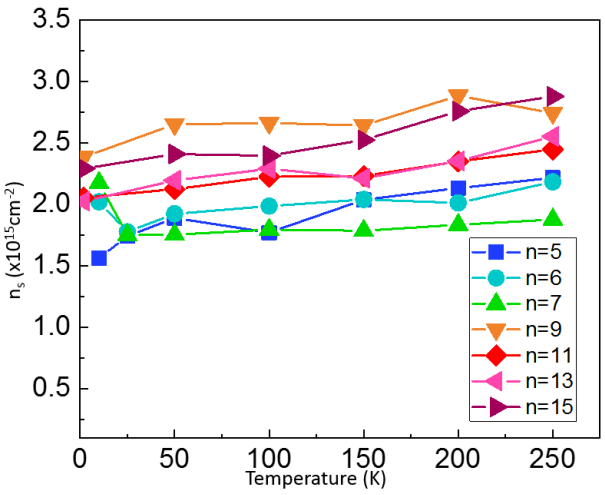

Figure 4.5 : Sheet carrier density n_s versus thickness of quantum well n.

The higher sheet carrier densities calculated from the Hall data can be originated from two main sources. All heterostructures were briefly annealed in vacuum to improve crystallinity which could potentially generate extra oxygen vacancies in the heterostructures. Additionally, lower oxygen pressure required for $LaTiO_3$ growth to avoid formation of insulating $La_2Ti_2O_7$ might be the other source of oxygen vacancies. The excess oxygen vacancies act as extra donors and thus increase the carriers at the interface [191].

It is also important to note that, since the $SrTiO_3$ layer grown on top is only 2 unit-cell thick, carriers transferred from the $LaTiO_3$ to the top are likely localized. However, the last 2 u.c of $SrTiO_3$ *and* 7nm amorphous silicon are proven to be effective in maximizing the sheet carrier density in $LaTiO_3$/ $SrTiO_3$ /*Si* heterostructures as show in Figure 4.6. In addition to their effect on increasing the sheet carrier density, thin $SrTiO_3$ layer and silicon cap reduced the surface depletion and further $LaTiO_3$ oxidation [181,204]. Hence, itinerant carriers in our heterostructures confined within a $SrTiO_3$ channel situated between $LaTiO_3$ and *Si*.

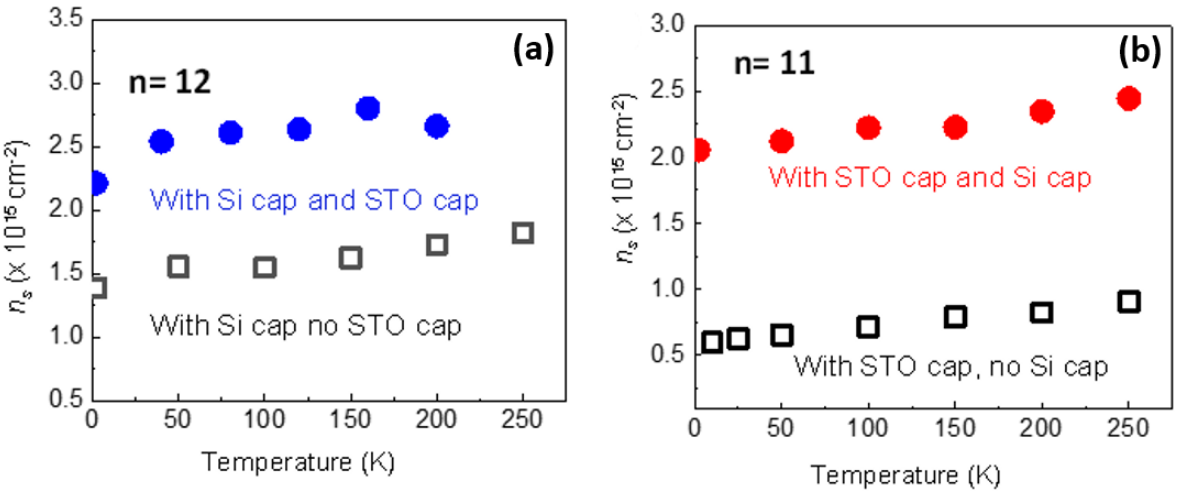

Figure 4.6: (a) Effect of 1.5 u.c. STO cap on n_s. Note that n_s is higher with the cap. (b) Effect of 7 nm amorphous Si cap on n_s.

The carrier mobilities measured on our heterostructure are also consistent with the mobility measured for rare-earth titanates heterostructures grown on comparable $SrTiO_3$ layer thickness. Figure 4.7 shows the mobility of $LaTiO_3$/$SrTiO_3$/*Si* heterostructure with different $SrTiO_3$ layer thickness over temperature range.

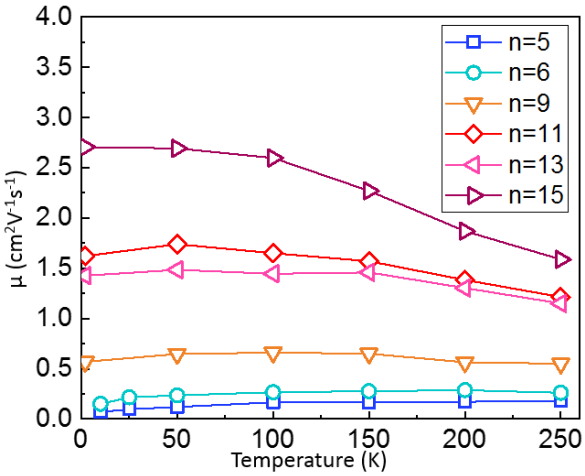

Figure 4.7: Mobility vs temperature for various LTO/STO/Si heterostructures.

Here in Figure 4.8, the sheet resistance was plotted versus temperature range for all heterostructures with different $SrTiO_3$ thickness. The metal to insulator transition observed in our heterostructures originated from $SrTiO_3$ thickness variations in which reducing (increasing) the $SrTiO_3$ layers exhibit insulating (metallic) transport behavior.

The transition occurs at $SrTiO_3$ thickness of n ~ 5, 6. The metal-insulator transition in our heterostructure is consistent with the transition driven by strong correlations, as opposed to disorder for several reasons:

1. There is a correlation between effective mass enhancement and the thickness of the heterostructures.

2. The insulating regimes are described by activated transport instead of disorder driven.

3. The activation energies are very small which is an agreement with Arrhenius activated transport.

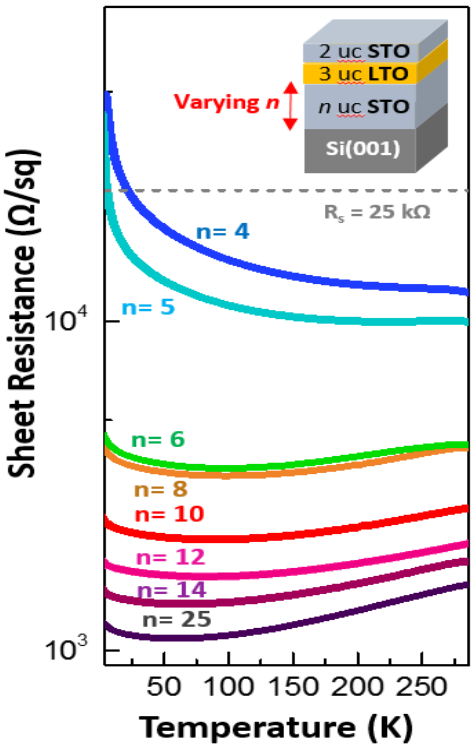

Figure 4.8: Sheet resistance versus temperature of STO/LTO/STO/Si heterostructures of various thicknesses.

The metal-insulator transition in our system happening through strong electron-electron correlation and not through disorder driven mechanisms. According to the transport data, increasing the $SrTiO_3$ layer thickness induces metallic behavior in our heterostructures which can be explained by the quadratic temperature dependence of sheet resistance known as Fermi-Liquid behavior as shown below.

$$R_s = AT^2 + R_0$$

Where R_s is the sheet resistance, A is the Fermi-Liquid T^2 dependence, R_0 is the residual resistivity and T is the temperature [205]. The quadratic temperature dependence is observed in all

of our films over a wide temperature range which is consistent with characteristics of electron-electron scattering as being the dominant transport mechanism.

Figure 4.9 shows sheet resistance as a function of T^2 for heterostructures of various $SrTiO_3$ thickness ranging from n = 6 to n = 25, sandwiched between $LaTiO_3$ and *Si* substrate. The dashed black lines in the plot are fits to the quadratic temperature dependence of our heterostructures. The temperature coefficient A was obtained from the slope of the fits to the quadratic temperature dependence The inverse correlation between the "A coefficient" and heterostructure thickness is proportional to the mass enhancement, and can be attributed to several parameters such as carrier concentrations and band-structure, which is consistent with Fermi-Liquid behavior. One of the main characteristics of enhanced electron-electron scattering in bulk rare-earth titanates is increasing the effective mass of carriers [175,180,188,189, 204].

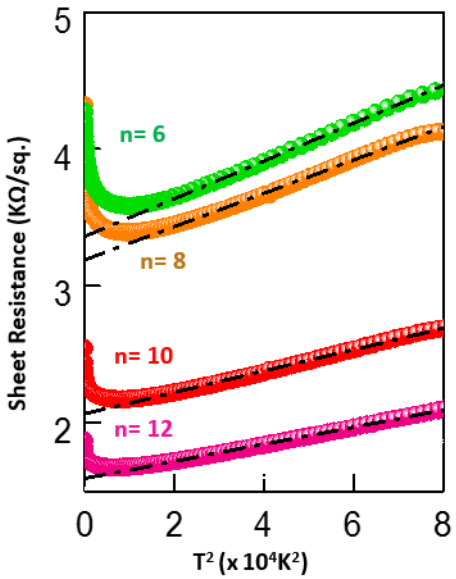

Figure 4.9: Sheet resistance plotted versus T^2 showing Fermi-liquid behavior. The black dashed lines are the fit for the quadratic temperature dependence.

Figure 4.10 shows the temperature coefficient "A" plotted versus number of unit-cells. As it can be seen from the plot, by reducing the $SrTiO_3$ channel thickness, the "A" value increases which as stated earlier is consistent with enhancement of electron effective mass.

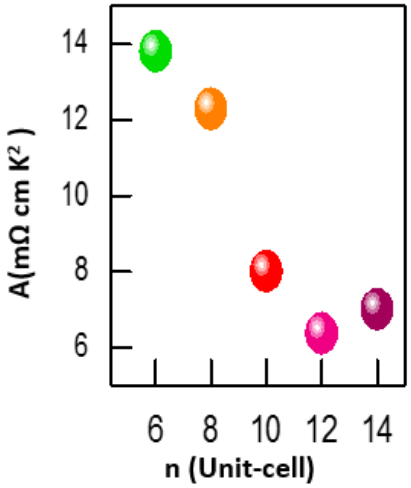

Figure 4.10: Temperature coefficient "A" as a function of thickness for metallic samples.

On the opposite side of the transition where heterostructures with n= 4 and 5 show insulating behavior ($dR_s/dT < 0$), the transport behavior can be explained by activated transport and sheet resistance can be fitted perfectly with Arrhenius transport as shown below:

$$R_s \sim exp(\Delta E/kT)$$

Rs is the sheet resistance, k is the Boltzmann constant, T is temperature and ΔE is the activation energy. Figure 4.11 shows the sheet resistance plotted versus temperature for insulating samples and fitted to the activated transport.

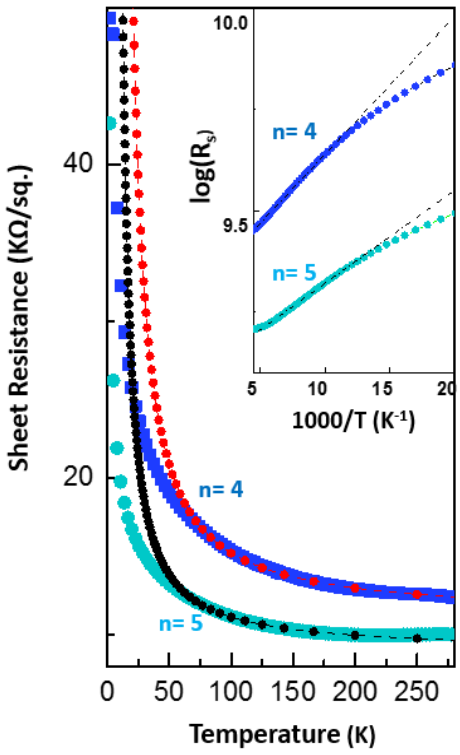

Figure 4.11: Sheet resistance of insulating heterostructures fitted to Arrhenius law. The inset shows sheet resistance plotted against 1/T for the insulating heterostructures. Black dotted lines are fits to the activated transport

It is important to note that transport behavior of the insulating regime is identical to the range found in bulk $LaTiO_3$ [188], and more importantly the dominant insulating mechanism originate from activated transport as opposed to disorder transport or variable range hopping (VRH). Transport behavior of the insulating heterostructures cannot be explained by VRH . The relationship between sheet resistance and temperature in VRH is described as :

$$R_s \sim exp[T_0/T]^y$$

Where R_s is the sheet resistance, T is the temperature and T_0 is the characteristic temperature.

The transport data in the insulating regime can be fitted with the VRH, but the extracted characteristic temperature (T_0) which represents a total sum of all possible energy states of hopping electrons in the localized area is much smaller ($36K^0$) than the reported values in the literatures (10^4-10^5) [180, 206, 227]. Therefore, VRH cannot be the dominant mechanism of the metal-insulator transitions in our heterostructures. Figure 4.12 shows the sheet resistance fitted with the VRH.

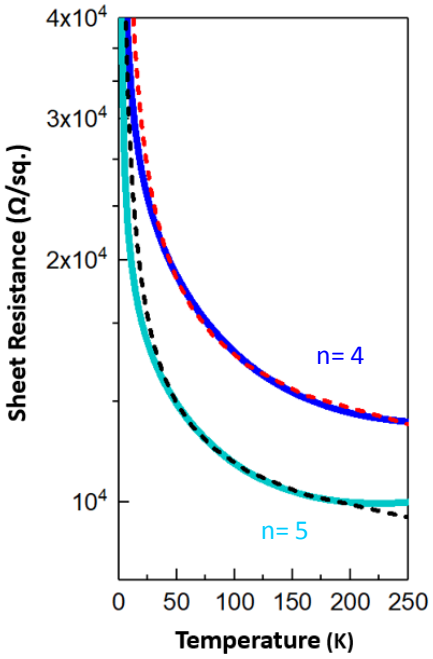

Figure 4.12: Sheet resistance of insulating heterostructures fitted to variable range hopping.

Second, the extracted activation energies E_A's are very small, around 2-3 meV which also confirms that disorder driven insulating transport is not the dominant mechanism driving the metal-insulator transition. Third, the calculated energy gap (activation energy) of more insulating samples (n=4) is higher than n = 5 which is consistent with a trend seen in enhanced correlated systems. Consequently, based on the transport behavior and data analyses performed on the

heterostructure, it has been demonstrated that the metal-insulator transition observed in our films are originated form strongly correlated effect as oppose to disorder driven mechanism.

4.4 The Effect of Strain Gradient on Metal-Insulator Transition

The structural characterizations of our $LaTiO_3$/ $SrTiO_3$ /*Si* heterostructure were done by our collaborators from North Carolina State University. Both $LaTiO_3$ and $SrTiO_3$ have the same perovskite crystal structures. The lattice constant of bulk $LaTiO_3$ (3.95 Å) is slightly larger than $SrTiO_3$ (3.91 Å) and yet larger than diamond cubic silicon (3.84 Å), consequently, the $LaTiO_3$/ $SrTiO_3$ heterostructure grown epitaxially on silicon (001) experiences compressive strain as shown schematically in Figure 4.13.

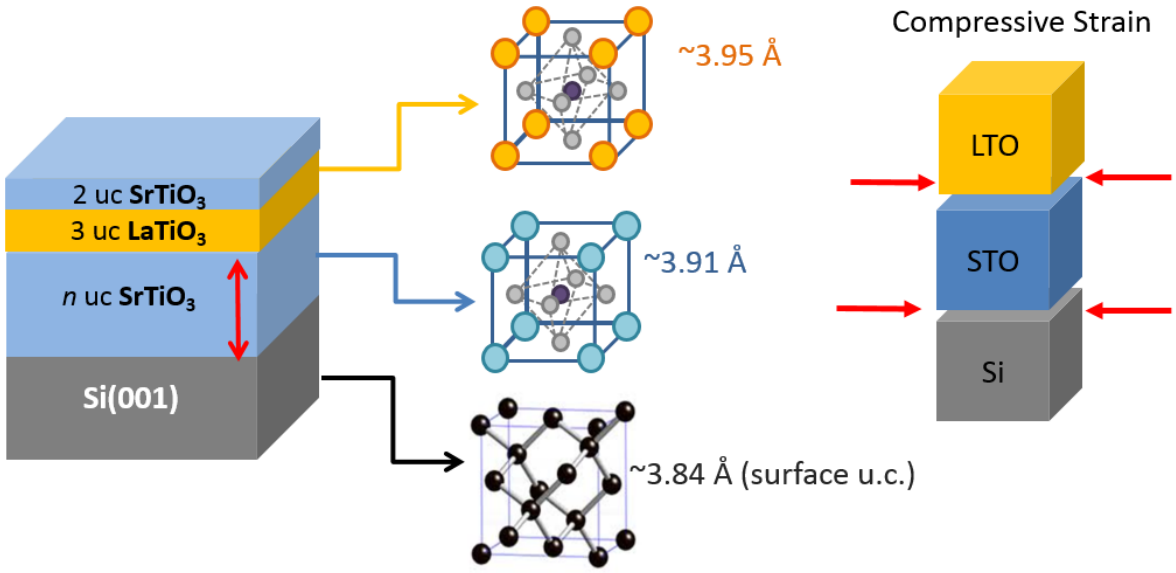

Figure 4.13: Perovskite structure of LTO/STO heterostructure grown on diamond cubic Si (001) facing compressive strain throughout the thin film.

One way of reducing the raised surface energy originated from compressive strain and lattice mismatch is the film relaxation through generating dislocations at heterostructure interfaces

[207-209] . Synchrotron X-ray diffraction and reciprocal space mapping were used to investigate the rapid relaxation of strain (strain gradient) in our system.

Synchrotron X-ray diffraction measurements were measured at the 33ID beamline at the Advanced Photon Source at room temperature. Diffraction intensities were measured using a Pilatus 100K 2D detector with an incident photon wavelength of 0.799 Angstroms. Figure 4.14 (a), shows RSM data taken from n= 5, 6, 7, and 11 samples around the off-axis reflection of Si (2, 2, L) for which there is no overlap with a Si Bragg peak. The RSMs are plotted in terms of the reciprocal lattice unit (r. l. u.) of bulk Si. Off-axis peak represents planes that are not parallel to the sample surface, therefore, they have an in-plane component (in addition to the perpendicular lattice plane spacing). Based on the data revealed by the RSM shown in Figure 4.14 (a) and (b) the interface near the $SrTiO_3$ and silicon remained largely coherent and compressively strained (labeled as C), while moving further from the interface by just a few unit-cells results in formation of partially relaxed regions (labeled as A and B).

In other words, varying the film thickness causes a decrease (increase) in the intensity of the strained (relaxed) region as indicated in the RSM data. As mentioned earlier, the lattice constants of $LaTiO_3$ and $SrTiO_3$ are larger than Si, therefore in reciprocal space, relaxation was resulted in a broadening in peak intensity and lower r.l.u values (larger real spacing). For more clarity Figure 4.15(b) shows the line profile of the heterostructure at different thicknesses which confirms the strain relaxation through three areas. As it can be clearly seen from the line profile at (2, 2, 2.7) increasing the thickness of the heterostructure were resulted in film relaxation, since the intensity of the strained portion was rapidly decreased whereas the intensity of the partially

relaxed portion was increased. The extracted in-plane and out-of-plane lattice constants of components A, B and C are compared in Table 4.1 for the n = 5, 6, 7 and 11 heterostructures.

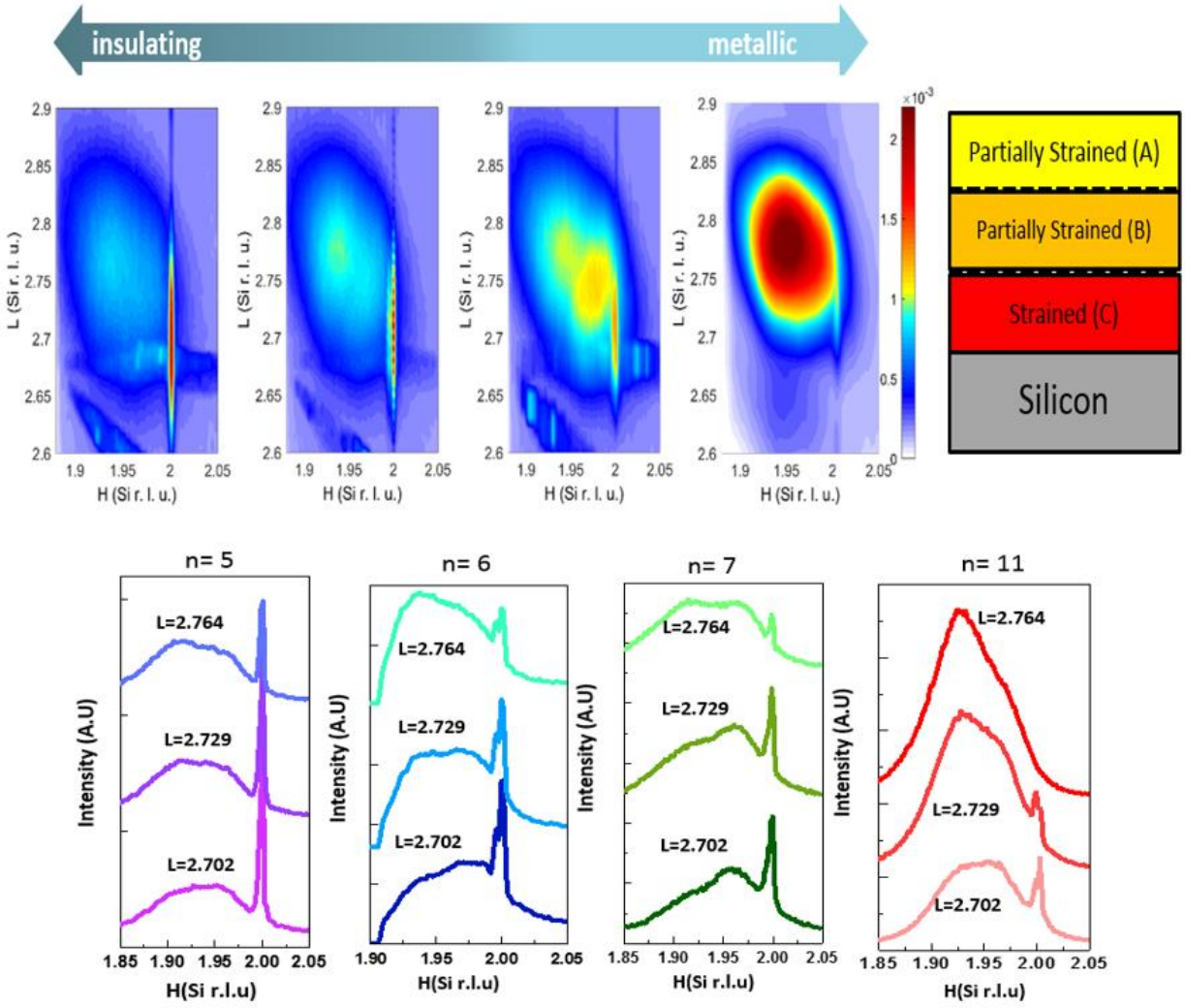

Figure 4.15: (a)Reciprocal space maps taken of heterostructure with various thickness n, showing the partially relaxed (labeled A, B) and coherently strained regions (labeled C). (b). Line profile plots of the RSM.

n	region	*c* (Å)	*a* (Å)	*c/a*
5	A	3.9284	3.9571	0.9928
	B	3.9497	3.8954	1.0139
	C	4.0334	3.8356	1.0516
6	A	3.9135	3.9526	0.9901
	B	3.9446	3.8925	1.0134
	C	4.0047	3.8300	1.0456
7	A	3.9073	3.9497	0.9893
	B	3.9560	3.8853	1.0182
	C	4.0085	3.8342	1.0455
11	A	3.9049	3.9480	0.9891
	B	3.9222	3.8924	1.0077
	C	3.9598	3.8397	1.0313

Table 4.1: Extracted lattice constants of A, B and C region C of for the n = 5, 6, 7, and 11 heterostructures.

As mentioned earlier, film relaxation can be explained through formation of dislocations to minimize the raised energy due to lattice mismatch between *Si*, $SrTiO_3$ and $LaTiO_3$. Misfit dislocations can be the source of carrier scattering which can induce disorder driven transitions. However, film relaxation (dislocations) cannot explain the metal-insulator transition observed in our heterostructures. It is important to note that thicker samples must have more dislocations to compensate for the larger misfits, whereas thinner heterostructures have fewer dislocations. Consequently, one must expect thicker heterostructures exhibit insulating behavior if the metal-

insulator transition is induced solely by a carrier scattering mechanism. In contrary, the insulating behaviors are observed in thinner heterostructures with fewer dislocations.

In order to eliminate extrinsic origins of the transition behavior seen in our heterostructures, we have also studied ultrathin 6 unit-cell solid solution $La_{0.75}Sr_{0.25}TiO_3$ film grown epitaxially on *Si* using MBE. We found that $La_{0.75}Sr_{0.25}TiO_3$ films of comparable thicknesses to the insulating samples remained metallic and the sheet carrier density calculated to be $n_s \sim 4 \times 10^{15}$ cm^{-2} as shown in Figure 4.16. The transport results confirm that insulating behavior in our heterostructures is actually originated from strongly correlated phenomena as opposed to a common effect of reducing the metallic oxide film thicknesses.

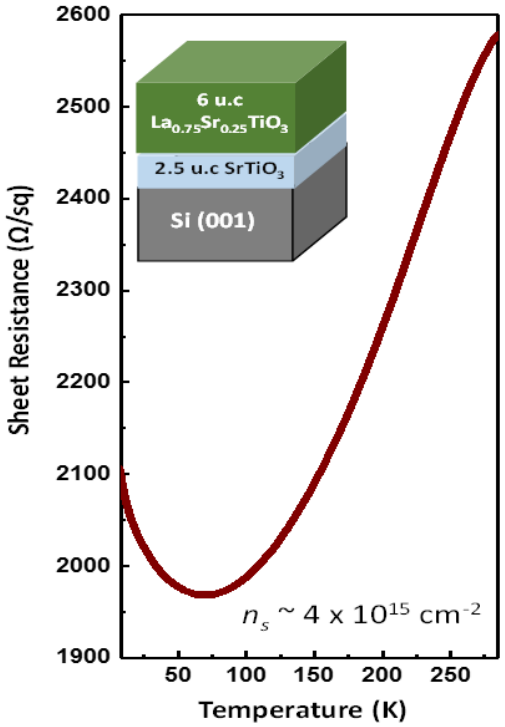

Figure 4.16: Sheet resistance of $La_{0.75}Sr_{0.25}TiO_3$ film grown epitaxially on Silicon.

4.5 Theoretical Approach and Conclusion

The metal-insulator transition in our heterostructure occurred through the filling-controlled mechanism, it is required that the three dimensional carrier density must exceed above 1.6x 10^{22} cm^{-3}, or one electron per *Ti* site. Therefore, Schrödinger-Poisson equations were applied to estimate carrier density (n_{3D}) in the $LaTiO_3/SrTiO_3/Si$ heterostructure.

According to the time independent Schrödinger equation, the existing eigenvalue consists of the kinetic part and the potential part. The carrier potential part of Schrödinger equation (V) obtained from solving the Poisson equation for voltage. In the Poisson equation (ρ) is the sum of all the possible source of carriers such as carriers in 2DEL, fixed ions and oxygen vacancies in the $SrTiO_3$. The Schrödinger equation cannot be solved by itself, since the density state of electrons change the potential value, in order to estimate n_{3D}, the carrier potential V is determined by iteratively solving the Poisson and Schrödinger equations.

$$\nabla^2 V = -\rho_f/\varepsilon \qquad \text{and} \qquad -\frac{\hbar^2}{2m}\nabla^2\psi(\mathbf{r}) + V(\mathbf{r})\psi(\mathbf{r}) = E\psi(\mathbf{r})$$

Heterostructure with n = 6 were selected for our calculations since the transition happens in the vicinity of this thickness. The 3-dimensional carrier density calculated from a Schrodinger-Poisson model shows the carrier density is equivalent to 1 electron per Ti as can be seen in Figure 4.17.

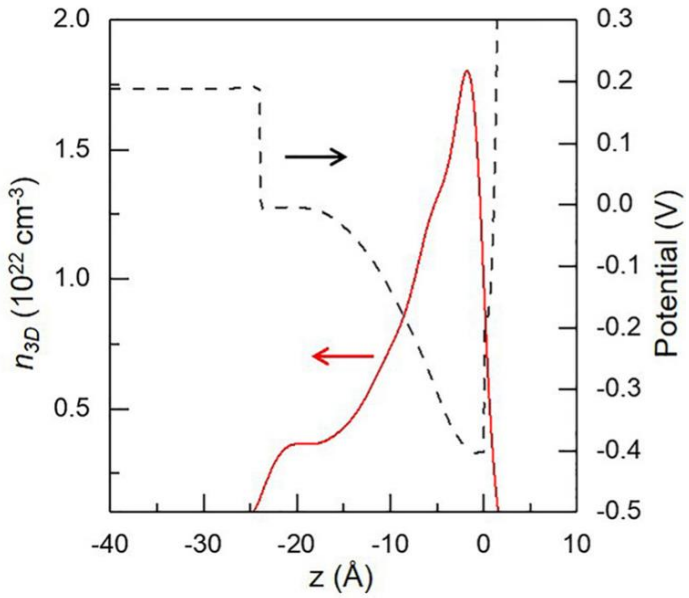

Figure 4.17: n_{3D} calculated from a Poisson-Schrodinger model showing the carrier density equivalent to 1 electron per Ti.

Earlier we discussed the effect of oxygen vacancies as a possible source of carrier density enhancement. In this regard, the strain gradient observed in the $SrTiO_3$ channel can also improve n_{3D} through an electric field E_{STO} produced by the flexoelectric effect. Flexoelectricity is a property of all insulators when subject to an inhomogeneous deformation like vertical gradient of in-plane strain induced for instance by bending or lattice mismatch strain [217]. Such deformations may cause the central cations to be squeezed up inside a unit-cell, breaking the local centro-symmetry and inducing polarity [217]. The lattice mismatch between the $SrTiO_3$ and Si layers induce strain gradients throughout the heterostructures that decay rapidly further away from the interface.

The existence of the a compressively strained region moves *Ti* cations towards positive c-direction which induces upward polarization in the $SrTiO_3$ crystals and generates an electric field. Reducing the thickness of heterostructures intensifies the polarization of the strained component of the $SrTiO_3$ as demonstrated by the *c*/*a* ratios shown in Figure 4.18.

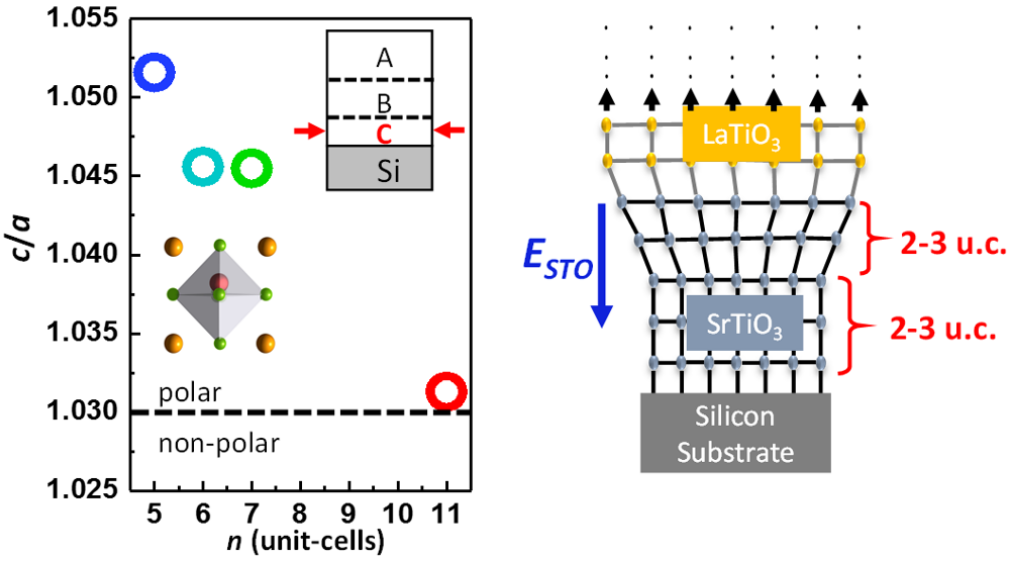

Figure 4.18: (Left) c/a ratio for the strained region. (Right) Schematic illustrating the thickness of the coherently strained STO and the number of unit-cells over which strain relaxes for the n = 5 heterostructure .

The large positive polarization at the Si/ $SrTiO_3$ interface has been previously reported in standalone epitaxial films of $SrTiO_3$ that are strained to Si (100) [221]. The negative polarization in the $LaTiO_3$, which has previously been predicted in $LaTiO_3$/ $SrTiO_3$ heterostructures, arises from charge transfer from the $LaTiO_3$ to the $SrTiO_3$, which leaves behind a positive ion core. The $LaTiO_3$ structure polarizes to screen the ion core, which screening enables carriers to extend further into the $SrTiO_3$ [222-224]. We follow the approach of D. Lee et al. [225] to estimate the electric field induced by the flexoelectric effect. E_{STO} is given as:

$$E_{STO} = \frac{e}{4\pi a \epsilon_0} \frac{\partial u}{\partial z}$$

where e is the electronic charge, ϵ_0 is the permittivity of free space, a is the lattice constant and $\partial u/\partial z$ is the gradient in strain. Given the rapid relaxation of the $SrTiO_3$ over ~ 2 – 3 u.c. as

indicated by the RSM's of Figure 4.15, we approximate $\partial u/\partial z$ as $\Delta u/\Delta z$ and estimate Δu from the fits to the RSMs. Following this approach, E_{STO} is estimated to be ~ 8 x 10^7 V/m.

In conclusion, based on the theoretical calculations such as flexoelectric effect and Schrödinger-Poisson equation along with the structural and electrical analysis like RSM, RHEED, STEM and transport data, it has been proved that the three dimensional carrier density in $LaTiO_3/SrTiO_3/Si$ heterostructure is higher than 1.6x10 ^{22} cm $^{-3}$ or one electron per each *Ti* site. Hence, the metal insulator transition (Mott transition) occur in our heterostructure can explained through filling control mechanism.

The ability of tuning metal insulator transition in strongly correlated oxide heterostructures grown directly on silicon substrate opens a pathway for various device applications such as field effect devices (MottFETs), fast response switching devices, sensor technologies and energy harvesting. The material behavior of strongly correlated oxides complements the properties of conventional semiconductors and would lead to additional modalities in device functionality.

Summary

Rare-earth titanates are known for exhibiting metal insulator transitions due to strong electron-electron correlation. The $LaTiO_3/SrTiO_3/Si$ heterostructures exhibit MI transitions in which the metallic side of the transition can be explained with Fermi-Liquid behavior and the insulating regime can be described by activated transport. The temperature coefficient is enhanced by decreasing the $SrTiO_3$ channel thickness and transport behavior of the insulating side are in perfect agreement with activated transport data fits over a large temperature range. All of the

mentioned transport behavior of the heterostructures indicate MI transition driven by a filling-control near the carrier densities of 1 electron per Ti site.

Chapter 5

Conclusion and Outlook

Oxide MBE was utilized to grow transition metal oxides with unprecedented control, layer-by-layer, at the atomic scale. By carefully changing the composition and functionality at the atomic scale, artificial heterostructures that exhibit a wide range of functionalities with novel applications can potentially be designed for future electronic devices. Improvements in the growth of artificial heterostructures have enabled many of the exotic properties of oxides such as superconductivity, high dielectrics, metal-insulator transition to be integrated on semiconductor platforms.

Over the last four chapters of this document, we have successfully achieved the main goals that were set in the beginning of the thesis. The main goals were: can we epitaxially grow three different classes of transition metal oxides on semiconductors? and will these oxides still exhibit same behaviors after integrated on semiconducting platforms?. In this regard, we have individually studied three different multi-functional oxide systems exhibiting different properties including high dielectric *SZTO*, superconducting $YBa_2Cu_3O_7$ and strongly correlated systems including $LaTiO_3$/ $SrTiO_3$ heterostructures. We have successfully demonstrated through individual projects that these multifunctional oxides can be epitaxially grown on semiconductors while they have maintained integrate their properties.

Here is the brief summary of each individual projects: In chapter two, principals of band gap engineering were applied to manipulate the band offset between single crystalline $SrZr_xTi_{1-x}O_3$ integrated directly on Ge from type-II to type-I through varying *Zr* content x.

Various structural characterization techniques such as X-ray diffraction and scanning transmission electron microscopy confirmed the single crystalline nature of the film with abrupt and coherent interface. Later Electrical characterizations such as C-V and I-V measurements confirmed the formation of type-I band offset in our heterojunctions. These findings confirm that the single crystalline *SZTO* can successfully be integrated on Ge and function as an electrical platform for device applications.

In the next chapter, the research mainly focused on creating an epitaxial platform to integrate properties of superconducting $YBa_2Cu_3O_7$ on silicon. In the first step, 30 nm single crystalline $SrTiO_3$ was successfully grown on un-doped silicon wafer. The *RHEED* images taken during the growth as well as *STEM* image confirmed the high crystallinity between $SrTiO_3$ and Si. Later 50 nm single crystalline $YBa_2Cu_3O_7$ was deposited in PLD chamber. The transition temperature for single crystalline $YBa_2Cu_3O_7$ grown on $SrTiO_3$ buffered silicon was recorded to be ~*93K*, which is the highest reported for single crystalline $YBa_2Cu_3O_7$ on silicon. Single crystalline $SrTiO_3$ grown epitaxially on silicon with MBE is proven to be a reliable platform to integrate superconducting $YBa_2Cu_3O_7$ films. The stability of 30 nm $SrTiO_3$ on silicon under ambient conditions without any protective layer makes it an ideal candidate to be used as platform for other deposition techniques like sputtering which can enable growth of $YBa_2Cu_3O_7$ on larger sized wafers.

Finally, in chapter 4, we have successfully integrated strongly correlated oxide exhibiting metal-insulator transition on to the most technologically relevant substrate. Oxide MBE was utilized to grow heterostructure consists of Mott insulator $LaTiO_3$ and band insulator $SrTiO_3$ on undoped silicon substrate. *2DEG* formed in the interface between the $SrTiO_3$ *and* $LaTiO_3$ due to charge difference between Ti^{+4} and Ti^{+3}. The transport data confirmed the metal-insulator

transition in heterostructure through changing the $SrTiO_3$ thickness layer. Thicker samples exhibiting metallic behavior that can be explained with Fermi-Liquid behavior whereas thinner sample show insulating behavior that can be described by activation transport. STEM images confirmed a formation of abrupt and coherent interface. It has been found that, reducing the thickness of the $SrTiO_3$ layer sandwiched between silicon substrate and $LaTiO_3$ layer, causing the carriers confined and induce metal-insulator transition in the heterostructure. Later, solving the Schrodinger-Poisson equation confirmed that the 3-D carrier density can reach the minimum value required for the filling control metal insulator transition (one electron-per Ti sites).

While we have addressed some of the challenges in epitaxial growth and integration of multifunctional oxides on semiconductors, a lot of problems remain to be solved in a future to fully understand the structural and electronic properties of these complex oxide systems. For instance, understanding the strongly correlated phenomena observed in many transition metal oxides remains one of the greatest challenges in solid state physics.

Based on our findings, the strongly correlated behavior (metal-insulator transition) that observed in $LaTiO_3$/ $SrTiO_3$ heterostructure can be mainly attributed to the carrier enhancement through controlling the thickness of the $SrTiO_3$ layers. Given the stacking structure of perovskite ABO_3, two independent interfaces can be defined at the $LaTiO_3$/ $SrTiO_3$ interface corresponding to the position at which the chemical make-up of the AO and BO_2 planes switch. Therefore, understanding how the interface compositions (*A-site or B-site terminated*) can affect the transport characteristics could be a new research trend. We have also shown that upward polarization in Ti atoms due to strain gradient in the heterostructure can induce electric field through flexoelectric effect that can further confine carriers near the interface.

In this regard, another approach that can improve our knowledge about these correlated systems is to realize other heterostructures comprised of different oxides with the aim to possibly control the metal-insulator transition only through strain effect which can be utilized in sensitive detectors and sensors.

In addition to understanding the fundamental physics of transition metal oxides, investigating their unique properties in device technologies can be a new pathway for experimental researchers in the field of oxide microelectronics as shown schematically in Figure 5.1. Hereof, this work has shown that *SZTO* can act as structural as well as electrical platform for integrating properties of transition metal oxides on Ge substrate, the next step is to explore a wide range of possible device applications of *SZTO*. For instance, further studies on this solid solution will be valuable to explore the possibility of using single crystalline *SZTO* as an intermediate buffer layer to minimize the charge transfer from a ferroelectric material to semiconductors.

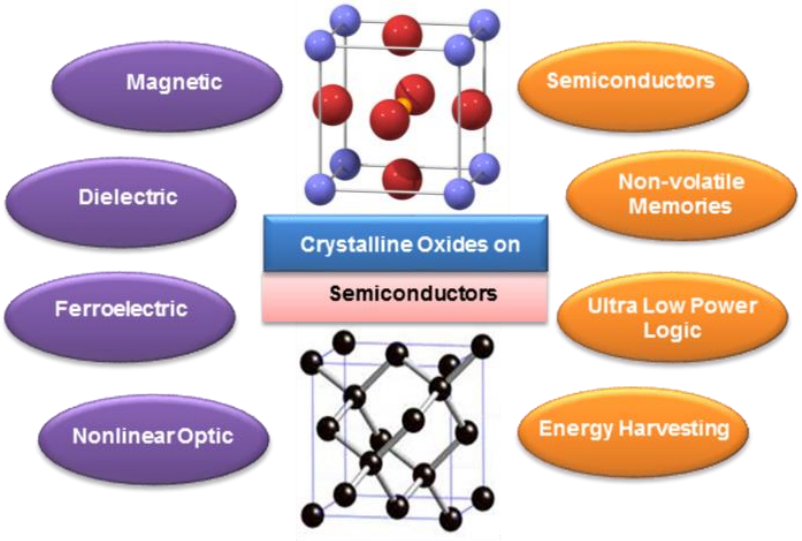

Figure 5.1: Fascinating properties of oxides. Right: possible applications.

Maximizing the conduction and valence band offsets in a type-I arrangement between the oxide and semiconductor is essential. Furthermore, minimizing the physical thickness of the oxide is also necessary. So far, we have demonstrated that solid solution $SrZr_xTi_{1-x}O_3$ (x ranging between *0.25- to 0.7*) can be utilized as a possible gate dielectric due to its type-I band offset and low leakage current. Therefore, exploiting the end member of solid solution $SrZr_xTi_{1-x}O_3$ meaning $SrZrO_3$ ($x=1$) is also important to find out the most favorable composition for the *Ge* based *PMOS*.

Finally, in order to gain further understanding of the origin of superconducting behavior in $YBa_2Cu_3O_7$ and the effect of epitaxial buffer layer on the transition temperature a variety of further experiments are necessary. To the best of my knowledge most of the buffer layers that have been used for $YBa_2Cu_3O_7$ is polycrystalline, therefore , there is a great opportunity to study a possible further improvement of transition temperature by using other transition metal oxides that can be epitaxially grown on traditional platforms as a buffer layer.

References

[1] O. Auciello, J. F. Scott, R. Ramesh, The Physics of Ferroelectric Memories, Phys. Today 51, 22 (1998).

[2] P. Muralt, Ferroelectric thin films for micro-sensors and actuators: a review, J. Micromech. Microeng. 10, 136 (2000).

[3] T. Schwarz, R. Wölbing, C. F. Reiche, B. Müller, M. J. Martínez-Pérez, T. Mühl, B. Büchner, R. Kleiner, and D. Koelle. Low-Noise $YBa_2Cu_3O_7$ Nano-SQUIDs for Performing Magnetization-Reversal Measurements on Magnetic Nanoparticles. Phys. Rev. Applied 3, 044011 (2015).

[4] S. A. Dayeh, D. P.Butler, Micromachined infrared bolometers on flexible polyimide substrates Sensors and Actuators. A. Phys. 118, 1 (2005).

[5] M. Imada, A. Fujimori and Y. Tokura. Metal-Insulator Transition, Res. Mod. Phys. 70 (1998).

[6] Z. Yang, C. Ko, S. Ramanathan, Oxide Electronics Utilizing Ultrafast Metal-Insulator Transitions, Annu. Rev. Mater. Res. 41, 337 (2011).

[7] H. T. Lue, C. Y. Liu, and T. Y. Tseng. An Improved Two-Frequency Method of Capacitance Measurement for $SrTiO_3$ as High-k Gate Dielectric. IEEE, Electron Device Letters, 23, 9, (2002).

[8] M. Yang, E. P. Gusev, M. Ieong, O. Gluschenkov, D. C. Boyd, K. Chan, P. M. Kozlowski, C. P. D'Emic, R. M. Sicina, P. C. Jamison, and A. I. Chou. Performance Dependence of CMOS on Silicon Substrate Orientation for Ultrathin Oxynitride and HfO_2 Gate Dielectrics. IEEE Electron Device Letters, 24, 5, (2003).

[9] E. P. Gusev et. al., Ultrathin Oxide Films for Advanced Gate Dielectrics Applications. Current Progress and Future Challenges, in Defects in SiO_2 and Related Dielectrics: Science and Technology, 57–579. (2000).

[10] R. M. Wallace and G. Wilk, Alternative Gate Dielectrics for Microelectronics, MRS Bull. 27, 192 (2002).

[11] T. Hori, Dielectrics and MOS ULSIs (Springer-Verlag, New York, 1997).

[12] D. G. Schlom and J. H. Haeni, Gate Oxides Beyond SiO_2, MRS Bull.27, 198 (2002).

[13] A. Demkov. B. Posadas. "Integration of multi-functional oxides with semiconductors", Springer 2014.

[14] R. A. McKee, F. J. Walker and M. F. Chisholm, Crystalline Oxides on Silicon: The First Five Monolayers, Phys. Rev. Lett. 81, 3014, (1998).

[15] X. Zhang, A.A. Demkov, H. Li, X. Hu, Y. Wei, J. Kulik, Atomic and electronic structure of the Si/SrTiO3 interfac, Phys. Rev. B 68 , 125323 (2003).

[16] C.R. Ashman, C.J. Först, K. Schwarz, P.E. Blöchl, First-principles calculations of strontium on Si(001), Phys. Rev. B 69 , 075309 (2004).

[17] C.R. Ashman, C.J. Först, K. Schwarz, P.E. Blöchl, First-principles calculations of strontium on Si(001), Phys. Rev. B 69 , 075309 (2004).

[18] Y. Liang, S. Gan, Y. Wei, R. Gregory, Effect of Sr adsorption on stability of and epitaxial $SrTiO_3$ growth on Si(001) surface, Phys. Status Solidi B 243 , 2098 (2006).

[19] C. Rossel, B. Mereu, C. Marchiori, D. Caimi, M. Sousa, A. Guiller, H. Siegwart, R. Germann, J.-P. Locquet, J. Fompeyrine, D.J. Webb, C. Dieker, J.W. Seo, Field-effect transistors with $SrHfO_3$ as gate oxide, Appl. Phys. Lett. 89 , 053506 (2006).

[20] J. W. Reiner, A. Posadas, M. Wang, F.J. Walker, C.H. Ahn, Electrical properties and interfacial structure of epitaxial $LaAlO_3$ on Si (001), J. Appl. Phys. 105, 124501 (2009).

[21] A. Vasudevarao, Y.L. Li, A. Kochhar, H. Ma, J. Levy, P. Zschack, J.C. Woicik, L.Q. Chen, V. Gopalan, D.G. Schlom, c-axis oriented epitaxial $BaTiO_3$ films on (001) Si, J. Appl. Phys. 100 , 024108 (2006).

[22] G. Niu, S. Yin, G. Saint-Girons, B. Gautier, P. Lecoeur, V. Pillard, G. Hollinger, B. Vilquin, Epitaxy of $BaTiO_3$ thin film on Si(0 0 1) using a $SrTiO_3$ buffer layer for non-volatile memory application, Microelectron. Eng. 88 , 1232 (2011).

[23] A.K. Pradhan, J.B. Dadson, D. Hunter, K. Zhang, S. Mohanty, E.M. Jackson, B. Lasley-Hunter, K. Lord, T.M. Williams, R.R. Rakhimov, J. Zhang, D.J. Sellmyer, K. Inaba, T. Hasegawa, S. Mathews, B. Joseph, B.R. Sekhar, U.N. Roy, Y. Cui, A. Burger, Ferromagnetic properties of epitaxial manganite films on $SrTiO_3$/Si heterostructures, J. Appl. Phys. 100 , 033903 (2006).

[24] J. Wang, H. Zheng, Z. Ma, S. Prasertchoung, M. Wuttig, R. Droopad, J. Yu, K. Eisenbeiser, R. Ramesh, Epitaxial $BiFeO_3BiFeO_3$ thin films on Si, Appl. Phys. Lett. 85 , 2574 (2004).

[25]. A. Posadas, M. Berg, H. Seo, A. de Lozanne, A.A. Demkov, D.J. Smith, A.P. Kirk, D. Zhernokletov, R.M. Wallace, Epitaxial integration of ferromagnetic correlated oxide $LaCoO_3LaCoO_3$ with Si (100), Appl. Phys. Lett. 98 , 053104 (2011).

[26] A. Posadas, M. Berg, H. Seo, D.J. Smith, A.P. Kirk, D. Zhernokletov, R.M. Wallace, A. de Lozanne, A. Demkov., Strain-induced ferromagnetism in $LaCoO_3$: Theory and growth on Si (1 0 0), Microelectron. Eng. 88 , 1444 (2011).

[27] H. Seo, A.B. Posadas, C. Mitra, A.V. Kvit, J. Ramdani, A. Demkov, Band alignment and electronic structure of the anatase TiO_2/$SrTiO_3$heterostructure integrated on Si(001), Phys. Rev. B 86 , 075301 (2012).

[28] M.D. McDaniel, A. Posadas, T. Wang, A. Demkov, J. Ekerdt, Growth and characterization of epitaxial anatase TiO_2 on $SrTiO_3$-buffered Si(001) using atomic layer deposition, Thin Solid Films 520 , 6525 (2012).

[29] B.W. Wessels, Ferroelectric oxide epitaxial thin films: synthesis and non-linear optical properties, J. Cryst. Growth 195 , 706 (1998).

[30] A. Podlesnyak, S. Streule, J. Mesot, M. Medarde, E. Pomjakushina, K. Conder, A. Tanaka, M.W. Haverkort, D.I. Khomskii, Spin-State Transition in $LaCoO_3$: Direct Neutron Spectroscopic Evidence of Excited Magnetic States, Phys. Rev. Lett. 97 , 247208 (2006).

[31] P.M. Raccah, J.B. Goodenough, First-Order Localized-Electron ⇆ Collective-Electron Transition in $LaCoO_3$, Phys. Rev. 155 , 932 (1967).

[32] D.L. Polla, L.F. Francis, processing and characterization of piezoelectric materials and integration intomicro electromechanical systems, Annu. Rev. Meter. Sci. 28, 563 (1998).

[33] X. Chen, S. Schen, L. Guo, S. Mao, Semiconductor-based Photocatalytic Hydrogen Generation, Chem. Rev. 110, 6503 (2010).

[34] P.Y. Yu, M. Cardona, Fundamentals of Semiconductors: Physics and Materials Properties , 4th edn. (Springer, Berlin, 2010).

[35] J.C. Slater, The Ferromagnetism of Nickel. II. Temperature Effects, Phys. Rev. 49 , 931 (1936).

[36] Goldschmidt, Geochemistry, Oxford University press, 1958.

[37] L. G. Tejuca, J. L. G. Fierro, Properties and Applications of Perovskite-type Oxides, Edited by CRC Press, (1992).

[38] Nevill F. Mott, H. Jones, The Theory of the Properties of Metals and Alloys, Cambridge publication (press)1958.

[39] E. Pavarini, S. Biermann, A. Poteryaev, A. I. Lichtenstein, A. Georges, and O. K. Andersen, Mott Transition and Suppression of Orbital Fluctuations in Orthorhombic $3d^1$ Perovskites, Phys. Rev. Lett. 92, 176403, (2004).

[40] P. A. Cox., The electronic structure and chemistry of solids, Oxford University Press (1987).

[41] Kittel. C., Introduction to solid state physics, Wiley New York (1976).

[42] R.G. Burns, Applications of crystal field theory, Cambridge University Press (1973).

[43] Vladimir I. Anisimov, Jan Zaanen, and Ole K. Andersen, Band theory and Mott insulators: Hubbard U instead of Stoner I, Phys. Rev. Lett. 8, 44,(1999).

[44] H. Fehske, A. P. Kampf, M. Sekania, G. Wellein, Nature of the Peierls- to Mott-insulator transition in 1D, arXiv:cond-mat/0203616 [cond-mat.str-el] (2017).

[45] Altunbulak, M. and Klyachko, The Pauli Principle Revisited , A. Commun. Math. Phys. (2008).

[46] S. Piskunov, E. Heifets, R.I. Eglitis, G. Borstel, Bulk properties and electronic structure of $SrTiO_3$, $BaTiO_3$, $PbTiO_3$ perovskites, Computational Materials Science 29, 165–178, (2004).

[47] G. Cappelini, S. Bouette-Russo, B. Amadon, C. Noguera, F. Finocchi, Structural properties and quasiparticle energies of cubic SrO, MgO and $SrTiO_3$, J. Phys.: Condens. Matter 12, 3671, (2000).

[48] N. H. HILL, Density Functional Studies of Multiferroic Magnetoelectrics, Annu. Rev. Mater. Sci., 32, 1-37 (2002).

[49] M. J. Akhtar, Z. Akhtar, and R. A. Jakson, Computer Simulation Studies of Strontium Titanate, J.Am. Ceram. Soc., 78, 421-28 (1995).

[50] T. Kolodiazhnyi, A. Petric, The Applicability of Sr-deficient n-type $SrTiO_3$ for SOFC Anodes, J. of Electroceramics, 15, 5-11, (2005).

[51] L. E. Rehn, Ion beam microanalysis, Nucl. Instrum. and Methods, B64, 161 (1992).

[52] P. Ramirez, et al., Colossal magnetoresistance, J. Phys.: Condens. Matter 9, 8171-8199 (1997).

[53] W. D. Luo, W. H. Duan, S. G. Louie and M. L. Cohen, Structural and electronic properties of n-doped and p-doped $SrTiO_3$, Phys. Rev. B 70, 214109, (2004).

[54] Y. S. Dai, H. B. Lu, F. Chen, Z. H Chen, Z. Y. Ren and D. H. L. Ng, In-doped $SrTiO_3$ ceramic thin films, Appl. Phys. Lett. 80, 3545, (2002).

[55] W. D. Luo, W. H. Duan, S. G. Louie and M. L. Cohen, Structural and electronic properties of n-doped and p-doped $SrTiO_3$, Phys. Rev. B 70, 214109, (2004).

[56] Y. S. Dai, H. B. Lu, F. Chen, Z. H Chen, Z. Y. Ren and D. H. L. Ng, In-doped $SrTiO_3$ ceramic thin films, Appl. Phys. Lett. 80, 3545, (2002)

[57] Y. S. Dai, H. B. Lu, F. Chen, Z. H Chen, Z. Y. Ren and D. H. L. Ng, In-doped $SrTiO_3$ ceramic thin films, Appl. Phys. Lett. 80, 3545, (2002).

[58] S. Gariglio, J. W. Seo, J. Fompeyrine, J.-P. Locquet, and J.-M. Triscone, Transport properties in doped Mott insulator epitaxial $LaTiO_3$ thin films, Phys. Rev. B 63, 161103(R), (2001).

[59] M. I. Aroyo, A. Kirov, C. Capillas, J. M. Perez-Mato, and H. Wondratschek, Bilbao Crystallographic Server. II. Representations of crystallographic point groups and space groups, Acta Crystallogr., Sect. A: Found. Crystallogr. 62, 115 (2006).

[60] N.F. Mott, R. Pierls. Discussion of the paper by de Boer and Verway. Proceedings of the physical society of London 49, 72, (1937).

[61] B. Maple. High temperature superconductivity. MRS Bulletin XV, 6, 60, (1990).

[62] D. Harlingen. Phase sensitive test of symmetry in the high temperature superconductor. Reviews of modern physics 67,515, (1995).

[63] J.C. Slater, The Ferromagnetism of Nickel. II. Temperature Effects, Phys. Rev. 49 , 931 (1936).

[64] Goldschmidt, Geochemistry, Oxford University press, 1958.

[65] L. G. Tejuca, J. L. G. Fierro, Properties and Applications of Perovskite-type Oxides, Edited by CRC Press, (1992).

[66] Joshua Young, and James M. Rondinelli, Octahedral Rotation Preferences in Perovskite, J. Phys. Chem. Lett. 7, 918−922, (2016).

[67] A. A. Stekolnikov, J. Furthmüller, and F. Bechstedt, Absolute surface energies of group-IV semiconductors: Dependence on orientation and reconstruction, Phys. Rev. B 65, 115318, (2002).

[68] G. Koller, Michael G Ramsey, Growth and Electronic Structure of Homo- and Hetero-epitaxial Nanostructures, 71923-6_7, Springer, Berlin, Heidelberg.

[69] Hosung Seo, Agham B. Posadas, Chandrima Mitra,1 Alexander V. Kvit, Jamal Ramdani, and Alexander A. Demkov1, Band alignment and electronic structure of the anatase TiO_2/$SrTiO_3$(001) heterostructure integrated on Si(001), Phys. Rev. B 86, 075301 (2012).

[70] Seung-Hyub Baek, Chang-Beom Eom, Epitaxial integration of perovskite-based multifunctional oxides on silicon, Acta Materialia 61 2734–2750, (2013).

[71] Y. Liang, Y. Wei, X. M. Hu, Z. Yu, R. Droopad, H. Li, and K. Moore, Heteroepitaxy of $SrTiO_3$ on vicinal Si(001): Growth and kinetic effects, J. Appl. Phys. 96, 3413 (2004).

[72] S.J. Wang, C.K. Ong, L.P. You, S.Y. Xu, Epitaxial growth of yttria-stabilized zirconia oxide thin film on natively oxidized silicon wafer without an amorphous layer. Semicond. Sci. Tech. 15 , 836 (2000).

[73] J. G. Bednorz, K. Miiller, perovskite-type oxides - the new approach to high-T_c superconductivity, Phys. B 64,89-96, (1986).

[74] M. Ohring, " The Materials Science of thin Films" , Academic Press (1992).

[75] D. W Pashley, The study of epitaxy in thin surface films, Adv. Phys., 5, 173, (1956).

[76] Ferenc Riesz, Rotated tilting in lattice-mismatched heteroepitaxial systems, J. Crys. Growth, 140, 213-218, (1992).

[77] S.J. Wang et al., Crystalline zirconia oxide on silicon as alternative gate dielectrics. Appl. Phys. Lett. 78 , 1604 (2001).

[78] High-quality silicon/insulator heteroepitaxial structures formed by molecular beam epitaxy using Al_2O_3 and Si. J. Cryst. Growth 196 , 88 (1999).

[79] H. Li et al., Two-dimensional growth of high-quality strontium titanate thin films on Si. J. Appl. Phys. 93 , 4521 (2003).

[80] C. Rossel et al., $SrHfO_3$ as gate dielectric for future CMOS technology. Microelectron. Eng. 84 , 1869 (2007).

[81] T.F. Wietler et al., Epitaxial growth of Gd_2O_3 on Ge films grown by surfactant-mediated epitaxy on Si(001) substrates. Solid State Electron. 53 , 833 (2009).

[82] M.E. Hunter, M.J. Reed, N.A. El-Masry, J.C. Roberts, S.M. Bedair, Epitaxial Y_2O_3 films grown on Si(111) by pulsed-laser ablation. Appl. Phys. Lett. 76 , 1935 (2000).

[83] K.G. Gunther, Evaporated layers of semiconducting III–V compounds, Naturwissenschaften 45, 415, (1958).

[84] Peng, L.M., Dudarev, S.L. & Whelan, M.J., High-Energy Electron Diffraction and Microscopy (Oxford University Press, Oxford, 2004).

[85] Harris, J.J., Joyce, B.A. & Dobson, P.J., Oscillations in the surface structure of Sn-doped GaAs during growth by MBE, Surf. Sci. 103, L90 (1981).

[86] Darrell G. Schlom, Perspective: Oxide molecular-beam epitaxy, APL MATERIALS 3, 062403 (2015).

[87] D. Buchanan, Scaling the gate dielectric materials, IBM J. Res. Develop. 43,245, (1999).

[88] M.L. Green, E.P. Gusev, R. Degraeve, E. Garfunkel, Ultrathin (<4 nm) SiO_2 and Si–O–N gate dielectric layers for silicon microelectronics: Understanding the processing, structure, and physical and electrical limits, J. Appl. Phys. (Review) 90 (2001), in press.

[89] E.P. Gusev, Ultrathin oxide films for advanced gate dielectrics applications: recent progress and future challenges in SiO_2 and Related Dielectrics, Science and Technology, Kluwer, Dordrecht, 2. 557, (2000).

[90] E.P. Guseva ,E. Cartiera, D.A. Buchanana, M. Gribelyukb, M. Copela, H. Okorn-Schmidt , C. D'Emic, : Ultrathin high-K metal oxides on silicon: processing, characterization and integration issues. Microelectronic Engineering 59, 341–349, (2001).

[91] P. K. Roy and I. C. Kizilyalli, Stacked high-ε gate dielectric for gigascale integration of metal–oxide–semiconductor technologies, Appl. Phys. Lett. 72, 2835 (1998).

[92] E.P. Gusev, M. Copel, E. Cartier, D.A. Buchanan, H. Okorn-Schmidt, M. Gribelyuk, D. Falcon, R. Murphy, S. Molis, I.J.R. Baumvol, C. Krug, M. Jussila, M. Tuominen, S. Haukka, Physical characterization of ultrathin films of high dielectric constant materials on silicon. The Electrochemical Soc, Pennington, NJ, 477, (2000).

[93] T.S. Jeon, J.M. White, D.L. Kwong, Thermal stability of ultrathin ZrO_2 films prepared by chemical vapor deposition on Si(100), Appl. Phys. Lett. 78, 368, (2001).

[94] W.-J. Qi, R. Nieh, B.H. Lee, L. Kang, Y. Jeon, J.C. Lee, Electrical and reliability characteristics of ZrO_2 deposited directly on Si for gate dielectric application, Appl. Phys. Lett. 77, 3269, (2000).

[95] L. Kang, K. Onishi, Y. Jeon, B.H. Lee, C. Kang, W.-J. Qi, R. Nieh, S. Gopalan, R. Choi, J.C. Lee, Effect of barrier layer on electrical properties on gate dielectrics, IEDM Technical Digest, 181, (2000).

[96] S.A. Campbell, H.S. Kim, D.C. Gilmer, B. He, T. Ma, W.L. Gladfelter, Electrical and material characterizations of high-permittivity mterials, IBM J. Res. Develop. 43, 383, (1999).

[97] C. Chaneliere, J.L. Autran, R.A.B. Devine, B. Balland, the physical chemistry of Si-SiO_2, Mat. Sci. Eng. Reports R22, 269, (1998).

[98] G.B. Alers, D.J.Werder, Y. Chabal, H.C. Lu, E.P. Gusev, E. Garfunkel, T. Gustafsson, R. Urdahl, Intermixing at the tantalum oxide/silicon interface in gate dielectric structures, Appl. Phys. Lett. 73, 1517, (1998).

[99] M. Houssa, M. Naili, M.M. Heyns, A. Stesmans, Ultrathin high-K metal oxides on silicon: processing, characterization and integration issues, J. Appl. Phys. 89, 792, (2001).

[100] J. W. Reiner, A. M. Kolpik, Y. Segal, K. F. Garrity, S. Ismail-Beige, C. H. Han, and F.J. Walker, Crystalline Oxides on Silicon, Adv. Mat., 22, 2919, (2010).

[101] V. Santhinatha, J. Altieri, W. Tian, A. Sharan, A. Vasudeva Rao, Y. L. Li, A. Kocher, H. Ma, J. Levy, P. Schack, J. C. Wojcik, L. Q. Chen, V. Gopalan, and D. G. Scholz, c-axis oriented epitaxial $BaTiO_3$films on (001) Si, J. Appl. Phys. 100, 024108, (2006).

[102] A. Posadas, M. Berg, H. Seo, A. de Lozanne, A.A. Demkov, D.J. Smith, A.P. Kirk, D. Zhernokletov and R.M. Wallace, Epitaxial integration of ferromagnetic correlated oxide $LaCoO_3$ with Si (100), Appl. Phys. Lett. 98, 053104, (2011).

[103] J. H. Ngai, D. P. Kumah, C. H. Ahn, and F. J. Walker, Hysteretic electrical transport in $BaTiO_3/Ba_{1-x}Sr_xTiO_3$/Ge heterostructures, Appl. Phys. Lett. 104, 062905, (2014).

[104] Federico Capasso, Band-Gap Engineering: From Physics and Materials to New Semiconductor Devices. SCIENCE, 235, (1985).

[105] M. Landmann, E. Rauls, and W. G. Schmidt, Understanding band alignments in semiconductor heterostructures: Composition dependence and type-I–type-II transition of natural band offsets in nonpolar zinc-blende $Al_xGa_{1-x}N/Al_yGa_{1-y}N$ composites, Phys. Rev. B 95, 155310, (2017).

[106] Guofu Niu , Band Alignment and Graded Heterostructures, Auburn University (2007).

[107] J.Robertson , New High-K Materials for CMOS Applications, Comprehensive Semiconductor Science and Technology, 4, 132-176, (2011).

[108] Y. Liang, J. Curless, and D. McCready, Band alignment at epitaxial $SrTiO_3$ –GaAs heterojunction, Appl. Phys. Lett. 86, 082905 (2005).

[109] S.A. Chambers, Y. Liang, Z. Yu, R. Droopad, and J. Ramdani and K. Eisenbeiser, Band discontinuities at epitaxial $SrTiO_3$/Si(001) heterojunctions, Appl. Phys. Lett. 77, 1662, (2000).

[110] F. Amy, A. S. Wan, A. Kahn, F. J. Walker, and R. A. McKee, Band offsets at heterojunctions between $SrTiO_3$ and $BaTiO_3$and Si(100), J. Appl. Phys., 96, 1635, (2004).

[111] Y. Liang, J. Curless, and D. McCready, Band alignment at epitaxial $SrTiO_3$–GaAs(001)) heterojunction, Appl. Phys. Lett., 86, 082905, (2005).

[112] F. Capasso, Band-Gap Engineering: From Physics and Materials to New Semiconductor Devices, Science., 235, 172, (1987).

[113] R. Schafranek, J. D. Baniecki, M. Ishii, Y. Kotaka, K. Yamananka and K. Kurihara, J. Phys. D: Band offsets at the epitaxial $SrTiO_3/SrZrO_3$ heterojunction, Appl. Phys., 45, 055303, (2012).

[114] C. Blumenstein, S. Meyer, A. Ruff, B. Schmid, J. Schafer, and R. Claessen, High purity chemical etching and thermal passivation process for Ge(001) as nanostructure template, J. Chem. Phys. 135, 064201 (2011).

[115] L. Chu, Y. C. Liu, W. C. Lee, T. D. Lin, M. L. Huang, T. W. Pi, J. Kwo, and M. Hong, Greatly improved interfacial passivation of in-situ high κ dielectric deposition on freshly grown molecule beam epitaxy Ge epitaxial layer on Ge(100), Appl. Phys. Lett. 104, 202102 (2014).

[116] M. Klesse, G. Scappucci, G. Capellini, and M. Y. Simmons, Preparation of the Ge(001) surface towards fabrication of atomic-scale germanium devices, Nanotechnology 22, 145604 (2011).

[117] N. Sata, M. Ishigame and S. Shin, Solid State Ionics, 8688, 629, (1996).

[118] C. Lu, A. W. Czanderna, ed. Applications of Piezoelectric Quartz Crystal Microbalances. Amsterdam: Elsevier (1984).

[119] B. D. Cullity, Elements of X-ray diffraction, Springer (1956).

[120] I.C. Noyan and J.B. Cohen, Residual Stress-Measurement by Diffraction, Interpretation, Springer-Verlag, New York, 1987.

[121] Williams D.B., Carter C.B. The Transmission Electron Microscope. In: Transmission Electron Microscopy. Springer, Boston, MA, (1996).

[122] Christian Kübel, Andreas Voigt, Remco Schoenmakers, Max Otten, David Su, Tan-Chen Lee, Anna Carlsson and John Bradley, Recent Advances in Electron Tomography: TEM and HAADF-STEM Tomography for Materials Science and Semiconductor Applications, Microscopy and Microanalysis, 11, 378-400, (2005).

[123] F Hofer et al., Fundamentals of electron energy-loss spectroscopy, IOP Conf. Ser.: Mater. Sci. Eng. 109, 01, (2007).

[124] Hu et. al. MOS Capacitor, Barkley Publications (2009).

[125] B. Streetman, S. Banerjee. Solid State Electronic Devices. Pearson Publications NJ 07458.

[126] T.S. Jeon, J.M. White, D.L. Kwong, Thermal stability of ultrathin ZrO_2 films prepared by chemical vapor deposition on Si(100), Appl. Phys. Lett. 78, 368, (2001).

[127] W.-J. Qi, R. Nieh, B.H. Lee, L. Kang, Y. Jeon, J.C. Lee, Electrical and reliability characteristics of ZrO_2 deposited directly on Si for gate dielectric application, Appl. Phys. Lett. 77, 3269, (2000).

[128] G. J. Norga, C. Marchiori, C. Rossel, A. Guiller, J. P. Locquet, H. Siegwart, D. Caimi, J. Fompeyrine, J. W. Seo, and Ch. Dieker. The relationship between oxygen stoichiometry and interface stability. Journal of Applied Physics 99, 084102 (2006).

[129] S. Jeon, F. J. Walker, C. A. Billman, R. A. McKee and H. Hwang, Electrical characteristics of epitaxially grown $SrTiO_3$ on silicon for metal-insulator-semiconductor gate dielectric applications, IEEE Elec. Dev. Lett., 24, 218, (2003).

[130] K.Eisenbeiser, J. M. Finder, Z. Yu, J. Ramdani, J. A. Curless, J. A. Hallmark, R. Droopad, W. J. Ooms, L. Salem, S. Bradshaw and C. D. Overgaard, Field effect transistors with $SrTiO_3$ gate dielectric on Si, Appl. Phys. Lett. 76, 1324, (2000).

[131] R. A. McKee, F.J. Walker, and M.F. Chisholm, Physical Structure and Inversion Charge at a Semiconductor Interface with a Crystalline Oxide, Science., 293, 468, (2001).

[132] N. Sata, M. Ishigame and S. Shin, Solid State Ionics, 8688, 629, (1996).

[133] G. Mavrou, P. Tsipas, A. Sotiropoulos, S. Galata, Y. Panayiotatos, A. Dimoulas, C. MarchioriandJ.Fompeyrine,Veryhigh-κ$ZrO_2$with La_2O_3 passivating interfacial layers on germanium substrates, Appl. Phys. Lett., 93, 212904, (2008).

[135] E. A. Kraut, R. W. Grant, J. W. Waldrop and S. P. Kowalczyk, Precise Determination of the Valence-Band Edge in X-Ray Photoemission Spectra: Application to Measurement of Semiconductor Interface Potentials, Phys. Rev. Lett., 44, 1620, (1980).

[136] E. A. Kraut, R. W. Grant, J. W. Waldrop and S. P. Kowalczyk, Semiconductor core-level to valence-band maximum binding-energy differences: Precise determination by x-ray photoelectron spectroscopy, Phys. Rev. B, 28, 1965, (1983).

[137] W.H. Butler, X.-G. Zhang, T.C. Schulthess and J.M. MacLaren, Spin-dependent tunneling conductance of Fe|MgO|Fe , Phys. Rev., B 63, 054416, (2001).

[138] C. Marchiori, M. Sousa, A. Guiller, H. Siegwart, J.-P. Locquet, J. Fompeyrine, G. J. Norga and J. W. Seo, Two-photon-induced reduction of metal ions for fabricating three-dimensional electrically conductive metallic microstructure, Appl. Phys. Lett., 88, 07291, (2006).

[139] P. A. Lee, N. Nagaosa and X. G. Wen, "Opportunities in nanomagnetisim," Rev. Mod. Phys., 78, 17, (2006).

[140] O. Harneck, B. Karasik, W. McGrath, A. Kleinsasser and J. Barner, "Micro bridge made from $YBa_2Cu_3O_7$ thin films," Supercond. Sci. Technol., 12, 850, (1999).

[141] J. C. Brasunas and B. Lakew, "High T_c superconductors bolometer with record performance," Appl. Phys. Lett., 64 (1994) 777.

[142] J. P. Rice, E. N. Grossman and D. A. Rudman, "Antenna-coupled high-T_c air-bridge microbolometer on Silicon," Appl. Phys. Lett., 65, 773, (1994).

[143] P. C. Shan, Z. Celik-Butler, D. P. Butler, A. Jahanzeb, C. M. Travers, W. Kula and R. Sobolewski, "Semiconducting $YBa_2Cu_3O_7$ thin film for uncooled infrared bolometers," Appl. Phys. Lett., 78, 6658, (1995).

[144] L. M. Wang, S. M. Chiou, M. L. Chu, C. W. Wu, M. C. Chang, C. G. Hsu, D. S. Hsieh and J. H. Chen, "Cross-coupled $YBa_2Cu_3O_7$ filters with spurious suppression using tap connection technique," IEEE Trans. Appl. Supercond., 17, 894-897, (2007).

[145] F. Oisjoen, J. Schneiderman , G. Figueras, M. Chukharkin, A. Kalabukhov, A. Hedstrom, M. Elam and D. Winkler, "High-T_c superconducting quantom interface device recording spontaneous brain activity," Appl. Phys. Lett., 100,13260, (2012).

[146] R. J Cava. Oxide superconductors. Journal of American Ceramic Society 83, 5-28, (2000).

[147] V. A. Vasko. Critical current suppression in a superconductor by injection of spin-polarized carriers. Phys. Rev. Lett. 78, 1134, (1994).

[148] C. Wu, M. Hsu, K. L. Chen, J. C. Chen, J. T. Jeng, T. S. Lai, H. E. Horng and H. C. Yang, "A highly sensetive $YBa_2Cu_3O_7$ seril SQUID magnetometer with flux focuser," Supercond. Sci. Technol., 19, S264, (2004).

[149] A. Mogro-Campero, "A review of high temperature superconducting films on Silicon," Supercond. Sci. Technol., 3, 953-2048, (1990).

[150] P. Chaudhari, R. Koch, R. Laibowitz, T. McGuire and R. Gambino, "Critical-current measurments in epitaxial films of $YBa_2Cu_3O_7$," Phys. Rev. Lett., 58, 2684, (1987).

[151] A. Sarkar, S. Ray, A. Dhar, D. Bhattacharya and K. Chopra, "In-situ superconducting $YBa_2Cu_3O_7$ films on buffered Silicon substrate for device applications," J. Supercond., 9, 217, (1996).

[152] Q. Jia and W. Anderson, "Comperative studies of ohmic contacts to superconductor $YBa_2Cu_3O_7$ thin films with different contact materials," Appl. Phys. Lett., 219, 518, (1991).

[153] S. Muira, T. Yoshitake, Y. Miyasaka, N. Shohata and T. Satoh, "Epitaxial $YBa_2Cu_3O_7$ films on Si with intermediate layer by RF magnetron sputtering," Phys. Lett., 53, 1967-1969, (1998).

[154] A. Chiodoni, V. Ballarini, D. Botta, C. Camerlingo, F. Fabbri, F. Ferrari, R. Gerbaldo, G. Ghigo, L. Gozzelino, F. Laviano, B. Minetti, C. Pirri, G. Tallarida, E. Tresso and E. Mezzetti, "Caharacterization of Silicon- $YBa_2Cu_3O_7$ buffered multilayers grown by sputtering," Appl. Surf. Sci., 238, 485-489, (2004).

[155] U. Balachandran, M. Li, R. Koritaha, B. Fisher and B. Ma, "Development of $YBa_2Cu_3O_7$-coated conductors for electric power applications," Physica C., 372, 869-872, (2002).

[156] L. Luo, R. Muenchausen, C. Maggiore, J. Jimenez and L. Schowalter, "Growth of $YBa_2Cu_3O_7$ thin films on Silicon with $CoSi_2$ buffer layer," Appl. Phys. Lett., 58, 419-421, (1991).

[157] P. Wang, J. Li, W. Peng, Y. F. Chen and D. N. Zheng, "Investigation of strain relaxation and ageing effect of $YBa_2Cu_3O_7$ thin films grown on Silicon-on-insulator substrate with yttria-stabilizied zirconia buffered layers," Supercond. Sci. Technol., 19, 51-56, (2006).

[158] T. Venkatesan, E. Chase, X. Wu, A. Inam, C. Chang and F. Shokoohi, "Superconducting $YBa_2Cu_3O_7$ on Silicon," Appl. Phys. Lett., 53, 243, (1998).

[159] S. Witanachi, S. Patel, H. Kwok and D. Shaw, "As-deposited superconducting $YBa_2Cu_3O_7$ films on Silicon at 400C," Appl Phys. Lett., 54, 578-580, (1989).

[160] T. Robin, A. Mesarwi, N. Wu, W. Fan, L. Espoir, R. Sega and A. Ignatiev, " $YBa_2Cu_3O_7$ growth on thin Y-enhanced SiO_2 buffer layer on Silicon," Appl. Phys. Lett., 59, 2323-2325, (1991).

[161] H. Ishiwara, N. Tsuji, H. Mori and H. Noshira, "Preparation of $YBa_2Cu_3O_7$ thin films on Si (001) substrate using $SrTiO_3$ buffer layer," Appl. Phys. Lett., 61, 1459-1461, (1992).

[162] F. Sanchez, M. Varela, X. Queralt, R. Aguiar and J. Morenza, "Prepration of $SrTiO_3$ thin films on Si (001) substrate by laser ablation: application as a buffer layer for $YBa_2Cu_3O_7$ film," Appl. Phys. Lett., 61, 2228-2230, (1992).

[163] J. Qiao and C. Yang, "High-T_c superconductros on buffered Silicon," Mater. Sci. Eng., R14 157-202, (1995).

[164] T. Ami, Y. Ishida, N. Nagasawa, A. Machida and M. Suzuki, "Room temperature epitaxia growth $CeCo_2$ thin film on Silicon substrate by electron beam evaporation," Appl. Phys. Lett., 78, 1361-1363, (2001).

[165] G. Poullain, B. Mercey, H. Murray and B. Raveau, "High-T_c superconductive film on Silicon substrate," Mod. Phys. Lett B., 2, 523-526, (1998).

[166] E. Bouteloup, M. Hervieu, B. Mercey, G. Poullain, B. Raveau and T. Rouillon, "Characterization of superconducting thin film growth on Silicon substrate," J. Cryst. Growth. , 91, 418-422, (1988).

[167] T. Venkatesan, X. D. Wu, B. Dutta, A. Inam, M. S. Hedge, D. M. Hwang, C. C. Chang and B. Wilkins, "High temperature superconductivity in ultra thin films of $YBa_2Cu_3O_7$," Appl. Phys. Lett., 54, 58, (1989).

[168] Y. Wei, X. Hu, Y. Liang, D. C. Jordan, B. Craigo, R. Drooped, Z. Yu, A. Demkov, J. L. Edwards and W. J. Ooms, "Mechanisim of cleaning Si (001) surface using Sr or SrO for the growth of crystalline $SrTiO_3$," J. Vac. Sci. Tech B. , 20 1402, (2002).

[169] J. R. Hardy and J. W. Flocken, Possible Origins of High-T_c Superconductivity, Phys. Rev. Lett. 60, 2191, (1988).

[170] Y. Wei, X. Hu, Y. Liang, D. C. Jordan, B. Craigo, R. Drooped, Z. Yu, A. Demkov, J. L. Edwards and W. J. Ooms, "Mechanisim of cleaning Si (001) surface using Sr or SrO for the growth of crystalline $SrTiO_3$," J. Vac. Sci. Tech B. , 20 (2002) 1402.

[171] Douglas B. Chrisey and Graham K. Hubler, Pulsed laser deposition of thin films, (1994).

[172] J. H. Ngai, R. Beck, G. Leibovitch, G. Deutscher and J. Y. Wei, "Local tunneling probe of (110) $YBa_2Cu_3O_7$ thin films in a magnetic field," Phys. Rev B., 82, 054505, (2010).

[173] X. Shen, K. Ahmadi-Majlan, J. H. Ngai, D. Wu and D. Su, "Interfacial structure in epitaxial perovskite oxides on (001) Ge crystal," Appl. Phys. Lett., vol. 106, p. 032903, (2015).

[174] Kevin Bautista, Four-Point Probe Operation, Thin Film Deposition, University Texas at Dallas, (2004).

[175] M. Imada, A. Fujimori and Y. Tokura, Metal-insulator transitions, Rev. Mod. Phys. 70, 1039 (1998).

[176] D. P. Kumah, A. S. Disa, J. H. Ngai, H. -H. Chen, A. Malashevich, J. W. Reiner, S. Ismail-Beigi, F. J. Walker and C. H. Ahn, Tuning the Structure of Nickelates to Achieve Two-Dimensional Electron Conduction, Adv. Mater. 26, 1935 (2014).

[177] P. D. C. King, H. I. Wei, Y. F. Nie, M. Uchida, C. Adamo, S. Zhu, X. He, I. Bozovic, D. G. Schlom and K. M. Shen, Atomic-scale control of competing electronic phases in ultrathin $LaNiO_3$, Nat. Nanotech. 9, 443 (2014).

[178] A. Ohtomo and H. Y. Hwang, A high-mobility electron gas at the $LaAlO_3/SrTiO_3$ heterointerface, Nature 427, 423 (2004).

[179] J. Mannhart and D. G. Schlom, Oxide Interfaces—An Opportunity for Electronics, Science 327, 1607 (2010).

[180] P. Moetakef, C. A. Jackson, J. Hwang, L. Balents, S. J. Allen and S. Stemmer, Toward an artificial Mott insulator: Correlations in confined high-density electron liquids in $SrTiO_3$, Phys. Rev. B 86, 201102(R) (2012).

[181] P. Xu, Y. Ayino, C. Cheng, V. S. Pribiag, R. P. Comes, P. V. Sushko, S. A. Chambers and B. Jalan, Predictive Control over Charge Density in the Two-Dimensional Electron Gas at the Polar-Nonpolar $NdTiO_3/SrTiO_3$ Interface, Phys. Rev. Lett. 117, 106803 (2016).

[182] A. D. Caviglia, S. Gariglio, N. Reyren, D. Jaccard, T. Schneider, M. Gabay, S. Thiel, G. Hammerl, J. Mannhart and J. M. Triscone, Electric field control of the $LaAlO_3/SrTiO_3$interface ground state, Nature 456, 624 (2008).

[183] J. Biscaras, N. Bergeal, A. Kushwaha, T. Wolf, A. Rastogi, R. C. Budhani and J. Lesueur, Two-dimensional superconductivity at a Mott insulator/band insulator interface $LaTiO_3/SrTiO_3$, Nat. Comm. 1, 89 (2010).

[184] L. Li, C. Richter, J. Mannhart and R. C. Ashoori, Coexistence of magnetic order and two-dimensional superconductivity at $LaAlO_3/SrTiO_3$ interfaces, Nat. Phys. 7, 762 (2011).

[185] J. H. Ngai, F. J. Walker and C. H. Ahn, Correlated Oxide Physics and Electronics, Annu. Rev. Mater. Res. 44, 1 (2014).

[186] J. B. Torrance, P. Lacorre, A. I. Nazzal, E. J. Ansaldo, and Ch. Niedermayer, Systematic study of insulator-metal transitions in perovskites $RNiO_3$ due to closing of charge-transfer gap, Phys. Rev. B 45, 8209(R), (1992).

[187] B. Brière, J. Caillaux, Y. Le Gal, D. Lorcy, S. Lupi, A. Perucchi, M. Zaghrioui, J. C. Soret, R. Sopracase, and V. Ta Phuoc, Interplay between bandwidth-controlled and filling-controlled pressure-induced Mott insulator to metal transition, Phys. Rev. B 97, 035101, (2018).

[188] C. C. Hays, J. -S. Zhou, J. T. Markert and J. B. Goodenough, Electronic transition in $La_{1-x}Sr_xTiO_3$, Phys. Rev. B 60, 10367 (1999).

[189] Y. Tokura, Y. Taguchi, Y. Okada, Y. Fujishima, T. Arima, K. Kumagai and Y. Iye, Filling dependence of electronic properties on the verge of metal–Mott-insulator transition in $Sr_{1-x}La_xTiO_3$, Phys. Rev. Lett. 70, 2126 (1993).

[190] P. Moetakef, T. A. Cain, D. G. Ouellette, J. Y. Zhang, D. O. Klenov, A. Janotti, C. G. Van de Walle, S. Rajan, S. J. Allen and S. Stemmer, Electrostatic carrier doping of $GdTiO_3/SrTiO_3$ interfaces, Appl. Phys. Lett. 99, 232116 (2011).

[191] E. N. Jin, L. Kornblum, . D. P. Kumah, K. Zou, C. C. Broadbridge, J. H. Ngai, C. H. Ahn and F. J. Walker, A high density two-dimensional electron gas in an oxide heterostructure on Si (001), APL Mater. 2, 116109 (2014).

[192] L. Kornblum, E. N. Jin, D. P. Kumah, A. T. Ernst, C. C. Broadbridge, C. H. Ahn and F. J. Walker, Oxide 2D electron gases as a route for high carrier densities on (001) Si, Artificial charge-modulationin atomic-scale perovskite titanate superlattices, Appl. Phys. Lett. 106, 201602 (2015).

[193] A. Ohtomo, D. A. Muller, J. L. Grazul and H. Y. Hwang, Electronic reconstruction at an interface between a Mott insulator and a band insulator, Nature 419, 378 (2002).

[194] S. Okamoto and A. J. Millis, Electronic reconstruction at an interface between a Mott insulator and a band insulator. Nature 428, 630 (2004).

[195] J. S. Kim, S. S. A. Seo, M. F. Chisholm, R. K. Kremer, H. -U. Habermeier, B. Keimer and H. N. Lee, Nonlinear Hall effect and multichannel conduction in $LaTiO_3/SrTiO_3$superlattices, Phys. Rev. B 82, 201407(R) (2010).

[196] Tyler A. Cain, Pouya Moetakef, Clayton A. Jackson, and Susanne Stemmer, Modulation doping to control the high-density electron gas at a polar/non-polar oxide interface, Appl. Phys. Lett. 101, 111604 (2012).

[197] J. Mannhart1 and D. G. Schlom, Oxide Interface, Opportunity for Electronics, Science, 327, 26, (2010).

[198] K. Zou, Sohrab Ismail-Beigi, Kim Kisslinger, Xuan Shen, Dong Su, F. J. Walker and C. H. Ahn, $LaTiO_3$/KTaO3 interfaces: A new two-dimensional electron gas system, APL MATERIALS 3, 036104 (2015).

[199] H. Ishida1 and A. Liebsch, Origin of metallicity of $LaTiO_3/SrTiO_3$ heterostructures, Phys. Rev. B. 77, 115350, (2008).

[200] C. CEN, S. THIEL, G. HAMMERL, C. W. SCHNEIDER, K. E. ANDERSEN, C. S. HELLBERG, J. MANNHART AND J. LEVY, Nanoscale control of an interfacial metal–insulator transition at room temperature, nature materials, 7, (2008).

[201] National Institute of Standard and Technology, U.S Department of Commerce, Energy and Physics Division.

[202] M. Takizawa, H. Wadati, K. Tanaka, M. Hashimoto, T. Yoshida, A. Fujimori, A. Chikamatsu, H. Kumigashira, M. Oshima, K. Shibuya, T. Mihara, T. Ohnishi, M. Lippmaa, M. Kawasaki, H. Koinuma, S. Okamoto and A. J. Millis, Photoemission from Buried Interfaces in $SrTiO_3$/$LaTiO_3$Superlattices, Phys. Rev. Lett. 97, 057601 (2006).

[203] S. S. A. Seo, W. S. Choi, H. N. Lee, L. Yu, K. W. Kim, C. Bernhard and T. W. Noh, Optical Study of the Free-Carrier Response of $LaTiO_3$/$SrTiO_3$Superlattices, Phys. Rev. Lett. 99, 266801 (2007).

[204] P. Nozieres and D. Pines, Surface depletion in doped $SrTiO_3$ thin films, Appl. Phys. Lett. 84, 1716 (2004).

[205] 28P. B. Chakraborty, K. Byczuk, and D. Vollhardt, Interacting lattice electrons with disorder in two dimensions: Numerical evidence for a metal-insulator transition with a universal critical conductivity, Phys. Rev. B 84,035121 (2011).

[206] A L Efros and B I Shklovskii, Coulomb gap and low temperature conductivity of disordered systems, Journal of Physics C: Solid State Physics, 8, (1975).

[207] J.W. Matthews, A.E. Blakeslee, Defects in epitaxial multilayers: Misfit dislocations, Journal of Crystal Growth, 27, 118-125, (1974).

[208] Alireza Moridi, Haihui. Ruan, L. C. Zhang, Mei. Liu, Residual stresses in thin film systems: Effects of lattice mismatch, thermal mismatch and interface dislocations, International Journal of Solids and Structures, 50, 3562-3569, (2013).

[209] E.Popova, .Warot-Fonrose, F.Bonell, S.Andrieu, Y.Dumont, B.Berini, A.Fouchet, N.Keller, , Mechanism of the lattice relaxation in thin epitaxial films of iron oxides, Surface Science, 605, 1043-1047, (2011).

[210] P.F. Fewster, Characterization of quantum wells by X-ray diffraction, Semicond. Sci. Technol. 8, 1915 (1993).

[211] B.K. Tanner, in: Analysis of Microelectronic Materials and Devices, Eds. M. Grasserbauer, H.W. Werner, Wiley, Vienna, 609, (1991).

[212] E. Koppensteiner, G. Bauer, H. Kibbel, E. Kasper, Investigation of strain-symmetrized and pseudomorphic Si_mGe_nsuperlattices by x-ray reciprocal space mapping, J. Appl. Phys. 76, 3489 (1994).

[213] C.R. Wie, High resolution X-ray diffraction of semiconductor structures, Mater. Sci. Eng. R 13, 1 (1994).

[214] V. Holy, J. Kubena, K. Ploog, X-Ray Analysis of Structural Defects in a Semiconductor Superlattice, Phys. Status Solidi B 162, 347 (1990).

[215] V. Holy, J. Kubena, E. Abramof, A. Pesek, E. Koppensteiner, High resolution x-ray reciprocal space mapping, J. Phys. D, Appl. Phys. 26, A146 (1993).

[216] Brian Jones, Martin Zimmermann, High Resolution X-ray Diffractometry 2 – Reciprocal Space Mapping, (2012).

[217] A. K. Tagantsev, Piezoelectricity and flexoelectricity in crystalline dielectrics, Phys. Rev. B 36, 6177 (1987).

[218] W. Kohn and L. J. Sham, "Self-Consistent Equations Including Exchange and Correlation Effects," Phys. Rev., vol. 140, p. A1133, 1965.

[219] P. E. Blochl, "Projector augmented-wave method," Phys. Rev. B, vol. 50, pp. 17953-17979, 1994.

[220] G. Kresse and D. Joubert, "From ultrasoft pseudopotentials to the projector augmented-wave method," Phys. Rev. B, vol. 59, pp. 1758-1775, 1999.

[221] D. P. Kumah, J. W. Reiner, Y. Segal, A. M. Kolpak, Z. Zhang, D. Su, Y. Zhu, M. S. Sawicki, C. C. Broadbridge, C. H. Ahn and F. J. Walker, "The atomic structure and polarization of strained SrTiO3/Si," Appl. Phys. Lett., vol. 97, p. 251902, 2010.

[222] D. R. Hamann, D. A. Muller and H. Y. Hwang, "Lattice-polarization effects on electron-gas charge densities in ionic superlattices," Phys. Rev. B, vol. 73, no. 19, p. 195403, 2006.

[223] S. Okamoto, A. Millis and N. Spaldin, "Lattice relaxation in oxide heterostructures: $LaTiO_3/SrTiO_3$ superlattices," Phys. Rev. Let., 97, 056802, (2006).

[224] J. H. You and J. H. Lee, "Critical thickness for the two-dimensional electron gas in $LaTiO_3/SrTiO_3$ superlattices," Phys. Rev. B, 88, 155111, (2013).

[225] D. Lee, A. Yoon, S. Y. Jang, J.-G. Yoon, J.-S. Chung, M. Kim, J. F. Scott and T. W. Noh, "Giant Flexoelectric Effect in Ferroelectric Epitaxial Thin Films," Phys. Rev. Lett., 107, 057602, (2011).

[226] L. J. van der Pauw, "A Method of Measuring the Resistivity and Hall Coefficient on Lamellae of Arbitrary Shape," Philips Tech. Rev. 20, 220-224 (1958).

[227] N. F. Mott, Coulomb gap and low-temperature conductivity of disordered systems J. Phys. C: Solid State Phys. 8 L239, (1975).

Biographical Information

Kamyar Ahmadimajlan completed a Bachelor of Science in Metallurgical Engineering at Yazd University in 2007. He focused on the dual alloys within Metallurgical Engineering, and he had over three years of experience as an engineer in the field of high temperature alloying, working in Azmoon foundry . In 2009, Kamyar joined the University Technology of Malaysia as a master student in mechanical materials engineering and began research with Dr. Sakhawat on Ni deposition . In 2012, he joined University of Texas at Arlington as a PhD student in Material Science and Engineering working with Dr. Joseph H. Ngai in Physics department. During his PhD he was mainly focused on growing epitaxial films and integrating transition metal oxides on conventional semiconductors for future device applications. He presented at several conferences such APS 2014,2015,2016,2017, MRS 2017, ACES 2015,2016, TSM 2015. In addition, his research was awarded as the best student talk at several conferances such as ACES2015, MSE 2016 and 26-EMC Conference 2017. During his graduate education, Kamyar completed two internships with FEI company and Thermofisher, in Richardson, Texas. He worked in the Research & Development of Thermofisher, for developing new nano prober system. In August of 2018, he will begin a full time job as an application engineer in Thermofisher EFA department, working on various nano probing systems and failure analysis tools.

List of Publications and Presentations

2. Kamyar Ahmadi-Majlan, Mohammadreza Jahangir-Moghadam, Xuan Shen, Timothy, Droubay, Mark Bowden, Matthew Chrysler, Dong Su, Scott A Chambers, Joseph H Ngai, Band-Gap Engineering at a Semiconductor–Crystalline Oxide Interface, Advanced Materials Interfaces, 2, 140049, (2015).
3. J. H. Ngai, K Ahmadi-Majlan, J Moghadam, M Chrysler, D Kumah, FJ Walker, CH Ahn, T Droubay, Y Du, SA Chambers, M Bowden, X Shen, D Su, Electrically coupling complex oxides to semiconductors: A route to novel material functionalities, Journal of Materials Research, 32, 249-259, (2017).
4. Xuan Shen, K Ahmadi-Majlan, Joseph H Ngai, Di Wu, Dong Su, Interfacial structure in epitaxial perovskite oxides on (001) Ge crystal, 106, 032903, (2015).
5. ZH Lim, K Ahmadi-Majlan, ED Grimley, Yingge Du, M Bowden, Reza Moghadam, James M LeBeau, Scott A Chambers, J. H. Ngai, Structural and electrical properties of single crystalline $SrZrO_3$ epitaxially grown on Ge (001), 122, 084102, (2017).
6. Reza M Moghadam, Zhiyong Xiao, Kamyar Ahmadi-Majlan, Everett D Grimley, Mark Bowden, Phuong-Vu Ong, Scott A Chambers, James M Lebeau, Xia Hong, Peter V Sushko, Joseph H Ngai, An Ultrathin Single Crystalline Relaxor Ferroelectric Integrated on a High Mobility Semiconductor, 17, 6248-6257, (2017).

7. Tongjie Chen, Kamyar Ahmadi-Majlan, Zheng Hui Lim, Zhan Zhang, Joseph H Ngai, Alexander F Kemper, Divine P Kumah, Interfacial Structure of $SrZr_xTi_{1-x}O_3$ films on Ge, arXiv preprint arXiv:1806.11140, (2018).
8. Joseph Ho Yeen Ngai, Reza M Moghadam, Kamyar Ahmadi-Majlan, Ferroelectric composition on semiconductor and method for producing same, 15730706, (2018)
9. K Ahmadi-Majlan, H Zhang, X Shen, MJ Moghadam, M Chrysler, P Conlin, R Hensley, D Su, JYT Wei, J. H. Ngai, Superconducting epitaxial YBCO on $SrTiO_3$-buffered Si(001), Journal Bulletin of Materials Science, 41, 23, (2018).
10. Joseph H. Ngai Kamyar Ahmadi-Majlan, Tongjie Chen, Zheng Hui Lim, Patrick Conlin, Ricky Hensley, Matthew Chrysler, Dong Su, Hanghui Chen, Divine P. Kumah, Tuning metal-insulator behavior in $LaTiO_3/SrTiO_3$ heterostructures integrated directly on Si(100) through control of atomic layer thickness, Applied Physics Letters, 112, 193104, (2018).
11. Kamyar Ahmadi Majlan, Tongjie Chen, Ricky Hensley, Patrick Conlin, Zheng Hui Lim, Reza Moghadam, Dong Su, Divine P Kumah, Joseph H Ngai, Thickness dependent metal-insulator transition of a correlated oxide heterostructure integrated directly on Si, Bulletin of the American Physical Society, 62, (2017).
12. Reza Moghadam, Z-Y Xiao, K Ahmadi-Majlan, E Grimley, PV Ong, JM Lebeau, SA Chambers, X Hong, P Sushko, JH Ngai, Scalable ferroelectric MOS capacitors comprised of single crystalline SrZrxTi1-xO3 on Ge., APS Meeting , (2017).
13. Joseph Ngai, K Ahmadi-Majlan, J Moghadam, M Chrysler, DP Kumah, CH Ahn, FJ Walker, T Droubay, M Bowden, SA Chambers, X Shen, D Su, Electrically Coupling Multifunctional Oxides to Semiconductors: A Route to Novel Material Functionalities, MRS ADVANCES, (2016).

14. Kamyar Ahmadi Majlan, Mohammadreza Jahangir Moghadam, Xuan Shen, Ricky Hensley, Patrick Conlin, Zheng Hui Lim, Dong Su, Joseph H Ngai, Tuning electrical transport in rare-earth delta-doped SrTiO3 epitaxially grown on Si (001), APS Meeting , (2016).
15. Kamyar Ahmadi-Majlan, Mohammadreza Jahangir-Moghadam, Xuan Shen, Timothy Droubay, Mark Bowden, Matthew Chrysler, Dong Su, Scott A Chambers, Joseph H Ngai, Band-gap engineering at a semiconductor-crystalline oxide interface, APS March Meeting, (2015).
16. Mohammadreza Jahangir Moghadam, Kamyar Ahmadi Majlan, Hao Zhang, Xuan Shen, Matthew Chrysler, Patrick Conlin, Ricky Hensley, Dong Su, John Wei, Joseph Ngai, Superconducting single crystalline YBa2Cu3O7-delta on SrTiO3 buffered Si (100), APS March Meeting, (2015).